Structure, Mobility, and Composition of Transition Metal Catalyst Surfaces: High-Pressure Scanning Tunneling Microscopy and Ambient-Pressure X-ray Photoelectron Spectroscopy Studies

by

Zhongwei Zhu

A dissertation submitted in partial satisfaction of the
requirements for the degree of
Doctor of Philosophy
in
Chemistry
in the
Graduate Division
of the
University of California, Berkeley

Committee in Charge:

Professor Gabor A. Somorjai, Chair
Professor Peidong Yang
Professor Michael Crommie

Fall 2013

Abstract

Structure, Mobility, and Composition of Transition Metal Catalyst Surfaces: High-Pressure Scanning Tunneling Microscopy and Ambient-Pressure X-ray Photoelectron Spectroscopy Studies

by

Zhongwei Zhu

Doctor of Philosophy in Chemistry

University of California, Berkeley

Professor Gabor A. Somorjai, Chair

Surface structure, mobility, and composition of transition metal catalysts were studied by high-pressure scanning tunneling microscopy (HP-STM) and ambient-pressure X-ray photoelectron spectroscopy (AP-XPS) at high gas pressures. HP-STM makes it possible to determine the atomic or molecular rearrangement at catalyst surfaces, particularly at the low-coordinated active surface sites. AP-XPS monitors changes in elemental composition and chemical states of catalysts in response to variations in gas environments. Stepped Pt and Cu single crystals, the hexagonally reconstructed Pt(100) single crystal, and Pt-based bimetallic nanoparticles with controlled size, shape and composition, were employed as the model catalysts for experiments in this thesis.

Surface reconstruction at low-coordinated step sites at high gas pressures was first explored on a stepped Pt(557) single crystal surface under O_2. At 298 K, 1 Torr of O_2 is able to create nanometer-sized clusters that are identified as surface Pt oxide by AP-XPS, which covers the entire Pt(557) surface. On the flat Pt(111) surface under 1 Torr of O_2, Pt oxide clusters can form but are mostly accumulated within 2 nm from the steps. The hexagonal oxygen chemisorption pattern is observed on the terraces. At lower pressures such as 10^{-7} Torr, O_2 only adsorbs at the step edges on Pt(557). The majority of the Pt oxide clusters disappear on both Pt(557) and Pt(111) surfaces after O_2 is evacuated to the 10^{-8} Torr range. Quantitative XPS analysis with depth profiles indicates that the Pt oxide formed on Pt(557) is less than 0.6 nm thick and that the Pt oxide concentration at surface together with oxygen coverage varies reversibly with the O_2 pressure.

The disappearance of Pt oxide clusters upon O_2 evacuation is ascribed to reactions of Pt oxide towards H_2 and CO in the vacuum background gases. The structure and surface

chemistry of the Pt(557) surface was therefore studied under H_2-O_2 and CO-O_2 mixtures. After exposing Pt(557) to approximately 1 Torr of O_2 to induce the formation of Pt oxide clusters, H_2 was slowly added into the system. Both HP-STM and AP-XPS results show that the Pt oxide coverage decreases with the H_2 partial pressure and that all the Pt oxide disappears at H_2 partial pressures above 43 mTorr. Pt steps are restored with the removal of Pt oxide clusters. Water is produced in the gas-phase, which co-adsorbs with hydroxyl species on Pt(557). Detailed analysis shows that the consumption of surface Pt oxide is exclusively responsible for the decrease of oxygen coverage on Pt(557). In the coexistence of 1 Torr of CO and 1 Torr of O_2, Pt oxide clusters are not observed like under the H_2-O_2 mixture. Instead, triangular Pt clusters and double-sized terraces induced by CO are observed.

Influences of step configuration on the surface restructuring processes were studied on Pt(557) and Pt(332) that differ only in the step orientation. 500 mTorr of CO creates Pt clusters shaped as triangles and parallelograms on Pt(557) and Pt(332), respectively. When 500 mTorr of C_2H_4 was introduced afterwards, Pt clusters are removed on Pt(332) but preserved on Pt(557). The three-fold hollow sites at the (111) steps enable the Pt(332) surface to accommodate ethylidyne even covered by CO. As a result, kink Pt atoms at the cluster edges are driven to diffuse to form straight steps, so as to admit more ethylidyne at steps. In contrast, Pt(557) has (100) steps on which ethylidyne does not adsorb, therefore keeping the island structure after the introduction of C_2H_4. When 500 mTorr of C_2H_4 was added first into the high-pressure cell, a periodic pattern is resolved at step edges on Pt(332). In contrast, some bright species separated by more than 1 nm are observed on Pt(557). Further introducing 500 mTorr of CO does not facilitate the formation of Pt clusters.

The structure and mobility under C_2H_4, H_2, and CO were also studied on the Pt(100) surface, whose topmost layer is rearranged into a hexagonal overlayer in vacuum. Under 1 Torr of C_2H_4, the hexagonal reconstruction is preserved on Pt(100), which is covered by highly mobile adsorbates. Pt atoms on the hexagonal layer can also move as a result of the weakened interaction between the surface layer and the bulk. The mobility is enhanced under 1 Torr of 1:1 C_2H_4-H_2 mixture because the Pt(100)-hex surface is active in ethylene hydrogenation. The surface mobility along with the catalytic reaction is quenched after introducing 3 mTorr of CO. Meanwhile, the hexagonal reconstruction is lifted by the adsorption of CO. At 5×10^{-6} Torr of C_2H_4, CO from background gases can also adsorb on Pt(100), creating Pt islands that do not revert to the hexagonal surface when the C_2H_4 pressure was further increased to 1 Torr.

In order to understand the effect of substrates on surface reconstruction, the structure of the stepped Cu(557) surface was monitored in equilibrium with high pressures of gases. Cu generally binds to the reducing gases such as CO, H_2, and C_2H_4 weaker than Pt, leading to a lower coverage on Cu than on Pt at the same gas pressure. Accordingly, 12 Torr of

CO is required to induce clusters on Cu(557), because higher CO pressures are needed to keep a sufficient amount of CO that can stabilize clusters. At 1 Torr, large terraces with an average width of 23 nm are observed on Cu(557), because of the low diffusion barrier for Cu atoms both on terraces and along the steps. 500 mTorr of H_2 results in step coalescence on Cu(557), giving rise to 6 nm wide terraces. C_2H_4 adsorption at 500 mTorr results in 5 nm large clusters. CO does not change the Cu(557) surface structure while adding into C_2H_4, but causes the appearance of large terraces while co-adsorbing with H_2. Under oxidizing gases, for example 1 Torr of O_2, the Cu(557) surface is significantly oxidized, forming thick layers of Cu oxide.

Pt-based bimetallic nanoparticle catalysts were also investigated with AP-XPS under reaction conditions to study their surface chemistry. PtFe nanoparticles do not undergo any surface segregation at 298 K when the gas environment changes, but surface Fe atoms are partially reduced under the C_2H_4-H_2 mixture and partially oxidized under O_2. Neither does the surface composition of Pt_9Co-Co core-shell nanoparticles change while heating under H_2 even to 673 K nor do oxidation states. In Pt−Ni systems, at 393 K, Ni is oxidized under O_2 and migrates to the surface because Ni is more susceptible to oxidation than Pt. In contrast, when the surface is reduced by H_2, Pt segregates to the surface since the surface free energy of Pt is lower. Such segregation does not occur at 353 K owing to the low atomic mobility in lattice.

Dedicated to my grandparents, my parents, and my aunt.

Table of Contents

Acknowledgements

Time has flew so fast that my Ph.D. studies in Berkeley is coming to the end, but it seems yesterday when I knocked on the door of Prof. Somorjai's office as a first-year graduate student. With the help and support from a lot of people both in science and in personal life, the past four and a half years was a fantastic journey for me.

First of all, I am sincerely grateful to my supervisor, Prof. Gabor A. Somorjai, who has provided me with the opportunity to work in such a great group. It was under his guidance and encouragement that I learned how to become an independent researcher, for which Prof. Somorjai himself is a world-class example. I truly appreciate his kindness, patience, and encouragement when I was initially struggling on learning the complex instrument. Apart from research, he also pays special attention to the future of his students and post-doctoral fellows, and he was extremely helpful in getting me a wonderful job to start with after graduation. Without him, an instructor in science and a mentor in life, I could not achieve what I have accomplished.

I would love to acknowledge Prof. Miquel Salmeron for his invaluable help on my research during my Ph.D. studies. His passion in science and open mind to new technology continue inspiring me to pursue further in my projects. He has carefully instructed me to pay attention to every detail in the data and to accurately present the results. I am so fortunate to have another advisor who is not only outstanding in science but also has great personalities, which I believe will benefit my future career and life.

Berkeley accumulates a lot of bright minds in the world, among which the brightest ones are certainly in the Somorjai group and the Salmeron group. I would like to thank Prof. Feng Tao and Dr. Derek Butcher in teaching me STM hand by hand. Xiaofeng Feng is so warm-hearted to help me twice on repairing the instrument and lots of discussions. I also want to acknowledge Inger Coble, a wonderful secretary, for all her essential assistance on everything small but important throughout my studies. I would like to thank Prof. Wenyu Huang, Prof. Chia-Kuang Tsung, Dr. Yimin Li, and Dr. Fan Zheng for their great help during my first two years. I want to express my gratitude to Christopher Thompson, my fellow in the same year, for all the support over the years. I also want to thank other past and present Somorjai group members, including Dr. Qiao Zhang, Dr. Hailiang Wang, Dr. Vladimir Pushkarev, Dr. Selim Alayoglu, Dr. Simon Beaumont, Dr. Gérôme Melaet, Dr. Kwangjin An, Dr. Antoine Hervier, Dr. Robert Baker, Dr. Elad Gross, Dr. Andras Sapi, Dr. Yihai Wang, Dr. Yuri Borodko, Cédric Barroo, Griffin Kennedy, Feifei Shi, Nate Musselwhite, Avery Lindeman, Walter Ralston, and Lindsay Carl, and other Salmeron group members, including Dr. Yu Shi, Dr. Byoung Choi, Dr. Sara Barja, Dr. Leonid Lichtenstein, Dr. Sophie Carenco, Chenghao Wu, Wei Bao, Yingjie Zhang, and Alexander Buyanin, for keeping a great working environment.

I would love to give my special thanks to Dr. Zhi Liu, the smart and kind beamline scientist. He has supported me on all the AP-XPS experiments at ALS and instructed me on data analysis. I also would like to thank his students and post-doctoral fellows at the beamline, Dr. Rui Chang, Dr. Stephanus Axnanda, and Baohua Mao, for the help during my experiments at the beamline.

No matter how many words I write here will not be enough to express my gratitude to my parents. They first suggested that I should pursue Ph.D. studies abroad and they spurred me to do so from every aspect. Their vision and full love has guided me to keep moving forward without any concern. I am so glad to have them attend my graduation ceremony, to share that memorable moment with them. I am also extremely grateful to my girlfriend, Jinnan Li. It is all her love that gives me a happy life besides research.

Life would be boring if without any friends here in Berkeley. I would love to specially acknowledge Chenghao Wu, my fantastic roommate for over 3 years, for all his warm help in daily life. I am always grateful to Dr. Ziyang Huo, Dr. Miao Zhang, Dr. Chen Chen, Caiyun Nan, and Chong Liu for their help over the years. I would like to thank my other friends I met here in Berkeley, Dr. Yichen Tan, Dr. Jie Zhang, Zhaoyi Kang, Pengcheng Zhang, Ying Qiao, Lei Cheng, Hongwei Li, Fangfang Ren, Shaomin Xiong, Wenjun Shao, and Xue Wang, for the great time we have spent together.

Throughout the years I have also received constant help and encouragement from many friends. I want to thank Yaodong Liu, Yi Zeng, Tian Ouyang, Xia Wang, Liteng Liu, Lizhi Liu, Juerui Zeng, Lizhi Xu, Xia Shu, Xinxi Liu, Yuhang Jin, Yifei Yan, Jia Liu, Jin Xie, and He Huang for all their support.

Lastly, I want to thank Department of Chemistry, University of California, Berkeley, and Materials Sciences Division, Lawrence Berkeley National Laboratory for financial support. This thesis was supported by the Director, Office of Science, Office of Basic Energy Sciences, Materials Sciences and Engineering Division, of the U.S. Department of Energy under Contract No. DE-AC02-05CH11231.

Chapter 1

Introduction

Abstract

The importance of *in situ* investigation of catalyst surface structure, mobility, and composition is presented in this chapter. Deep understanding of surface reconstruction and adsorbate mobility under high pressures of gases is essential in heterogeneous catalysis. Among all the *in situ* techniques, high-pressure scanning tunneling microscopy advances in providing local structural information at the molecular level. Ambient-pressure X-ray photoelectron spectroscopy can identify the surface composition and chemical states. Model catalysts used in the experiments of the thesis, well-controlled stepped metal single crystals and bimetallic nanoparticles, are also briefly introduced.

1.1 Importance of *In Situ* Structural Investigation on Catalyst Surfaces

Heterogeneous catalysis has been attracting a great deal of attention for over a century thanks to its essential influence on global economy, since most of industrial products are synthesized through heterogeneously catalyzed reactions.[1,2] Catalysts accelerate reactions by breaking the original rate-limiting step into several extra steps, each with lower activation barriers. The involvement of catalysts is also able to direct multipath reactions preferentially into one pathway, selectively yielding the desired products. By virtue of the effects on enhancing productivity and efficiency, catalysts have been frequently used in numerous fields such as pharmaceutical industry, petrochemistry, polymers, consumer products, and fuel cells.[2] Continuous effort has been devoted to the development of economical and environmental catalysts, in order to address the increasing issues on energy consumption, by means of enhancing catalytic activity and selectivity.

The rates of a great number of catalytic reactions, for example ammonia synthesis,[3] rely on the structure of catalyst surfaces. Such reactions are classified as structure sensitive reactions,[4] in which the catalyst surface structure plays a key role in catalytic performances. The catalyst surface structure governs sites for reactant adsorption, the beginning step in heterogeneous catalysis. The adsorption sites subsequently determine the strength of reactant adsorption and the adsorbate mobility, both important for catalytic turnovers. In addition, the population of an adsorbate layer in turn alters the structure of many catalyst surfaces, which is called adsorbate-induced reconstruction. Reciprocal influences between gas adsorption and the catalyst structure are thus appealing in surface science studies.

Surface restructuring driven by adsorbates is an important molecular factor that affects catalytic performances. Seven molecular factors are identified as crucial in heterogeneous catalysis, including surface composition, oxidation states, reaction intermediates, catalyst size and morphology, adsorbate-induced reconstruction, surface mobility, and charge transfer between metal and oxide supports.[5] Various techniques have been utilized in the past decades for molecular investigation of the principles of heterogeneous catalysis, such as low-energy electron diffraction (LEED), electron energy loss spectroscopy (EELS), molecular beam scattering, Helium atom scattering, X-ray photoelectron spectroscopy (XPS), Auger electron spectroscopy (AES), and scanning tunneling microscopy (STM). A vast database regarding the catalyst surface structure and reaction kinetics has been established in ultrahigh vacuum (UHV), as most conventional surface science techniques require well-controlled crystal surfaces under UHV conditions. Knowledge from UHV experiments has shed light on reaction mechanisms and design of outstanding catalysts with high activity and 100% selectivity.

However, UHV studies have notably reduced the complexity of real catalysis that usually happens at or above atmospheric pressures, which are over 9 orders of magnitude higher than vacuum. Catalyst surfaces are able to admit a dense layer of molecules at high pressures, even though the binding between adsorbates and substrates can be weak. From a

thermodynamic point of view, the Gibbs free energy of gases increases with the pressure via the term kT·log P, leading to the decrease in the value of Gibbs free energy change for all the gas adsorption processes. A dense adsorbate layer is naturally populated at high gas pressures, which potentially causes some restructuring processes that are initially not simultaneous in vacuum to occur. It is thereby open to discussion whether knowledge acquired in UHV can be applicable to real industrial conditions, typically at elevated pressures and temperatures.

A second approach to increase the gas Gibbs free energy other than raising the pressure, according to the term kT·log P that is negative because the pressure is lower than 1 bar in UHV experiments, is to cool the sample to low temperatures during measurements. In several systems, this method indeed results in the same structure as the structure formed at high gas pressures.[6,7] Nevertheless, structures formed by the two manners differ in a lot of systems, since some thermodynamically favored processes are kinetically hindered after cooling because of high activation barriers. Metastable structure is observed at low temperatures in this case. Surface structure of catalysts therefore ought to be investigated at elevated pressures, in order to characterize the real catalyst structure during reactions.

1.2 *In Situ* Characterization Techniques

In attempt to probe the catalyst surface structure during catalytic reactions, surface scientists have developed a variety of *in situ* characterization tools. Most surface science techniques detect photons, electrons, and ions generated at the sample surface or scattered by the sample. Because electromagnetic waves interact with media weakly, techniques on the basis of photon-in and photon-out processes such as X-ray adsorption spectroscopy (XAS)[8] and X-ray emission spectroscopy (XES)[9] are appropriate for *in situ* investigation. Among all the photon-based techniques, sum frequency generation (SFG) vibrational spectroscopy is exclusively surface sensitive,[10] since it requires the breaking of central symmetry that happens only at the interface between catalysts and reactants. As for methods involving electrons, the strong interaction between electrons and gas media leads to low electron mean free paths that limit the application of these techniques at high pressures.[1] Nevertheless, a few electron-based techniques have been improved to accommodate the ability to work at elevated pressures. For instance, environmental transmission electron microscopy (E-TEM) is able to monitor the dynamic evolution of catalysts under gaseous environments or even in liquids.[11] Two sorts of electron-based methods, STM and XPS, were employed for the *in situ* analysis of transition metal catalysts in this thesis.

1.2.1 High-Pressure Scanning Tunneling Microscopy

Since the milestone demonstration in early 1980s,[12,13] STM has revolutionized surface characterization, thanks to the advantage in resolving the surface structure at the atomic or

molecular level on both metal[14,15] and semiconductor[16] surfaces. STM works principally with electrons tunneling from the tip end to a conductive sample surface provided a positive bias on the sample, or *vice versa*. Only electronic states at the sample surface, whether empty at a positive sample bias or filled at a negative sample bias, can thus be detected when the tip scans across the sample surface. In addition, the ability to provide extremely local structure information distinguishes STM from other techniques. Catalytic processes usually occur at special sites such as steps or kinks on metal surfaces, oxygen vacancies on oxides, and interfacial sites between metal and oxide supports. Spectroscopic information from these sites is averaged in the overall data owing to their low surface concentration, even if relevant knowledge could be gained indirectly through fitting. In contrast, STM is able to directly reveal the adsorption, diffusion, and turnover processes at specific surface sites.

Unlike other electron-based techniques that encounter electron scattering by gas molecules at high pressures, STM is capable of working at a wide pressure range from UHV to atmospheric or even higher pressures. Because electrons travel through a gap of a few angstroms to tunnel between the tip and the surface, two orders of magnitude shorter than the electron mean free paths at atmospheric pressures,[1] the majority of tunneling electrons reach the surface without getting scattered by gas molecules. Our group has pioneered in high-pressure STM (HP-STM) by filling gases into the STM chamber initially kept under UHV in the early designs.[17,18] Several HP-STM systems were later established around the world,[19-22] some with the ideas of high-pressure cell[19] or micro-reactor.[20] Lately in 2008, a new HP-STM system was built in our group,[23] in which the STM head is assembled in a high-pressure cell coated by a layer of gold. The gold coating avoids possible reactions between gases and stainless steel used to construct the high-pressure cell, since gold is inert whereas the constituent elements in stainless steel are active at times. Nevertheless, the performance of STM is indeed impacted at high gas pressures, in the sense that adsorption and desorption processes at the tip surface render the STM tip structure unstable during imaging. Additionally, the thermal drift of the tip is severe relative to the drift in UHV experiments.

HP-STM has uncovered the distinct surface structure at high pressures in a lot of systems. One typical example is the (3 × 3)-7NO adsorption pattern on Rh(111) only detectable under 30 mTorr of NO, whereas the (2 × 2)-3NO structure is observed at lower NO pressures.[24] Reconstruction of substrate surfaces caused by gas adsorption is also revealed. For instance, a "missing-row" (1 × 2) structure forms on Cu(110) under 1 bar of H_2, which reverts to the unreconstructed Cu(110) surface with the evacuation of H_2 to 10^{-9} bar.[25] Pt atoms can be embedded into a monolayer FeO film grown on Pt(111) under 20 Torr of CO at 520 K as a result of the partial reduction of the FeO film.[26] HP-STM has unraveled the essence of high surface mobility in catalytic turnovers as well. When the hydrogen-deuterium exchange reaction occurs on Pt(111), no surface order can be

discerned because adsorbates diffuse much faster than the tip scans. However, once CO is introduced to poison the reaction, CO adsorption pattern on Pt(111) is clearly resolvable, owing to the fact that the adsorption of CO has impeded the diffusion of hydrogen and deuterium atoms and thus stopped the reaction.[27]

1.2.2 Ambient-Pressure X-ray Photoelectron Spectroscopy

Electrons and photons are emitted from the surface through various mechanisms in response to external X-ray excitation. Binding energy of core levels in the material can be analyzed by measuring the kinetic energy of photoelectrons, which can be used to identify elemental composition and oxidation states. Given the atomic sensitivity factor of each element at the given incident X-ray energy, surface composition can be quantitatively estimated via peak integration and deconvolution. XPS is surface sensitive because the inelastic mean free paths (IMFPs) of photoelectrons in measurements are commonly at the scale of several atomic layers.

As an electron-based technique, XPS encounters the issue of strong electron scattering by gas molecules at ambient pressures. Photoelectrons need to travel tens of centimeters to reach the analyzer, but the mean free path of electrons under gas pressures of ~1 Torr is in the millimeter range.[1,28] Differential pumping systems were invented to lower the pressure stage by stage on the way of photoelectrons to the analyzer, resulting in lower collision rates of electrons with gas molecules. Electron lens was later assembled with differential pumping stages, so as to further enhance the signal collection efficiency. Years after the birth of ambient-pressure XPS (AP-XPS), it was developed for the first time at the synchrotron radiation source in Lawrence Berkeley National Laboratory (LBNL).[29] AP-XPS is benefited by synchrotron not only because the exceedingly strong X-ray flux allows spectrum acquisition to be substantially faster than Mg or Al anodes, but also since the tunable incident energy permits structural analysis at different depths. Currently, photoelectron transmission is significantly promoted with the upgrade of the instrument to the third generation, leading to higher signal-to-noise ratio and shorter data acquisition time.[30] AP-XPS has vastly demonstrated its advances in various applications, for example analyzing surface segregation of bimetallic nanocatalysts during reactions[31,32] and probing the reaction kinetics in electrochemical cells.[33]

1.3 Model Catalysts

The rapid development of nanoscience and nanotechnology in the past decade has permitted unprecedented control of dimension, size, morphology, and composition during nanoparticle synthesis. As catalytic reactions occur at the interface between catalysts and reactant mixtures, nanoparticles exhibit superior productivity to bulk catalysts given the same mass, which is attributed to the high surface-area-to-volume ratio of nanoparticles. Moreover, nanoparticle surfaces are populated by low-coordinated surface sites that are

considered as the real active sites in heterogeneous catalysis. Figure 1-1 shows the structure of some typical low-coordinated sites along with the terrace sites. Accordingly, model catalysts need to be extended from the well-defined (111), (100), and (110) crystal facets to nanoparticles of well-controlled size, shape, and composition, which could be prepared from colloidal synthesis.

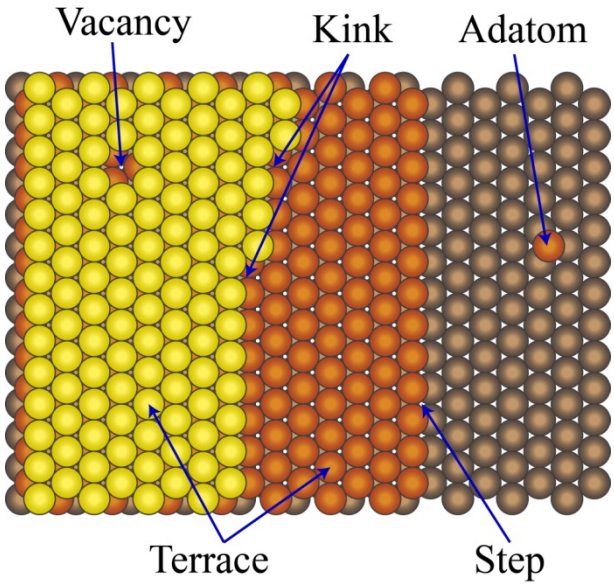

Figure 1-1. Ball model of a catalyst surface showing different types of surface sites.

However, STM studies on colloidal-synthesized nanoparticles are presently unfeasible, because the existence of polymer surfactants has reduced the conductivity and hence inhibited the acquisition of image with high resolution. Methods that can remove the capping agents also substantially roughen the substrate surface in the meantime, making metal nanoparticles difficult to differentiate from the corrugation on the rough substrate. Since STM is still limited to characterize well-controlled surfaces, model catalysts have been improved by growth of oxide layers on metal substrates,[34] deposition of metal islands on oxide substrates,[35-37] or deposition of one metal on another metal surface in vacuum.[37,38] After preparation, these model catalysts are transferred to the measurement chamber without loss of vacuum. In my studies, stepped metal single crystal surfaces, which are cut with a specific angle relative to the (111) surface, are used as the model catalyst to mimic nanoparticles. The high concentration of step sites present on stepped single crystals can represent the great number of low-coordinated sites on nanoparticle catalysts. Local structural changes at the step sites are monitored by means of HP-STM, to visualize the reconstruction at the real catalyst surfaces.

The field of heterogeneous catalysis has seen the advantages of bimetallic catalysts in activity, selectivity, and stability over the past half a century.[39-41] Such distinct properties of

bimetallic systems are attributed to electronic effect, which was proposed as early as in 1950s.[42] The electronic structure at a bimetallic surface is modified in two ways.[40] Irrespective of the formation of metal−metal solution or alloys by two metals, the average lengths of metal−metal bonds differ from the bond lengths in pure metal, giving rise to lattice strain in bimetallic catalysts. Furthermore, changes in the atomic orbital overlap in heteroatom bonds alter the electron band structure through the ligand effect. The modification in the electronic structure induces some unique behaviors of bimetallic materials such as surface enrichment and segregation during reactions,[31] since each reactant gas may preferentially bind with one metal. *In situ* structural characterization of bimetallic systems, specifically on surface composition and chemical states, are necessary to understand the electronic structure and hence the outstanding performances. Bimetallic nanoparticles whose size, shape, and composition are well controlled are employed as model catalysts, to explore the surface chemistry under a variety of chemical conditions.

1.4 Organization of Thesis

This thesis is organized in 9 chapters. The motivation of *in situ* characterization of transition metal model catalysts has been introduced in this chapter. Chapter 2 describes the experimental techniques, particularly the HP-STM and AP-XPS instruments, along with relevant tools equipped in UHV systems. Studies of surface reconstruction on Pt single crystal surfaces are presented from Chapter 3 to 6. Chapter 3 discusses the formation of nanometer-sized Pt oxide clusters that preferentially nucleates at step sites on Pt(557) induced by 1 Torr of O_2. Pt oxide is revealed as an important reaction intermediate for hydrogen oxidation and CO oxidation on Pt(557) in Chapter 4. Influence of step orientation on restructuring processes is explored under the CO-C_2H_4 mixture in Chapter 5. Chapter 6 investigates the preservation of hexagonal reconstruction and the surface mobility on Pt(100) under 1 Torr of C_2H_4 and 1 Torr of 1:1 C_2H_4-H_2 mixture. CO contamination from the background gases can incorporate at low C_2H_4 pressures is also observed. Chapter 7 focuses on the structural evolution on Cu(557) under reactive gases, which is compared with the phenomena on Pt(557). Finally, surface chemistry of three sorts of Pt-based bimetallic nanoparticle catalysts is studied in Chapter 8. Chapter 9 summarizes the results in the thesis and gives a brief outlook of the future directions.

1.5 References

(1) Somorjai, G. A.; Li, Y. *Introduction to Surface Chemistry and Catalysis*; 2nd ed.; Johns Wiley & Sons, Inc.: Hoboken, NJ, 2010.

(2) Ertl, G.; Knözinger, H.; Schüth, F.; Weitkamp, J. *Handbook of Heterogeneous Catalysis*; 2nd ed.; Wiley-VCH: Weinheim, 2008.

(3) Spencer, N. D.; Schoonmaker, R. C.; Somorjai, G. A. *Nature* **1981**, *294*, 643-644.

(4) Boudart, M. *Adv. Catal.* **1969**, *20*, 153-166.

(5) Somorjai, G. A.; Park, J. Y. *Angew. Chem., Int. Ed.* **2008**, *47*, 9212-9228.

(6) Longwitz, S. R.; Schnadt, J.; Vestergaard, E. K.; Vang, R. T.; Laegsgaard, E.; Stensgaard, I.; Brune, H.; Besenbacher, F. *J. Phys. Chem. B* **2004**, *108*, 14497-14502.

(7) Vang, R. T.; Wang, J.-G.; Knudsen, J.; Schnadt, J.; Stensgaard, I.; Besenbacher, F. *J. Phys. Chem. B* **2005**, *109*, 14262-14265.

(8) Moggridge, G. D.; Rayment, T.; Ormerod, R. M.; Morris, M. A.; Lambert, R. M. *Nature* **1992**, *358*, 658-660.

(9) Forsberg, J.; Duda, L. C.; Olsson, A.; Schmitt, T.; Andersson, J.; Nordgren, J.; Hedberg, J.; Leygraf, C.; Aastrup, T.; Wallinder, D.; Guo, J. H. *Rev. Sci. Instrum.* **2007**, *78*, 083110-083117.

(10) Shen, Y. R. *Nature* **1989**, *337*, 519-525.

(11) Gai, P. L.; Boyes, E. D.; Helveg, S.; Hansen, P. L.; Giorgio, S.; Henry, C. R. *MRS Bull.* **2007**, *32*, 1044-1050.

(12) Binnig, G.; Rohrer, H.; Gerber, C.; Weibel, E. *Appl. Phys. Lett.* **1982**, *40*, 178-180.

(13) Binnig, G.; Rohrer, H.; Gerber, C.; Weibel, E. *Phys. Rev. Lett.* **1982**, *49*, 57-61.

(14) Hallmark, V. M.; Chiang, S.; Rabolt, J. F.; Swalen, J. D.; Wilson, R. J. *Phys. Rev. Lett.* **1987**, *59*, 2879.

(15) Wintterlin, J.; Wiechers, J.; Brune, H.; Gritsch, T.; Höfer, H.; Behm, R. J. *Phys. Rev. Lett.* **1989**, *62*, 59.

(16) Binnig, G.; Rohrer, H.; Gerber, C.; Weibel, E. *Phys. Rev. Lett.* **1983**, *50*, 120.

(17) McIntyre, B. J.; Salmeron, M.; Somorjai, G. A. *Rev. Sci. Instrum.* **1993**, *64*, 687-691.

(18) Weeks, B. L.; Durkan, C.; Kuramochi, H.; Welland, M. E.; Rayment, T. *Rev. Sci. Instrum.* **2000**, *71*, 3777-3781.

(19) Lægsgaard, E.; Österlund, L.; Thostrup, P.; Rasmussen, P. B.; Stensgaard, I.; Besenbacher, F. *Rev. Sci. Instrum.* **2001**, *72*, 3537-3542.

(20) Rasmussen, P. B.; Hendriksen, B. L. M.; Zeijlemaker, H.; Ficke, H. G.; Frenken, J. W. M. *Rev. Sci. Instrum.* **1998**, *69*, 3879-3884.

(21) Rößler, M.; Geng, P.; Wintterlin, J. *Rev. Sci. Instrum.* **2005**, *76*, 023705.

(22) Kolmakov, A.; Goodman, D. W. *Rev. Sci. Instrum.* **2003**, *74*, 2444-2450.

(23) Tao, F.; Tang, D. C.; Salmeron, M.; Somorjai, G. A. *Rev. Sci. Instrum.* **2008**, *79*, 084101.

(24) Rider, K. B.; Hwang, K. S.; Salmeron, M.; Somorjai, G. A. *Phys. Rev. Lett.* **2001**, *86*, 4330-4333.

(25) Österlund, L.; Rasmussen, P. B.; Thostrup, P.; Lægsgaard, E.; Stensgaard, I.; Besenbacher, F. *Phys. Rev. Lett.* **2001**, *86*, 460-463.

(26) Merte, L. R.; Knudsen, J.; Eichhorn, F. M.; Porsgaard, S.; Zeuthen, H.; Grabow, L. C.; Lægsgaard, E.; Bluhm, H.; Salmeron, M.; Mavrikakis, M.; Besenbacher, F. *J. Am. Chem. Soc.* **2011**, *133*, 10692-10695.

(27) Montano, M.; Bratlie, K. M.; Salmeron, M.; Somorjai, G. A. *J. Am. Chem. Soc.* **2006**, *128*, 13229-13234.

(28) Starr, D. E.; Liu, Z.; Havecker, M.; Knop-Gericke, A.; Bluhm, H. *Chem. Soc. Rev.* **2013**, *42*, 5833-5857.

(29) Ogletree, D. F.; Bluhm, H.; Lebedev, G.; Fadley, C. S.; Hussain, Z.; Salmeron, M. *Rev. Sci. Instrum.* **2002**, *73*, 3872-3877.

(30) Grass, M. E.; Karlsson, P. G.; Aksoy, F.; Lundqvist, M.; Wannberg, B.; Mun, B. S.; Hussain, Z.; Liu, Z. *Rev. Sci. Instrum.* **2010**, *81*, 053106.

(31) Tao, F.; Grass, M. E.; Zhang, Y.; Butcher, D. R.; Renzas, J. R.; Liu, Z.; Chung, J. Y.; Mun, B. S.; Salmeron, M.; Somorjai, G. A. *Science* **2008**, *322*, 932-934.

(32) Tao, F.; Grass, M. E.; Zhang, Y.; Butcher, D. R.; Aksoy, F.; Aloni, S.; Altoe, V.; Alayoglu, S.; Renzas, J. R.; Tsung, C. K.; Zhu, Z.; Liu, Z.; Salmeron, M.; Somorjai, G. A. *J. Am. Chem. Soc.* **2010**, *132*, 8697-8703.

(33) Zhang, C.; Grass, M. E.; McDaniel, A. H.; DeCaluwe, S. C.; El Gabaly, F.; Liu, Z.; McCarty, K. F.; Farrow, R. L.; Linne, M. A.; Hussain, Z.; Jackson, G. S.; Bluhm, H.; Eichhorn, B. W. *Nat. Mater.* **2010**, *9*, 944-949.

(34) Kulawik, M.; Nilius, N.; Rust, H. P.; Freund, H. J. *Phys. Rev. Lett.* **2003**, *91*, 256101.

(35) Nilius, N.; Ernst, N.; Freund, H. J. *Phys. Rev. Lett.* **2000**, *84*, 3994-3997.

(36) Bowker, M. *Phys. Chem. Chem. Phys.* **2007**, *9*, 3514-3521.

(37) Schmid, M.; Kresse, G.; Buchsbaum, A.; Napetschnig, E.; Gritschneder, S.; Reichling, M.; Varga, P. *Phys. Rev. Lett.* **2007**, *99*, 196104.

(38) Ling, W. L.; Takeuchi, O.; Ogletree, D. F.; Qiu, Z. Q.; Salmeron, M. *Surf. Sci.* **2000**, *450*, 227-241.

(39) Campbell, C. T. *Annu. Rev. Phys. Chem.* **1990**, *41*, 775-837.

(40) Yu, W.; Porosoff, M. D.; Chen, J. G. *Chem. Rev.* **2012**, *112*, 5780-5817.

(41) Stamenkovic, V. R.; Fowler, B.; Mun, B. S.; Wang, G.; Ross, P. N.; Lucas, C. A.; Marković, N. M. *Science* **2007**, *315*, 493-497.

(42) Dowden, D. A.; Reynolds, P. W. *Discuss. Faraday Soc.* **1950**, *8*, 184-190.

Chapter 2

Experimental Methods

Abstract

This chapter describes the principles of HP-STM and AP-XPS, the two *in situ* techniques used for measurements in the following chapters. The design of the HP-STM and AP-XPS instruments is particularly illustrated with detailed diagrams. Supplementary techniques for the experiments in this thesis, including UHV and AES, are also briefly discussed.

2.1 Introduction

Structural investigation of catalyst surfaces under gases can be performed with HP-STM and AP-XPS, as discussed in the previous chapter, to acquire geometrical, electronic, and chemical information. Gas composition can be readily controlled by using high-purity gases. Clean metal crystal surfaces need to be prepared in UHV, since samples will be contaminated by adsorption of gases from background otherwise. On the basis of UHV systems, special design on the instruments is necessary to accommodate the ability to work at high gas pressures. Principles of STM and XPS, instrumental developments, and other relevant techniques are described in this chapter in detail.

2.2 High-Pressure Scanning Tunneling Microscopy

2.2.1 Principle of STM

Electron wave functions at the surface can quantum mechanically decay away from the surface, given a finite energy barrier between the material and the media. Overlap of wave functions of two surfaces can cause electrons to tunnel from one material to the other. However, because wave functions decay exponentially with the distance to the surface, only when the two surfaces are in close proximity (typically a few angstroms) of each other can electron tunneling happen. In STM experiments, a sharp tip is placed close to the sample surface. A positive bias on the sample induces tunneling electrons to flow from the filled tip states to empty sample states, as shown in Figure 2-1, whereas electrons tunnel from the filled sample states to the empty tip states at a negative sample bias. STM images represent a complex convolution of the geometry and the electronic structure at the surface, rather than simply the surface topography. As STM works on the basis of electron transport, only conductor and semiconductor surfaces can be imaged.

According to theoretic derivation, the tunneling current can be calculated by:[1-4]

$$I \propto V \cdot \exp\left(-Ad\sqrt{\Phi}\right)$$

where V is the bias voltage, d is the distance between the tip and sample, and Φ is the work function of the material. A is a constant that has an approximate value of 1.025 if d is in Å and Φ is in eV. For a typical value of 4 to 5 eV for the work function of most metals and semiconductors, the tunneling current decreases by an order of magnitude when the tip moves 1 Å away from the sample. As a result, tunneling solely occurs between the topmost layer of the sample and the tip apex atom, even though both the tip and the sample consist of numerous atoms.

Small sample bias is commonly used for imaging metal surfaces. Electrons usually tunnel elastically between the tip and the sample, having the kinetic energy equal to eV. Tunneling electrons with high energy can serve as the energy source to promote physical and chemical processes to happen at the surface, including rotation,[5] dissociation,[6] and so forth. Images acquired at high sample bias thus may not reflect the real surface structure, and artifacts induced by high-energy electrons may appear.

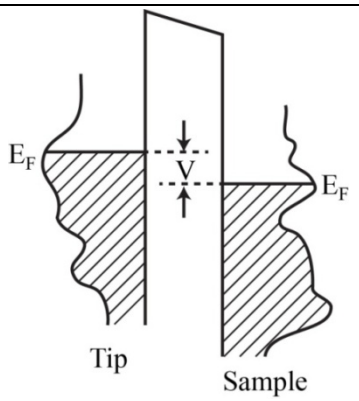

Figure 2-1. Principle of electron tunneling from tip to sample at a positive sample bias.

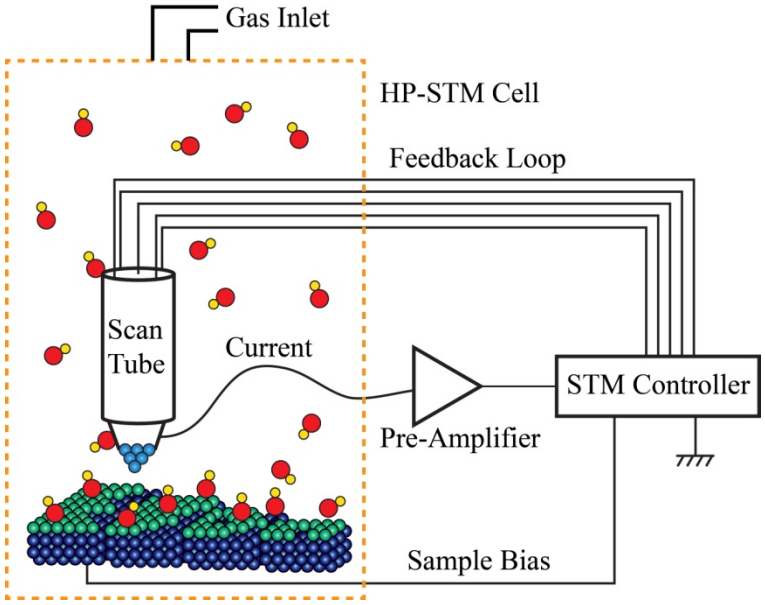

Figure 2-2. Diagram of STM working under the constant-current mode in a high-pressure cell. An electronic box and a feedback loop control the tip to scan across the sample surface at a tunneling current equal to a pre-set value. Green and blue balls on the sample represent atoms in the top layer and in the bulk, respectively, and red-yellow balls in the cell represent gas molecules. The sample surface is roughened upon gas adsorption. The tip is attached to the end of the scan tube, and a few atoms at the tip end are shown by light blue balls.

During scanning, the tip is attached to a scanner made of piezoelectric materials that undergo slight shape changes in response to applied electrical field. Lead zirconate titanate ceramics are the most frequently used piezoelectric materials in STM. The deformation of piezoelectric scan tube is able to regulate the tip motion in *x*-, *y*-, and *z*-directions at the

nanometer scale. Intuitively, when the tip scans across the surface at the same height, the current fluctuates because of the atomic corrugation at the surface. Surface structure can be imaged by recording changes in the tunneling current. This STM working mode, which is called constant-height mode, is not commonly used since the tip can be easily damaged by any big protrusions on the surface, and also because the error in the tip-sample distance can be large when the tunneling current is small. The alternative method to improve the performance is to use a feedback loop that governs the *z*-motion of the tip by comparing the measured current and a pre-set value, as in Figure 2-2. If the measured current is smaller than the pre-set value, the tip moves close to the sample so as to reach the pre-set value, and *vice versa*. In this constant-current mode, the trajectory of the tip is recorded during scans and the tip-sample distance is kept at the similar level.

2.2.2 The HP-STM Apparatus

The home-built HP-STM system upgraded in 2008 is consisted of two UHV chambers along with a load lock.[7] Figure 2-3 shows the overall schematic of the HP-STM instrument. The entire apparatus rests on a steel frame equipped with four air legs for damping of the building vibration. In addition, the frame prevents the instrument to move or fall in case of an earthquake since small earthquakes frequently happen in Berkeley. Each chamber is equipped with a mechanical pump (not drawn in the diagram), a turbo pump, and an ion pump. The load lock is pumped with the same mechanical pump and turbo pump as the STM chamber, but it has a separate small ion pump. The base pressure in the load lock and both chambers is kept at 10^{-10} Torr.

Sample preparation is facilitated by the combination of Ar^+ sputtering and annealing in the preparation chamber, as in Figure 2-4b. The sample resides on a stage made of alumina ceramics, on which a piece of Ta foil is placed to ground the sample. Ar^+ bombardment is performed with a sputter ion gun emitting high-energy electrons that ionize Ar gases filled in the preparation chamber. The sputter position can be calibrated with Ta_2O_5 foil which turns purple while being sputtered. Thoriated tungsten wire of 0.015 mm in diameter is used as the filament for electron bombardment heating. Each end of the filament is fixed on a Ta wire with 1 mm diameter inserted in an alumina ceramic tube. The Ta wires are then attached on Cu wires that go towards the feedthrough on the chamber. While annealing, sample temperature is measured by a pyrometer, and the sample is cooled by water flow in stainless steel coils connected onto the sample stage. Sample cleanness after the sputtering-annealing cycles is assessed by an Auger Cylindrical Mirror Analyzer. The big Auger analyzer is mounted on bellows retractable with a hydraulic pump, in order to leave enough space for sample stage rotation during sample transfer.

Samples are transferred between chambers and the load lock without loss of vacuum, through a transfer rod with a three-finger fork end. A wobble stick is employed to transfer the sample between the transfer rod and the HP-STM cell. A slit present in the back of the

sample holder matches the transfer arm, and two holes in the front of the holder fit the pins at the wobble stick end. Metal crystals of ~9 mm in diameter and ~0.7 mm in thickness are mounted on the sample holder with four pieces of small Ta foil and screws.

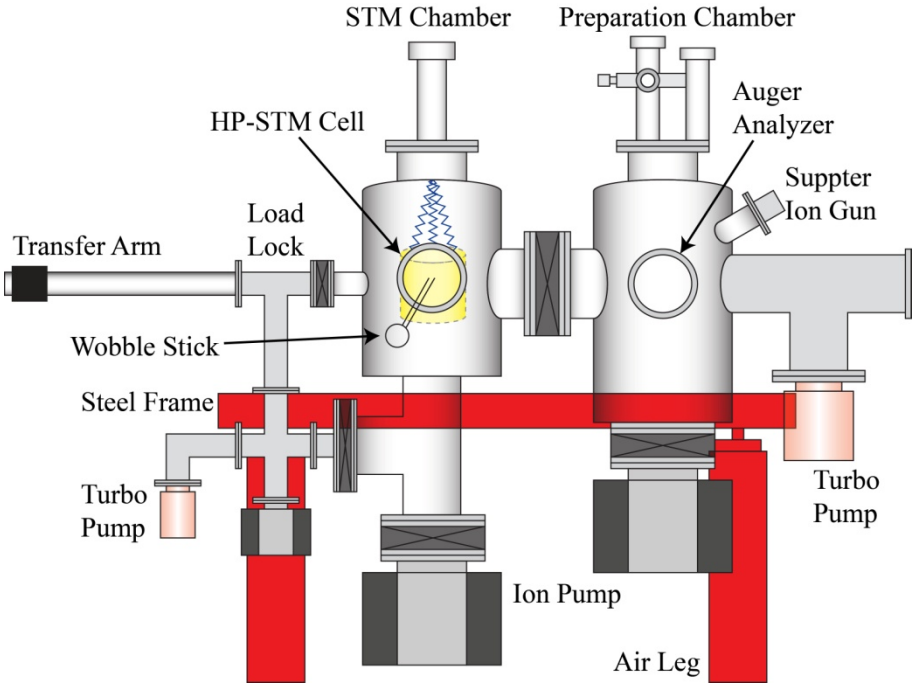

Figure 2-3. Diagram of the home-built HP-STM instrument upgraded in 2008.

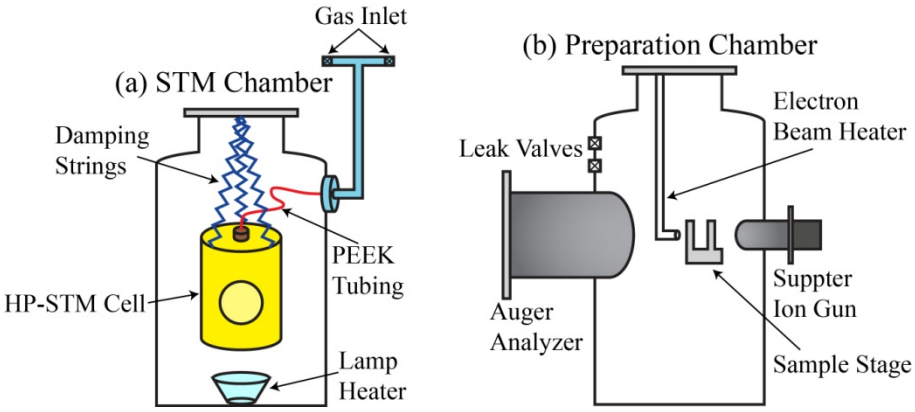

Figure 2-4. Schematics of (a) STM chamber and (b) preparation chamber. Connection between chambers and connection to pumps are not drawn.

Figure 2-4a displays that the STM chamber houses a high-pressure batch cell with a volume of ~19 cm^3 for HP-STM experiments. This cell is coated by gold in order to avoid reactions between the reactor initially fabricated of stainless steel and gases, since gold is

inert whereas stainless steel is active. A port, which can be closed by a bayonet seal, is opened in the front of the cell for sample transfer and tip exchange. Reactant gases are introduced into the system through polyether ether ketone (PEEK) tubes. The gas pressure is measured by a Baratron capacitance gauge, which has two channels with measurement range of 0.1~1000 mTorr and 0.1~1000 Torr. Therefore for experiments at above 0.1 mTorr, gases are filled only into the high-pressure cell while the STM chamber is still under high vacuum, whereas gases are filled into the whole STM chamber that is isolated from the rest of the instrument by gate valves at pressures below 0.1 mTorr. The high-pressure cell is hanged by strings in the STM chamber for vibration damping. A halogen lamp along with an elliptical reflector is installed at the bottom of the STM chamber for heating the sample during HP-STM measurements.

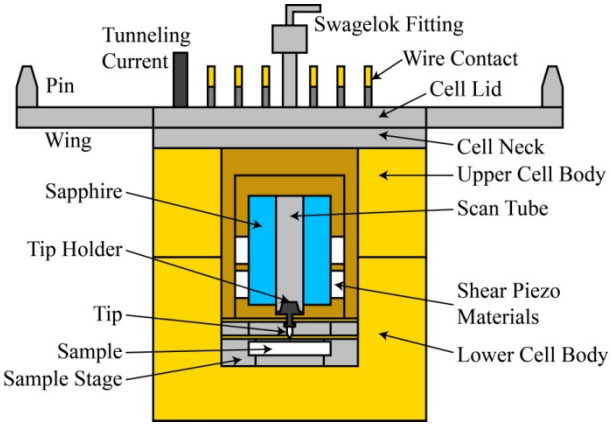

Figure 2-5. Cross-section view of the HP-STM cell coated by gold.

The STM body is assembled into the Au-coated HP-STM cell whose cross-section view is shown in Figure 2-5. The tip holder made of steel is attracted to a bowl-shaped SmCo magnet glued at the bottom of the piezoelectric scan tube. A hexagonal sapphire surrounds the scan tube, and six packs of shear piezoelectric materials are attached to the sapphire for coarse approach. The other side of the shear piezoelectric plates is glued onto the STM body frame. These shear piezoelectric plates control the forward and backward movement of the scan tube in the walker mode. 11 Kapton-coated Cu wires are used to connect the scan tube (5 wires) and the shear materials (6 wires) to the pins on top of the HP-STM cell. The pins are subsequently connected to feedthroughs on the STM chamber. The tunneling current wire is attached to the end of the scan tube close to the SmCo magnet.

Below the STM body, a sample stage is fastened through PEEK screws. Seven glass beads are precisely aligned between the sample stage and the STM body, in order to thermally isolate and electrically insulate the sample stage from the STM body by. The sample bias is put through a K-type thermocouple welded on the sample stage, which can also be used to measure the sample temperature during heating. The HP-STM system is

able to work at pressures up to 1000 Torr and at temperatures from 298 to 700 K.

Highly ordered pyrolytic graphite (HOPG) is used to calibrate the HP-STM. Figure 2-6 shows STM images of HOPG acquired in UHV both at low magnification exhibiting terraces and steps and at high magnification with atomic resolution. The *z*-movement of the scan tube is calibrated with the step height in Figure 2-6a, whereas movement in the *x*- and *y*-directions is calibrated with the periodicity in Figure 2-6b. Because interlayer interactions between graphite render two neighboring C atoms inequivalent, three-fold symmetry is observed in the atomically resolved STM image of HOPG, instead of the real honeycomb atomic packing. The STM image of HOPG hence directly evidences that STM measures surface electronic structure rather than surface topography.

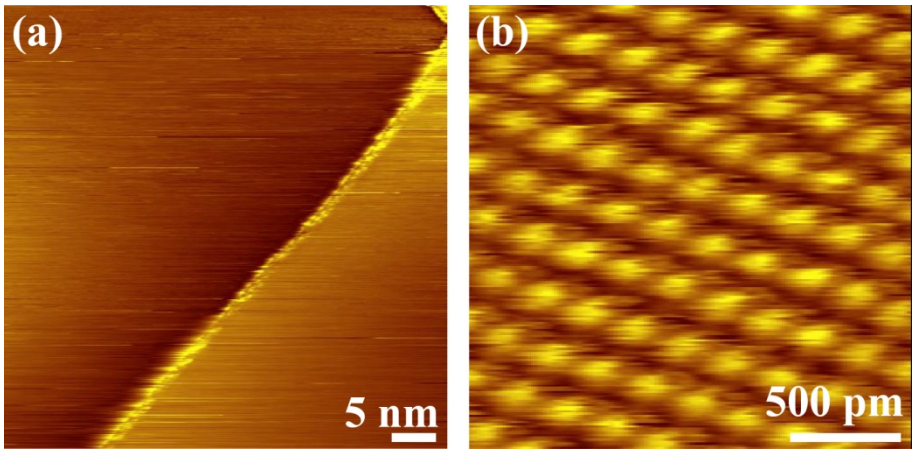

Figure 2-6. STM images of HOPG at (a) low and (b) high magnification. Flat terraces separated by a monatomic step are shown in (a), and the three-fold lattice is atomically resolved in (b).

2.3 Ambient-Pressure X-ray Photoelectron Spectroscopy

2.3.1 Principle of XPS

XPS works on the fundamental basis of the photoelectric effect that electrons are emitted from materials after adsorbing photons with high enough energy. X-rays from either metal anodes or synchrotron radiation are used as the excitation source for photoemission in XPS measurements. The kinetic energy of those ejected photoelectrons is measured. According to Figure 2-7, the corresponding binding energy of electrons in core levels or valence levels are given by:

$$E_B = h\nu - E_k - \Phi_a$$

where ν is the photon frequency, E_k is the electron kinetic energy, and Φ_a is the analyzer work function. Electrons at the Fermi level in the materials are set as having zero binding energy. An XPS spectrum is acquired by measuring the counts of photoelectrons per second as a function of binding energy. Peaks in XPS spectra are used for elemental

analysis of the surface. Like STM, XPS experiments also require conductive surfaces. Otherwise the surface is positively charged during measurements, impacting the yield of photoelectrons and shifting the binding energy upwards in the spectrum.

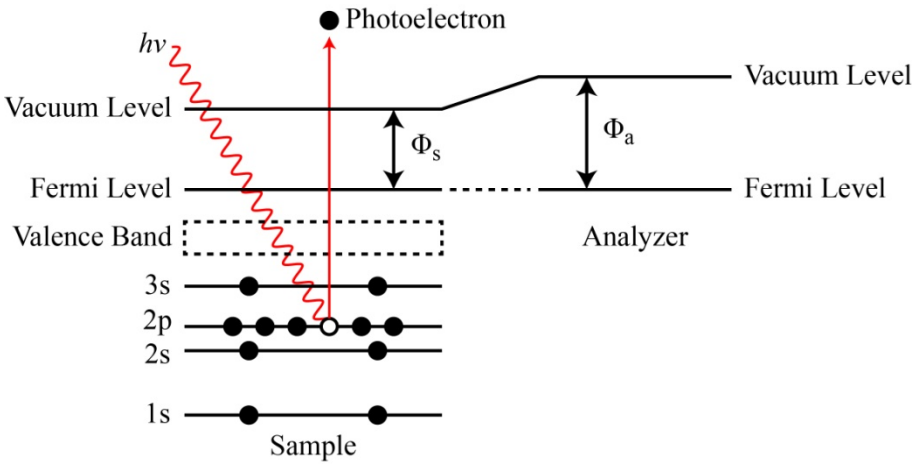

Figure 2-7. Schematic of the X-ray photoemission process and measurement of the kinetic energy of photoelectrons.

Additional to elemental identification, the atomic fraction of each constituent element and the relative concentration of different chemical states of the same element can also be quantitatively determined by XPS through peak integration and proper deconvolution. Since each atomic level has its own possibility to interact with photons, relative sensitive factors, also known as photoemission cross-sections, must be taken into consideration for quantification. Background needs to be subtracted in the spectrum prior to quantitative analysis. Inelastic scattering of electrons by surrounding atoms is mainly responsible for the energy loss and contributes to the spectrum background.

During XPS measurements, the incident beam intensity must be compromised such that spectra are acquired in a short time scale without causing any beam-induced effects. The enhanced beam intensity undoubtedly raises signal intensity and thus accelerates data acquisition. However, strong X-ray beam was observed to cause sample damage such as degradation of polymers,[8] decomposition of metal complexes,[9] and oxidation of metal.[10] Beam damage deserves special attention while using high-flux synchrotron X-ray source with small beam size.

2.3.2 The AP-XPS Apparatus

Figure 2-8 shows the schematic of the AP-XPS instrument, which was upgraded in 2010,[11] at Beamline 9.3.2 at Advanced Light Source (ALS) in LBNL. This apparatus consists of two UHV chambers for sample analysis and preparation, with the base pressures both in the 10^{-9} Torr range. The shielding in the analysis chamber was coated by gold as well, in

order to prevent reactions between the stainless steel alloy and reactive gases. Ion sputtering and LEED are installed in the preparation chamber for single crystal studies. The instrument is equipped with two transfer rods, one to transfer samples between two chambers and the other to transfer between the preparation chamber and the load lock. A hemispherical analyzer located at the end of the workstation measures the kinetic energy of photoelectrons. X-ray is delivered into the analysis chamber through a 100 nm thick Si_3N_4 window. Samples are mounted onto a ceramic button heater on the sample holder using Ta clips, with type K thermocouple wires underneath to measure the temperature. Gases are backfilled into the chambers through separated leak valves.

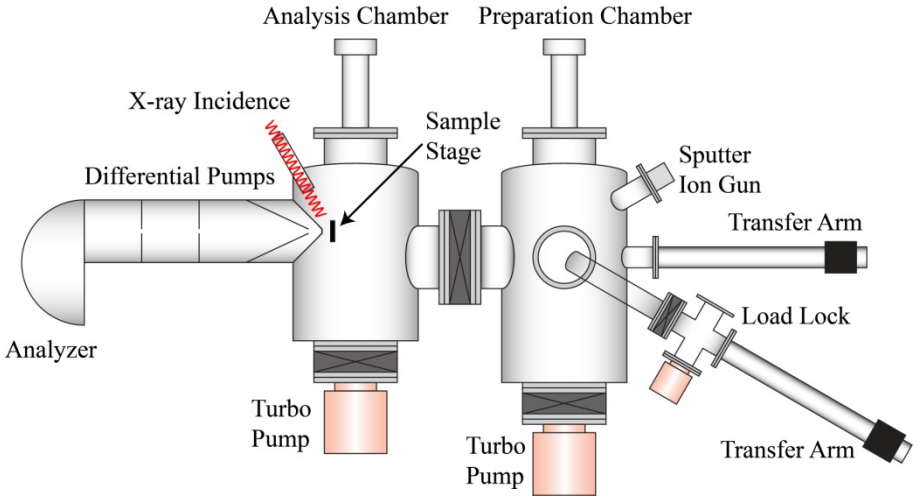

Figure 2-8. Schematic of the AP-XPS instrument at Beamline 9.3.2 in LBNL.

An integrated differential pumping system is located between the analysis chamber and the analyzer to reduce the pressure on the electron trajectory to the analyzer, thereby weakening the signal attenuation by gas scattering. In the front of the first differential pump is a nozzle with a small aperture placed close to the sample. The aperture size is optimized for trade-off between measurement efficiency and the upper pressure limit. Larger apertures increase the acceptance angle of electrons and hence the counts of electrons at the analyzer, whereas smaller apertures increase the pressure differentials and thus the maximum pressure in the analysis chamber. A sample-nozzle distance larger than twice the nozzle diameter suffices to ensure that the pressure drop due to the aperture does not impact any chemical processes at the sample surface, since the sample pressure is over 95% of the chamber pressure.[11,12] In order to further enhance the pumping efficiency, the cone of the second pumping stage is placed close to the first nozzle, which results in a steeper pressure gradient.

Since photoelectrons expand radially once entering the low pressure side of the apertures, electron lenses are coupled with differential pumps to increase photoelectron

transmission and signal intensity. The improved transmission also allows a smaller X-ray spot size down to 0.5 mm. The smaller beam in turn permits a smaller nozzle aperture and a higher maximum pressure. XPS spectra can be recorded in this AP-XPS apparatus at pressures up to several Torr with low X-ray incident flux that effectively alleviates beam damage.

2.4 UHV Systems

Well-characterized sample surfaces are required for *in situ* STM and XPS studies before the introduction of reactive gases. Since Pt and Cu surfaces are susceptible towards adsorption of CO, O_2, NO, and hydrocarbon contaminants present in the lab, UHV is necessary to prepare clean metal surfaces for high-pressure experiments. Based on the kinetic theory of gases, the flux F of molecules sticking onto the surface varies with pressure and temperature, which can be given by:[13]

$$\mathrm{F} = \frac{\mathrm{N_A p}}{\sqrt{2\pi \mathrm{MRT}}} = 3.51 \times 10^{22} \frac{\mathrm{p}}{\sqrt{\mathrm{MT}}}$$

where p is pressure in Torr, T is temperature in K, and M is molar mass of molecules in g/mol. At a base pressure of 10^{-10} Torr in the instruments, even assuming every particle hitting the sample stays on the surface, adsorbates will not saturate on the sample surface within approximately 10,000 seconds, or 2 hour 45 minutes. This time is long enough to cool and transfer the sample after preparation, and to examine the sample cleanness prior to any gas introduction.

2.5 Auger Electron Spectroscopy

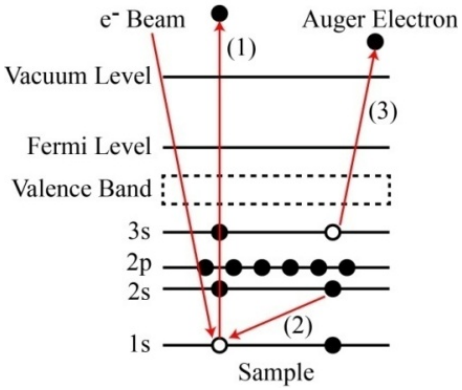

Figure 2-9. Illustration of the Auger process. After the incident electron beam causes the emission of a core-level electron (1), an electron in the outer levels fills the vacancy (2), leading to the generation of an Auger electron (3).

In the HP-STM apparatus, the absence of any C or O contaminants on Pt and Cu crystal surfaces after cleaning is examined with AES. During the Auger process, as shown in

Figure 2-9, the material is excited by a high-energy electron beam, usually 1.5 to 3 keV, which is able to eject electrons from the core levels like X-rays. The vacancy left behind can be filled by an electron in an outer core or valence level. Energy released in this process leads to the emission of another electron in outer levels, called Auger electrons. Similar to XPS, AES is also a surface-sensitive technique since the IMFP of Auger electrons is as large as a few atomic layers. Elemental analysis is performed based on the kinetic energy of Auger electrons, which does not depend on the energy of the incident electron beam. In addition, because the signal of Auger electrons sometimes obscure with the background contributed by secondary and backscattered electrons, derivative of electron counts over energy is hence taken in order to differentiate Auger signal from background.

2.6 References

(1) Bardeen, J. *Phys. Rev. Lett.* **1961**, *6*, 57-59.

(2) Tersoff, J.; Hamann, D. R. *Phys. Rev. Lett.* **1983**, *50*, 1998-2001.

(3) Tersoff, J.; Hamann, D. R. *Phys. Rev. B* **1985**, *31*, 805-813.

(4) Chen, C. J. *Introduction to Scanning Tunneling Microscopy*; 2nd ed.; Oxford University Press, 2008.

(5) Stipe, B. C.; Rezaei, M. A.; Ho, W. *Science* **1998**, *279*, 1907-1909.

(6) Stipe, B. C.; Rezaei, M. A.; Ho, W.; Gao, S.; Persson, M.; Lundqvist, B. I. *Phys. Rev. Lett.* **1997**, *78*, 4410-4413.

(7) Tao, F.; Tang, D. C.; Salmeron, M.; Somorjai, G. A. *Rev. Sci. Instrum.* **2008**, *79*, 084101.

(8) Yoshihara, K.; Tanaka, A. *Surf. Interface Anal.* **2002**, *33*, 252-258.

(9) Cleary, D. A.; Baer, D. R. *Chem. Mater.* **1992**, *4*, 112-116.

(10) Jiang, P.; Porsgaard, S.; Borondics, F.; Köber, M.; Caballero, A.; Bluhm, H.; Besenbacher, F.; Salmeron, M. *J. Am. Chem. Soc.* **2010**, *132*, 2858-2859.

(11) Grass, M. E.; Karlsson, P. G.; Aksoy, F.; Lundqvist, M.; Wannberg, B.; Mun, B. S.; Hussain, Z.; Liu, Z. *Rev. Sci. Instrum.* **2010**, *81*, 053106.

(12) Starr, D. E.; Liu, Z.; Havecker, M.; Knop-Gericke, A.; Bluhm, H. *Chem. Soc. Rev.* **2013**, *42*, 5833-5857.

(13) Somorjai, G. A.; Li, Y. *Introduction to Surface Chemistry and Catalysis*; 2nd ed.; Johns Wiley & Sons, Inc.: Hoboken, NJ, 2010.

Chapter 3

Formation of Nanometer-sized Platinum Oxide Clusters on a Stepped Pt(557) Single Crystal Surface Induced by Oxygen

(This chapter covers similar materials as in Zhu, Z. *et al.*, *Nano Lett.* **2012**, *12*, 1491-1497 – reproduced with permission, copyright 2012 American Chemical Society.)

Abstract

This chapter focuses on studies of oxygen-induced restructuring processes on a stepped Pt(557) single crystal surface, at O_2 pressures up to 1 Torr at 298 K. HP-STM has revealed that nanometer-sized clusters are created on Pt(557) under 1 Torr of O_2, and AP-XPS has identified these clusters as surface Pt oxide. The appearance of clusters is preceded by the formation of one-dimensional chain structures at step edges. By using a Pt(111) surface as a reference, step sites were found as the nucleation centers for the formation of surface oxide clusters. These surface oxide clusters disappear and the stepped structure is restored on Pt(557) after evacuating O_2 to the 10^{-8} Torr range. While dosing 10^{-7} Torr of O_2 onto the clean Pt(557) surface, only O_2 chemisorption is observed. Imaging the Pt(557) surface with +2.0 V sample bias under 10^{-7} Torr of O_2 can lead to formation of kink sites, because tunneling electrons provide energy for Pt atoms to diffuse along steps. Changes in the surface oxide concentration in response to variations in the O_2 gas pressure are repeatable for several cycles. The results that small clusters are initiated at step sites only at high pressures demonstrate the importance of *in situ* characterization of stepped Pt catalysts under reaction conditions.

3.1 Introduction

Heterogeneous catalysts usually contain a large amount of low-coordinated sites such as steps, kinks, and vacancies, which have long been considered as the active sites during catalytic reactions. These low-coordinated sites can influence activity and selectivity of reactions, because they strongly bind with reactants and readily break chemical bonds.[1-7] In addition, a high concentration of unsaturated surface sites can promote substrate reconstruction in response to adsorbed molecules, giving rise to step coalescence,[8-10] microfaceting,[11] and cluster formation.[12]

Recently developed *in situ* techniques have revealed the relation between catalyst structures and turnover rates under reaction conditions.[13-18] At high gas pressures and elevated temperatures, transition metal surfaces can undergo dramatic structural changes, as a result of the increased coverage of the gas molecules.[12,18-21] HP-STM can provide information regarding local surface electronic structure and morphology at the nanometer scale.[22,23] AP-XPS allows us to monitor the chemical states of both adsorbed reactants and underlying catalyst surfaces.[24,25]

Using these techniques, our group have recently reported that stepped Pt(557) and Pt(332) crystal surfaces break into nanometer-sized Pt clusters under 1 Torr of CO.[12] These Pt clusters on Pt(557) and Pt(332) were in triangle and parallelogram shapes, respectively. Such surface restructuring was reversible, since clusters disappeared and steps reformed after the CO gas was removed. The formation of Pt clusters occurred simultaneously with the growth of a high-binding energy component in the Pt 4f XPS spectra, which was attributed to low-coordinated Pt atoms at cluster edges bonded with CO. Step sites played a central role in inducing the formation of clusters on Pt surfaces, since no clusters were observed on Pt(111) crystal surface under similar CO pressures.[26]

O_2 can oxidize coordinatively unsaturated Pt surfaces at high gas pressures, which also causes profound changes in Pt surface structure. The variety of surface platinum and oxygen chemical states from chemisorption through to surface Pt oxide[27-32] has called for a detailed *in situ* investigation of the Pt−O system. In this chapter, the interaction between oxygen and a stepped Pt(557) surface at pressures from 10^{-7} to 1 Torr and at 298 K was investigated by HP-STM and AP-XPS. It was found that in the presence of 1 Torr of O_2, a one-dimensional (1D) chain structure forms first at the step edges, and clusters of approximately 1 nm in size subsequently cover the surface. These clusters are identified as a surface Pt oxide phase by means of AP-XPS. Comparative studies on Pt(111) demonstrate that clusters preferentially form at the step edges at 1 Torr, whereas direct oxidation of terraces is kinetically limited. After evacuating O_2 to the 10^{-8} Torr range, most of the clusters disappear in STM images and the surface oxide component in XPS spectra is attenuated. The concentration of surface oxide along with the oxygen coverage could repeatably vary with the O_2 pressure for several cycles.

3.2 Experimental Section

All the STM experiments were carried out in a home-built HP-STM system described in the previous chapter.[33] The HP-STM system consists of a 19 cm^3 Au-coated STM batch cell that is able to work at pressures of up to 1000 Torr. The STM cell is integrated into a UHV chamber with a base pressure of 10^{-10} Torr. A load lock and another UHV chamber for sample preparation (base pressure also 10^{-10} Torr) are combined in the system.

The Pt(557) and Pt(111) crystals were cleaned through repeated cycles of 1000-eV Ar^+ sputtering at 3×10^{-5} Torr at 298 K for 20 min, oxygen annealing at 5×10^{-8} Torr at 923 K for 3 min and subsequent vacuum annealing at 1073 K for 5 min. The Pt crystals were cooled down to 298 K at a rate of 1 K/sec after the final annealing step. Before STM experiments, the sample cleanliness was confirmed by the absence of carbon and oxygen in AES (PHI 15-255G double pass cylindrical mirror analyzer).

STM experiments at pressures lower than 10^{-7} Torr were performed by directly dosing the O_2 gas into the STM chamber, which is separated from the rest of system by gate valves. At pressures above 10^{-7} Torr, a bayonet seal was used to isolate the STM cell from the system and simultaneously maintain the STM chamber under vacuum. STM images were recorded using commercial $Pt_{0.8}Ir_{0.2}$ tips with diameters of 0.25 mm (Bruker AFM probes). The imaging condition is +0.2 V sample bias and 0.1 nA tunneling current unless specifically noted in the figure caption.

AP-XPS experiments were performed on a Scienta 4000 HiPP workstation at Beamline 9.3.2 of ALS in LBNL.[34,35] The base pressure of this instrument is maintained at 10^{-9} Torr. XPS survey scans were performed to ensure the absence of impurities on the Pt crystal surfaces prior to gas introduction. Pt 4f and O 1s core level spectra were recorded with incident X-ray photon energies of 340 eV and 800 eV, respectively, in order to generate photoelectrons with similar kinetic energies (~270 eV). Controlling the kinetic energy of the detect electrons ensures the same probing depth for both elements.[36] The Pt 4f region was also studied with 475 eV incident photon energy to detect deeper surface layers. The energy positions of all XPS spectra were calibrated relative to the Fermi edge (set at 0 eV) recorded with the same incident photon energy.

3.3 Results and Discussion

3.3.1 Clean Pt(557)

Figure 3-1a shows a model of a stepped Pt(557) single crystal surface. The Pt(557) surface has six-atom wide face-centered cubic (fcc) (111)-type terraces and monatomic high (100)-type steps, therefore being denoted as a 6(111) × (100) structure.[37] The STM image of Pt(557) taken in UHV is displayed in Figure 3-1b. From the STM image, the average terrace width of clean Pt(557) is measured as 1.6 nm, which is close to the calculated value of 1.4 nm based on the crystal structure. This deviation in terrace widths between theoretical and measured values is due to thermal drift during STM scans.

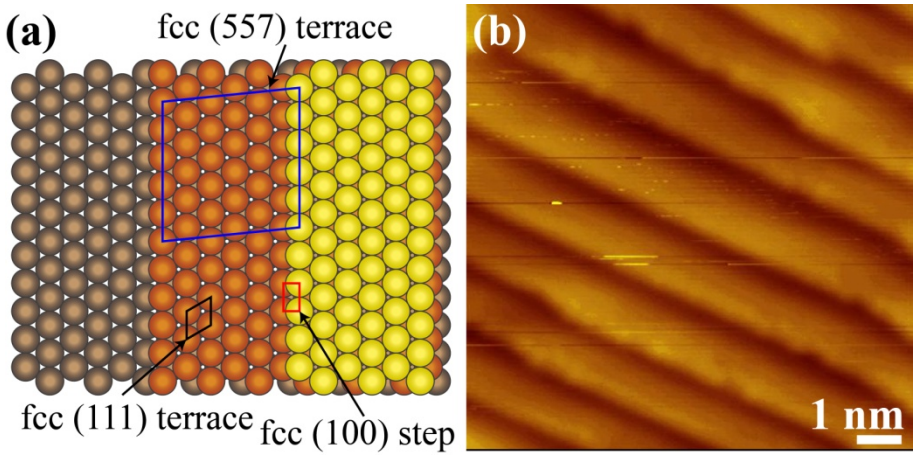

Figure 3-1. (a) Ball model of a Pt(557) surface. Light yellow, orange, and gray balls represent the top, second, and third layer of Pt atoms, respectively. (b) STM image of Pt(557) taken under UHV (10^{-10} Torr). The measured average terrace width is 1.6 nm.

3.3.2 High Pressures of O_2

The Pt(557) surface structure under 1 Torr of O_2 evolves with exposure time. 30 min after introducing 1 Torr of O_2, ordered stripes are resolved on portions of the step edges that remain straight, as in Figure 3-2a. The line profile in the inset illustrates that the stripes consist of a periodic array of brightness maxima with 250 pm periodicity on average, close to the Pt−Pt distance in the crystal lattice. This structure likely corresponds to a 1D Pt oxide chain, which was reported to form at edges of stepped Pt crystals under high oxygen coverage, based on XPS measurements and theoretical calculations.[27,30] Figure 3-2a has thus provided direct proof for the existence of 1D oxides on a stepped Pt surface. A few bright elongated structures with an average length of 1.0 nm and an average height of 0.16 nm also form near the Pt oxide chains. As the exposure time to 1 Torr of O_2 is extended to 2 h, numerous clusters of ~1 nm in diameter, which are roughly aligned along the original steps, cover the majority of the Pt(557) surface, as shown in Figure 3-2b. The order of clusters and the appearance of bright islands suggest that the clusters are formed by the growth from the 1D oxide chain into a complete overlayer. Further increasing the O_2 pressure to 10 Torr results in a disordered layer of clusters on Pt(557). The clusters formed under high pressures of O_2 are ascribed to a two-dimensional (2D) surface Pt oxide phase.

The assignment of clusters to surface Pt oxide is supported by AP-XPS experiments in which a Pt(557) crystal was exposed to different O_2 pressures. Figure 3-3a displays the Pt 4f core level spectra of Pt(557) recorded with 340 eV photon energy in UHV and under 2 h exposure to 1 Torr of O_2. Both the location of the Pt $4f_{7/2}$ peak at 71.0 eV and the spin-orbit splitting of 3.3 eV agree with literature values.[38,39] At 1 Torr of O_2, an additional component appears at 71.6 eV with a core level shift (CLS) of +0.6 eV, as marked in Figure

3-3a and more clearly shown in the difference spectrum in Figure 3-3b. This Pt peak is attributed to surface oxide clusters based on the Pt 4f binding energy, because surface oxides with similar Pt 4f CLS can be formed by exposing stepped or kinked Pt single crystal surfaces to O_2.[28-30] Given that the Pt $4f_{7/2}$ CLS is +1.0-1.3 and +2.2-2.9 eV for PtO and PtO_2, respectively,[39-42] no bulk Pt oxide has formed under our experimental conditions. In addition, the position of the dips in the difference Pt 4f spectra at 70.6 eV (-0.4 eV CLS) agrees with Pt atoms in the surface layer,[29,30,39] which demonstrates that the oxide forms at the expense of surface Pt atoms.

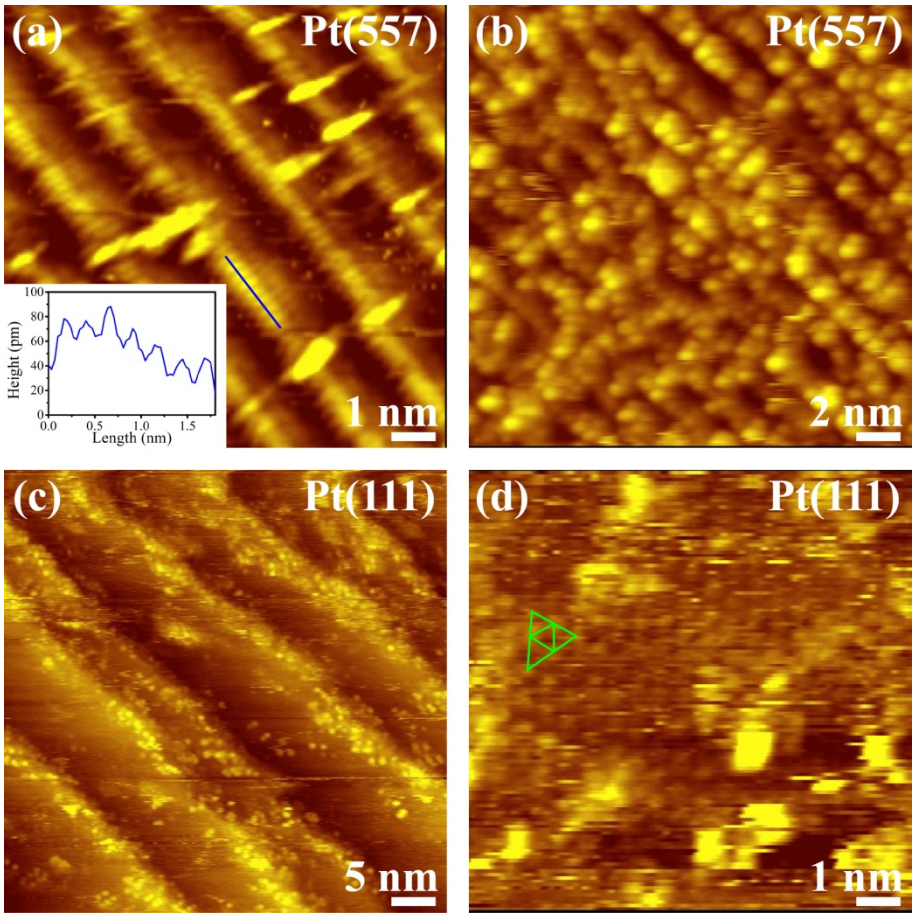

Figure 3-2. STM images of Pt(557) taken in 1 Torr of O_2 (a) 30 min and (b) 2 h after continuous exposure of the clean Pt(557) to O_2 gas. A periodic 1D chain structure is resolved at the step edges in (a) with the inset showing the line profile, while in (b) disordered clusters of approximately 1 nm in size cover the surface roughly following the original step direction. (c) and (d): Low and high magnification STM images of Pt(111) (the few steps indicate a miscut of approximately 1º), acquired after 1.5 h exposure to 1 Torr of O_2. Numerous nanometer-sized clusters accumulate close to the steps on the upper terraces in (c). The chemisorbed oxygen p(2 × 2) pattern, marked by green triangles, is resolved in (d) between clusters on Pt(111) terrace.

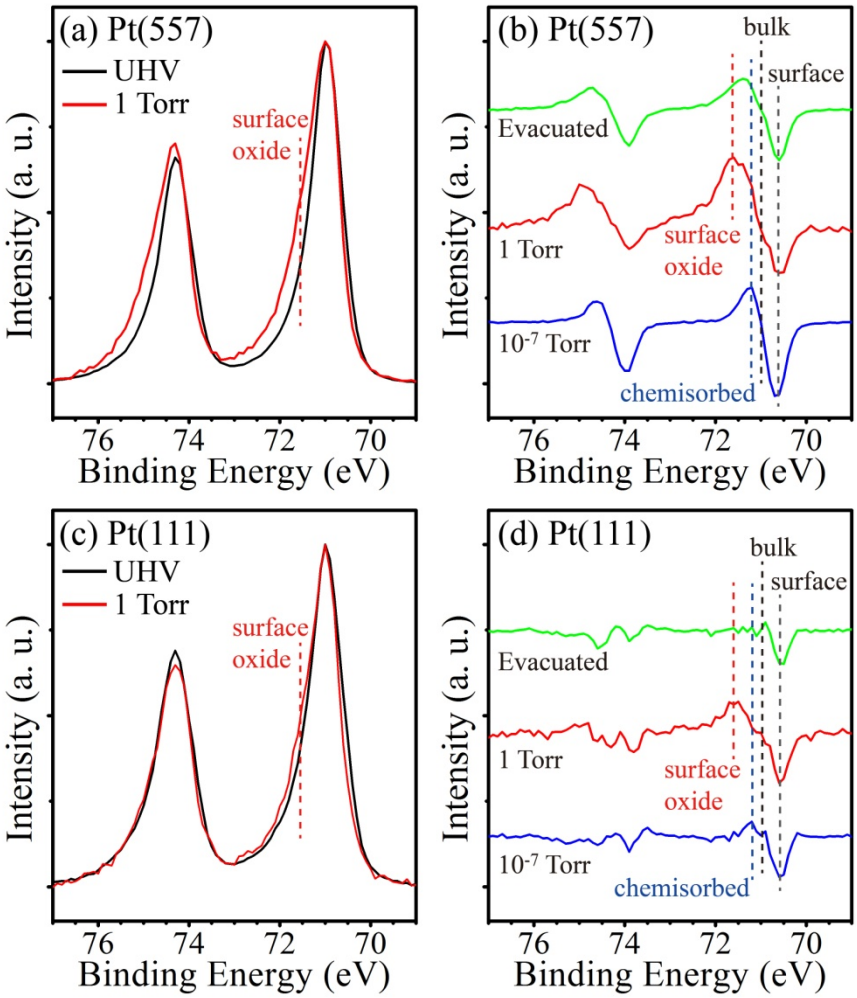

Figure 3-3. (a) Pt 4f spectra of Pt(557) recorded in UHV and under 2 h exposure to 1 Torr of O_2. A shoulder representing surface Pt oxide arises at +0.6 eV CLS. (b) Difference Pt 4f spectra of Pt(557) acquired under exposure to 10^{-7} Torr of O_2 for 2 h, 1 Torr of O_2 for 2 h, and 1.5 h after evacuation to 2×10^{-8} Torr of O_2 with respect to clean Pt(557) in UHV as the reference, in order to clearly show the XPS peak evolution. The enhancement at +0.2 eV CLS at 10^{-7} Torr shows that only oxygen chemisorption occurs. The surface oxide shoulder at 1 Torr is now evident in the difference spectrum at +0.6 eV CLS, whose intensity decreases after O_2 evacuation. (c) Pt 4f spectra of Pt(111) acquired in UHV and under exposure to 1 Torr of O_2 for 2 h. The Pt(111) has a less pronounced surface oxide shoulder than Pt(557), illustrating the relatively high activity of the stepped surface for the formation of the surface oxide phase. (d) Difference Pt 4f spectra of Pt(111) obtained under the same conditions as those in (b) using clean Pt(111) in UHV as the reference. The XPS spectra of Pt(111) evolve similarly to those of Pt(557), but to a less degree owing to the lower step density. All the spectra were recorded with 340 eV photon energy at 298 K and binding energies were calibrated to the Fermi level at 0 eV under the same conditions.

During the growth of surface Pt oxide clusters on Pt(557) to 1 Torr of O_2, the Pt oxide component does not shift in position in Pt 4f spectra, as in Figure 3-4a. The same Pt 4f peak position indicates that the Pt oxide grows from 1D to 2D without significant changes in chemical structure. However, the intensity of the Pt oxide component becomes twice stronger when the exposure time to 1 Torr of O_2 increases from 40 min to 2 h, which accords with the growth of the Pt oxide clusters in STM images. In addition, the oxygen coverage on Pt(557), measured by integration of Pt 4f and O 1s peak areas (both recorded with ~270 eV kinetic energy photoelectrons) and a subsequent calibration using the oxygen coverage of 0.25 ML on Pt(111) at 10^{-7} Torr,[43-46] increases with exposure time as well. Figure 3-4b shows that the oxygen coverage reaches 0.79 ML within 40 min of introducing 1 Torr of O_2 and slowly increases to 0.93 ML in 2 h.

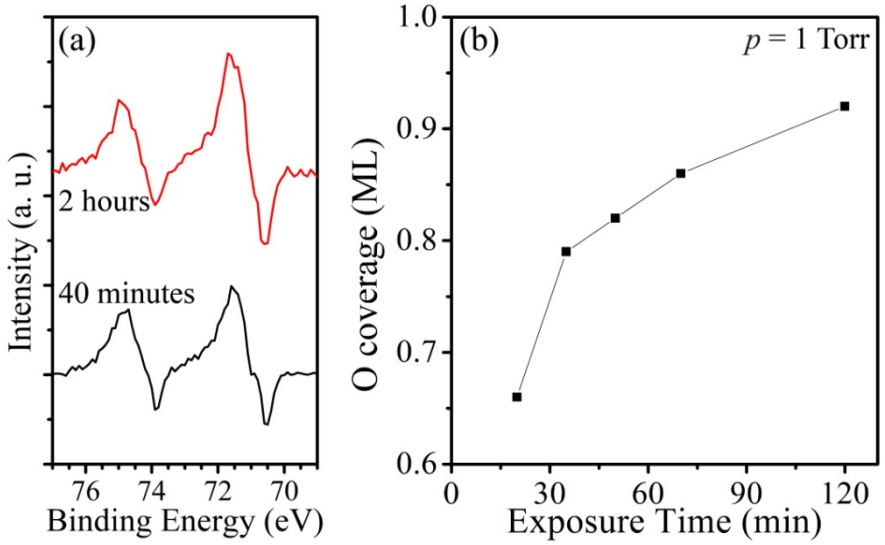

Figure 3-4. (a) Difference Pt 4f spectra of Pt(557) taken (black) 40 min and (red) 2 h after introducing 1 Torr of O_2, with respect to the clean Pt 4f spectrum in UHV. The surface oxide component remains at 71.6 eV but grows in intensity, indicating the similar chemical structure of 1D and 2D surface oxide. (b) Increase of the oxygen coverage on Pt(557) with exposure time to 1 Torr of O_2, which is indicative of the slow growth of surface Pt oxide.

Another major concern of AP-XPS experiments involves the beam-induced oxidation of metal surfaces.[47] In order to rule out the effect of X-ray beam on oxidizing the Pt(557) surface, a new set of spectra were acquired at another position after staying at the initial position for 2 h. Figure 3-5 displays the two Pt 4f spectra after subtracting the reference Pt 4f spectrum in UHV. The blue spectrum at the new position is similar to the red spectrum at the old position, in both the energy and especially intensity of the surface Pt oxide peak.

Had beam-induced oxidation occurred, the red spectrum recorded at the initial position should show a more prominent surface Pt oxide peak. X-ray beam effect is therefore negligible in these experiments.

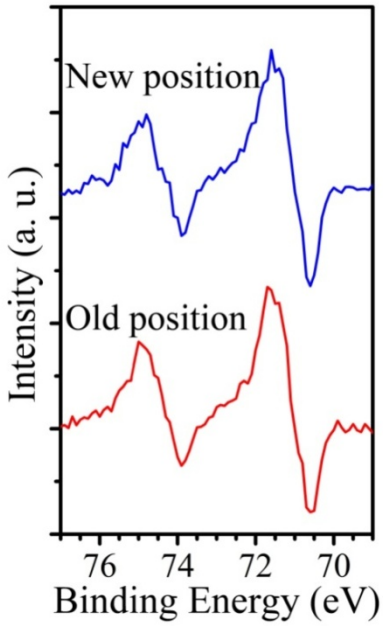

Figure 3-5. Difference Pt 4f spectra of Pt(557) under 1 Torr of O_2 using clean Pt(557) in UHV as the reference. The red spectrum was acquired after keeping recording XPS spectra for 2 h at the same sample position upon introducing O_2. Immediately after the red spectrum, the blue spectrum was obtained at a new position that had not been hit by X-ray. As the two spectra are similar, no X-ray beam damage occurs.

In order to investigate the role of steps in creating clusters, changes of the Pt(111) surface structure in the presence of O_2 were studied as well. Figure 3-2c, acquired 1.5 h after filling the HP-STM cell with 1 Torr of O_2, shows that a number of clusters have accumulated near the steps edges. The presence of steps on the Pt(111) crystal is due to a miscut angle of approximately 1º, which results in terraces of 12 nm wide on average. Although a few clusters appear on inner terraces, over 90% of the nanometer-sized clusters are located less than 2 nm away from the step edges. This phenomenon is consistent with literature reports that indicate cluster nucleation begins at step sites,[48] owing to the high mobility and activity of low-coordination Pt atoms. Growth of 2D surface Pt oxide is thus more likely to occur on Pt(557) because of the high step density as well as the narrow terrace width. Direct oxidation of Pt(111) terraces by O_2, in contrast, occurs slowly at similar pressures at 298 K, and was reported to happen only above 520 K.[49] By zooming in on the terraces, a hexagonal pattern marked by the green triangles in Figure 3-2d is resolved between clusters. The periodicity of the hexagonal pattern is 590 pm, which

corresponds to a chemisorbed oxygen p(2 × 2) structure. Since a p(2 × 1) order is the precursor state of Pt oxide on Pt(111) terraces when Pt(111) is oxidized by strong oxidants,[50] the p(2 × 2) chemisorption pattern in turn substantiates the slow kinetics of oxidation on terraces.

Pt 4f spectra of Pt(111) also demonstrate the low activity of terraces relative to steps in forming surface oxide. As shown in Figure 3-3c,d, exposure to 1 Torr of O_2 for 2 h also results in a new component on Pt(111) at 71.6 eV (+0.6 eV CLS), the same binding energy as the surface oxide component on Pt(557). The surface oxide formed on Pt(111) is thus indistinguishable from the oxide clusters on Pt(557) based on the same Pt 4f CLS value. However, the increase of intensity at 71.6 eV for Pt(111) on exposure to 1 Torr of O_2 is only one third of the increase observed on Pt(557), which accords well with the smaller number of clusters seen on Pt(111) by STM. This difference between Pt(111) and Pt(557) is undoubtedly the consequence of the lower step density on Pt(111).

3.3.3 O_2 Evacuation

Figure 3-6a shows that 1.5 h after evacuating O_2 from 1 Torr to 10^{-8} Torr, almost all the 2D surface Pt oxide clusters disappear with steps forming again on the Pt(557), although some of the steps are no longer as straight as they originally were on the clean Pt(557) surface in Figure 3-1b. The 1D oxide chains are not observed at the step edges in Figure 3-6a. Nevertheless, it can be due to the inevitable loss of resolution by the blunting of the STM tip after exposure to 1 Torr of O_2 for several hours. Similarly, very few clusters are left on Pt(111) 1.5 h after O_2 evacuation, as in Figure 3-6b. The removal of surface Pt oxide can be observed by XPS as well. As shown by difference Pt 4f spectra of the Pt(557) in Figure 3-3b, evacuation of the XPS chamber from 1 Torr to 2×10^{-8} Torr of O_2 causes a significant decrease in intensity of the oxide component at 71.6 eV. Figure 3-3d reveals that the peak at 71.6 eV has also nearly disappeared on Pt(111), accompanied by the disappearance of clusters in the STM images.

The disappearance of the 2D oxide clusters with O_2 evacuation is worth discussing. Given that Pt oxide decomposition and oxygen desorption both occur slowly on Pt at 298 K[51] and that a thin Pt oxide film is thermodynamically more stable than bulk Pt oxide,[52] it would be surprising that the 2D oxide has decomposed within 1.5 h of O_2 gas removal. The reactions between surface Pt oxide and background gases (CO and H_2) are likely responsible for removing the 2D oxide, because CO can quickly reduce surface Pt oxide even at 273 K.[30,32] Reactions of the 2D oxide with H_2 and CO on Pt(557) are further studied with HP-STM and AP-XPS, which reveals that the surface Pt oxide clusters are indeed removed by H_2 at a low H_2:O_2 pressure ratio. These results will be discussed in detail the next chapter.

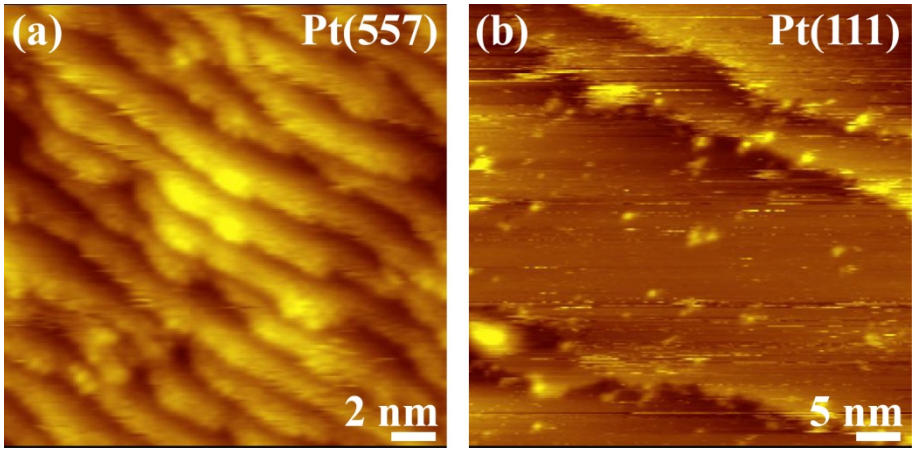

Figure 3-6. STM images of (a) Pt(557) and (b) Pt(111) 1.5 h after evacuating the HP-STM cell to 10^{-8} Torr. Most clusters have disappeared on both crystals, and steps on Pt(557) as well as terraces on Pt(111) reappear.

3.3.4 Low Pressures of O_2

To further explore the reactivity of Pt step sites towards O_2, the Pt(557) surface structure at low O_2 pressures was investigated by means of direct dosing gases into the UHV chamber. When the clean Pt(557) crystal is exposed to 10^{-7} Torr of O_2 at 298 K, the nanometer-sized clusters are not formed. Instead, periodic bright spots are resolved at parts of the step edges, as revealed in Figure 3-7a. The average spacing of 580 pm between the bright spots is close to twice the Pt−Pt distance in the lattice. Although atomic information on the narrow terraces near the step bottom cannot be obtained owing to the large tip radius, the results agree with literature STM reports that O_2 only chemisorbs at Pt steps at low pressures.[6,53] O_2 adsorbs dissociatively at Pt step edges, with the chemisorption sites depending on the step geometry. Moreover, the difference Pt 4f spectrum in Figure 3-3b shows that 10^{-7} Torr of O_2 does not lead to the growth of the oxide component at 71.6 eV. Instead, the enhancement of the Pt $4f_{7/2}$ peak is located at 71.2 eV (+0.2 eV CLS). This shift is due to the Pt atoms bonded with chemisorbed oxygen on Pt(111) terraces.[28,30] O_2 therefore dominantly chemisorbs on Pt(557) at low pressures. No clusters are observed on Pt(557) until the O_2 pressure is raised to 10^{-3} Torr. Figure 3-7b shows that several ~1 nm large clusters are formed exclusively at the Pt step edges under 10^{-3} Torr of O_2, which verifies that step sites are the nucleation center of Pt oxide clusters. As for the Pt(111) surface, consensus has already been reached in the literature that O_2 chemisorbs after dissociation below 10^{-6} Torr at 298 K.[43-46,50]

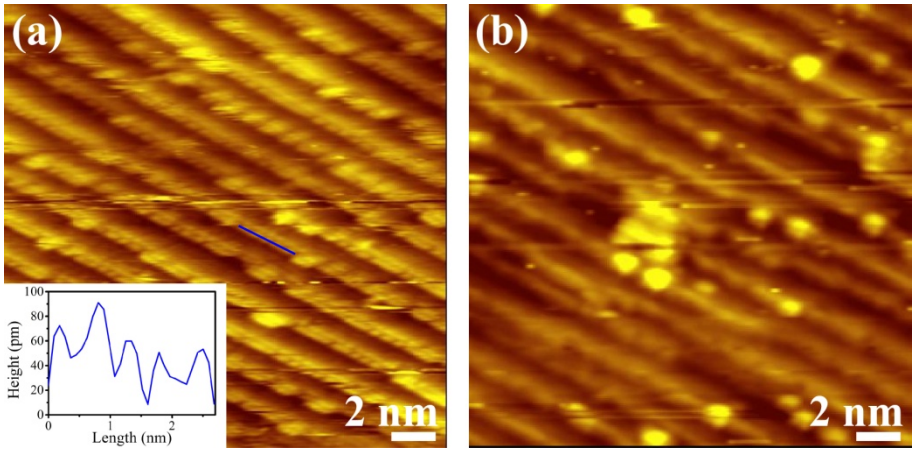

Figure 3-7. STM images of Pt(557) at O_2 pressures of (a) 10^{-7} Torr and (b) 10^{-3} Torr. Chemisorbed patterns are resolved as bright dots at parts of the step edges at 10^{-7} Torr, with a line profile of the chemisorbed structure shown in the inset. At 10^{-3} Torr, a few bright clusters start to accumulate at step edges.

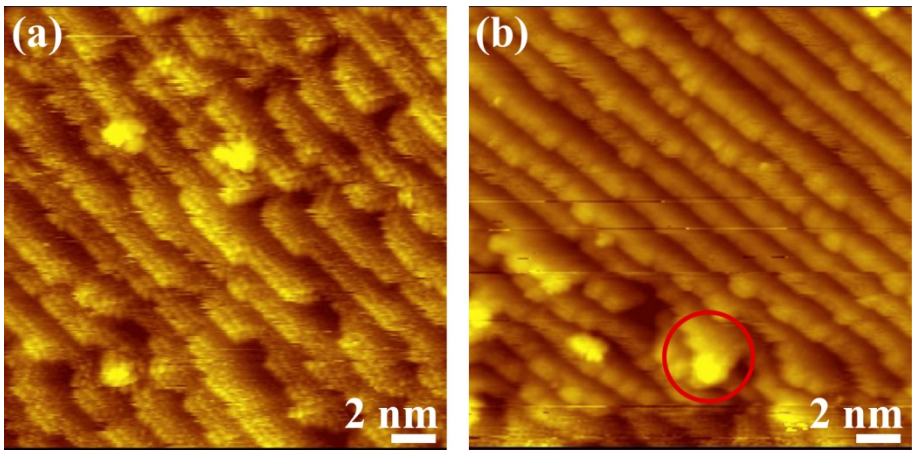

Figure 3-8. STM images of Pt(557) under 10^{-7} Torr of O_2 showing the formation of kink sites. (a) A number of kink sites are formed while imaging the surface with +2.0 V sample bias and 0.1 nA tunneling current, because the tunneling electrons can provide energy for Pt atoms to diffuse. (b) The surface is imaged at +0.2 V sample bias after putting a +5.0 V pulse at the position highlighted by the red circle. Kink sites are mostly formed where the +5.0 V pulse is added.

It is noteworthy that in Figure 3-7a, chemisorption of oxygen does not change terrace widths and step heights at 298 K. In our previous report regarding CO adsorption on Pt(557), the terrace widths and step heights are doubled under 5×10^{-7} Torr at 298 K.[12] However, at elevated temperatures, O_2 could yield such doubling transition on Pt(111)

vicinal surfaces.[9,10] This discrepancy is potentially due to a kinetic energy barrier for Pt atom to diffuse along steps. The repulsion between chemisorbed CO molecules can lower the Pt diffusion barrier, whereas the binding of oxygen atoms to two or more step Pt atoms may impede Pt diffusion. Tunneling electrons, whose energies are determined by the sample bias, can be an energy source for physical and chemical processes to occur at low temperatures.[54,55] Figure 3-8a shows that, when imaging the Pt(557) surface under 10^{-7} torr of O_2 with +2.0 V sample bias instead of +0.2 V, a large amount of kink sites are created. In contrast, no kink sites formation are observed on clean Pt(557) in UHV with +2.0 V or even higher sample bias, which illustrates that the existence of chemisorbed oxygen atoms is essential in causing step coalescence. The STM tip was then moved to a new region where the steps were originally straight. A +5.0 V pulse was put onto the surface and the region was subsequently imaged with +0.2 V bias. As in Figure 3-8b, kink sites are only observed around the pulse position marked by the red circle, whereas steps still remain straight in other parts of the region which are not close to the pulse.

3.3.5 Quantitative XPS Analysis

Quantitative curve fits of Pt 4f core level spectra of the Pt(557) were performed, so as to gain further insight into the Pt oxide formation at high pressures of O_2. Pt 4f spectra were recorded with photon energies of 340 and 475 eV, which produce photoelectrons of ~270 and ~405 eV kinetic energy, respectively. ~270 eV kinetic energy corresponds to an IMFP of ~0.6 nm and ~405 eV kinetic energy corresponds to ~0.8 nm.[36] The thickness of Pt oxide can then be roughly estimated by measuring the oxide intensity at each surface depth. Selected Pt 4f spectra, which were acquired at 1 Torr and after O_2 evacuation to 2×10^{-8} Torr, are displayed along with fitted peaks in Figure 3-9. These Pt 4f spectra were deconvoluted using asymmetric Voigt-type line-shapes, preceded by a subtraction of the Shirley-type background.[56] Four components, including bulk Pt (gray), surface Pt (-0.4 eV CLS, yellow), Pt bonded with chemisorbed oxygen (+0.2 eV CLS, blue), and surface oxides of Pt (+0.6 eV CLS, red) were used for peak fitting, and no other components were found to be necessary for a good fit. The CLS values of these components are determined from the difference Pt spectra in Figure 3-3b. Under both O_2 pressures, the intensity ratio of Pt oxide to bulk Pt is lower at 475 eV photon energy than at 340 eV. The Pt peak from the chemisorption phase which forms exclusively at the surface decreases in intensity with increasing probing depth as expected. The less intense oxide peak with deeper probing depth thereby implies that the Pt oxide is only enriched at surface. Although bulk PtO_2 and Pt_3O_4 are both thermodynamically stable at 298 K even at low O_2 pressures,[57,58] growth of surface oxide to form bulk oxide can be kinetically limited by the high energy barrier for oxygen diffusion into the Pt subsurface at 298 K.[59]

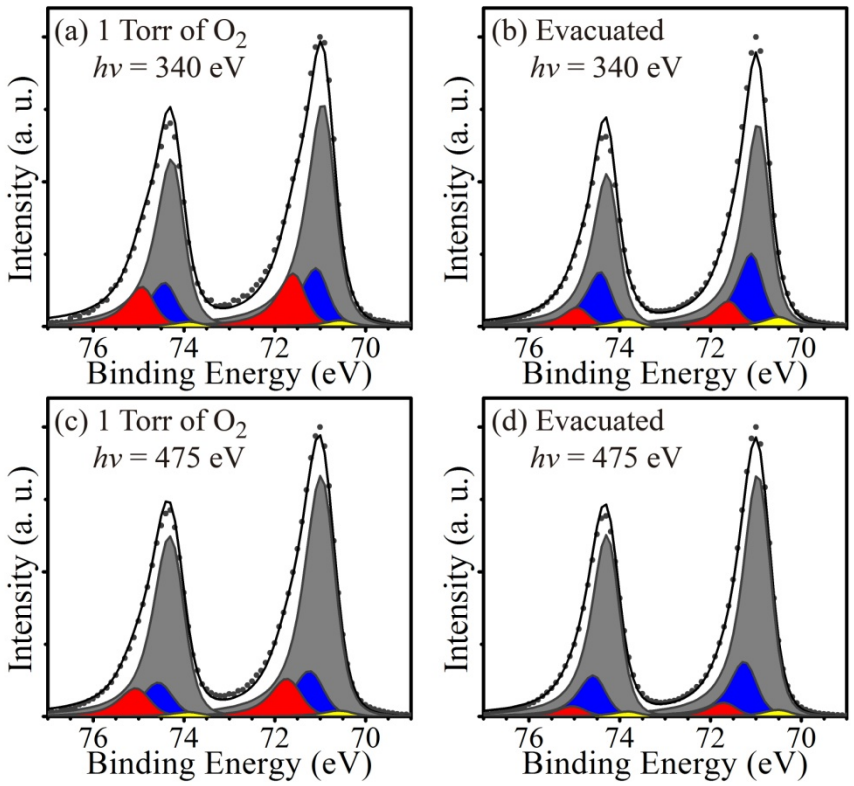

Figure 3-9. Pt 4f spectra of Pt(557) obtained at 298 K under 2 h exposure to 1 Torr of O_2 and 1.5 h after evacuation to 2×10^{-8} Torr with X-ray energies of 340 eV (probing depth ~0.6 nm) and 475 eV (probing depth ~0.8 nm). Gray, yellow, blue, and red components represent bulk Pt, surface Pt, Pt bonded with chemisorbed oxygen, and Pt in surface oxide, respectively. The black dots denote the raw data points and the gray lines are the fitted spectra (the summation of the gray, yellow, blue, and red components). The fitting results show that surface oxide decomposes upon O_2 evacuation (left to right), and that the oxide is only a surface phase (top to bottom).

The area ratio of Pt in oxide phase to total detected Pt on the Pt(557) sample was then determined by integrating the peak areas of Pt oxide and total Pt in the fitted Pt 4f spectra at both photon energies. The surface oxide concentration varies reversibly with switching between high and low pressures of O_2, as plotted by the red circles (~0.6 nm depth) and triangles (~0.8 nm depth) in Figure 3-10. At 10^{-3} Torr of O_2 when oxide clusters start to appear at Pt step sites in the STM images, the concentrations of Pt oxide at ~0.6 nm and ~0.8 nm depths are ~6% and ~4%, respectively. The respective Pt oxide ratios at ~0.6 nm and ~0.8 nm increase to ~15% and ~11% after introducing O_2 to 1 Torr, and then decrease to ~7% and ~4% upon evacuating to 2×10^{-8} Torr. Since the concentrations of Pt oxide determined by incident energy of 340 eV are always higher than those by 475 eV, the oxide clusters are obviously more populated at the surface. Re-introduction and re-evacuation of

O_2 to similar pressures change the Pt oxide concentration at ~0.6 nm depth to ~15% and ~8%, respectively. Similarly, at ~0.8 nm probing depth, the Pt oxide concentration increases to ~11% with re-introduction, followed by declining to ~5% after re-evacuation. Such variation trend in oxide concentration at the Pt(557) surface with changing O_2 pressures can be repeated for several cycles.

Moreover, the oxygen coverage on Pt(557) exhibits a similar variation in response to changes in O_2 gas pressures. At 10^{-7} Torr, the oxygen coverage on Pt(557) is 0.28 ML, and then slowly increases with O_2 pressure until 0.42 ML at 10^{-3} Torr. The oxygen coverage suddenly increases to 0.93 ML at 1 Torr. A similar experiment on Pt(111) gives the coverage of 0.48 ML at 1 Torr of O_2. The large difference in oxygen coverage between Pt(557) and Pt(111) is indicative of the higher activity of step sites than terrace sites in forming Pt oxide. After O_2 gas evacuation, the oxygen coverage on Pt(557) remains stable at 0.70 ML. However, this value is still larger than 0.28 ML after initial exposure to 10^{-7} Torr, because the Pt(557) surface inevitably turns rougher after the introduction-evacuation cycle of O_2. The oxygen coverage on Pt(557) increases to 1.05 ML upon re-introduction of O_2 to 1 Torr and decreases to 0.82 ML after re-evacuation. Changes in the oxygen coverage can also be repeated over several cycles.

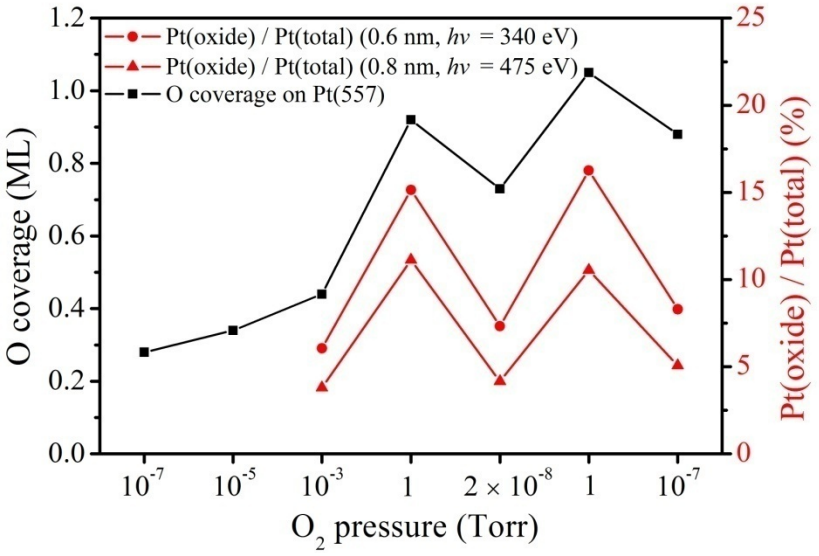

Figure 3-10. Changes in the surface Pt oxide concentration on Pt(557) in response to O_2 pressure variation, as measured with 340 eV (red circles) and 475 eV (red triangles) incident X-ray photon energies. The curves show that changes in the surface oxide concentration correlate with changes in the O_2 gas pressure. Black lines: Oxygen coverage on Pt(557) determined from Pt 4f and O 1s photoelectrons (both ~270 eV kinetic energy), after calibration with respect to the 0.25 ML p(2 × 2) structure formed on Pt(111) at 10^{-7} Torr of O_2. Oxygen coverage on Pt(557) varies with gas pressures in a similar trend to that of oxide concentration, but gradually increases as a result of surface roughening.

3.4 Conclusions

In conclusion, *in situ* STM and XPS studies were performed to monitor the structural and chemical evolution of a stepped Pt(557) surface induced by O_2 at 298 K. STM images illustrate that at 1 Torr, periodic 1D chains form initially at step edges, followed by the formation of nanometer-sized clusters that cover the entire Pt(557) surface, as O_2 exposure time increases. The clusters are identified as surface Pt oxide by the appearance of a high-binding energy component at +0.6 eV with respect to the metallic Pt peak in XPS spectra obtained under the same condition. The intensity of the surface Pt oxide component increases with exposure time, which agrees with the growth of 2D clusters in STM results. No X-ray beam induced surface oxidation is observed. In a comparative experiment on Pt(111), both HP-STM and AP-XPS demonstrate that low-coordinated step atoms are more active than terrace sites in reacting with O_2. Most clusters disappear on both Pt(557) and Pt(111) upon evacuation of O_2 to 10^{-8} Torr. Such dramatic structural changes on the stepped Pt(557) surface are seen only when the O_2 gas pressure reaches 1 Torr, whereas chemisorption occurs at low pressures such as 10^{-7} Torr. Step coalescence induced by O_2 can be observed under 10^{-7} Torr while imaging with +2.0 V or higher sample bias. The results indicate that it is important to study the structure of stepped Pt single crystal model catalysts under ambient pressures, not only since they can undergo dramatic structure changes in equilibrium with high-pressures of gas phase reactants, but also because the high structural flexibility of stepped Pt surfaces allows us to bridge the connection between surface structures and catalytic performances.

3.5 References

(1) Somorjai, G. A.; Li, Y. *Introduction to Surface Chemistry and Catalysis*; 2nd ed.; Johns Wiley & Sons, Inc.: Hoboken, NJ, 2010.

(2) Ertl, G.; Knözinger, H.; Schüth, F.; Weitkamp, J. *Handbook of Heterogeneous Catalysis*; 2nd ed.; Wiley-VCH: Weinheim, 2008.

(3) Hendriksen, B. L. M.; Ackermann, M. D.; van Rijn, R.; Stoltz, D.; Popa, I.; Balmes, O.; Resta, A.; Wermeille, D.; Felici, R.; Ferrer, S.; Frenken, J. W. M. *Nature Chem.* **2010**, *2*, 730-734.

(4) Zambelli, T.; Wintterlin, J.; Trost, J.; Ertl, G. *Science* **1996**, *273*, 1688-1690.

(5) Vang, R. T.; Honkala, K.; Dahl, S.; Vestergaard, E. K.; Schnadt, J.; Lægsgaard, E.; Clausen, B. S.; Nørskov, J. K.; Besenbacher, F. *Nat. Mater.* **2005**, *4*, 160-162.

(6) Gambardella, P.; Šljivančanin, Ž.; Hammer, B.; Blanc, M.; Kuhnke, K.; Kern, K. *Phys. Rev. Lett.* **2001**, *87*, 056103.

(7) Hammer, B.; Nielsen, O. H.; Nørskov, J. K. *Catal. Lett.* **1997**, *46*, 31-35.

(8) Batteas, J. D.; Dunphy, J. C.; Somorjai, G. A.; Salmeron, M. *Phys. Rev. Lett.* **1996**, *77*, 534-537.

(9) Hahn, E.; Schief, H.; Marsico, V.; Fricke, A.; Kern, K. *Phys. Rev. Lett.* **1994**, *72*, 3378-3381.

(10) Lindauer, G.; Légaré, P.; Maire, G. *Surf. Sci.* **1983**, *126*, 301-306.

(11) Sander, M.; Imbihl, R.; Schuster, R.; Barth, J. V.; Ertl, G. *Surf. Sci.* **1992**, *271*, 159-169.

(12) Tao, F.; Dag, S.; Wang, L. W.; Liu, Z.; Butcher, D. R.; Bluhm, H.; Salmeron, M.; Somorjai, G. A. *Science* **2010**, *327*, 850-853.

(13) Ackermann, M. D.; Pedersen, T. M.; Hendriksen, B. L. M.; Robach, O.; Bobaru, S. C.; Popa, I.; Quiros, C.; Kim, H.; Hammer, B.; Ferrer, S.; Frenken, J. W. M. *Phys. Rev. Lett.* **2005**, *95*, 255505.

(14) Montano, M.; Bratlie, K. M.; Salmeron, M.; Somorjai, G. A. *J. Am. Chem. Soc.* **2006**, *128*, 13229-13234.

(15) Grass, M. E.; Zhang, Y.; Butcher, D. R.; Park, J. Y.; Li, Y.; Bluhm, H.; Bratlie, K. M.; Zhang, T.; Somorjai, G. A. *Angew. Chem., Int. Ed.* **2008**, *47*, 8893-8896.

(16) Li, Y.; Liu, J. H.-C.; Witham, C. A.; Huang, W.; Marcus, M. A.; Fakra, S. C.; Alayoglu, P.; Zhu, Z.; Thompson, C. M.; Arjun, A.; Lee, K.; Gross, E.; Toste, F. D.; Somorjai, G. A. *J. Am. Chem. Soc.* **2011**, *133*, 13527-13533.

(17) Zheng, F.; Alayoglu, S.; Guo, J.; Pushkarev, V.; Li, Y.; Glans, P. A.; Chen, J. L.; Somorjai, G. A. *Nano Lett.* **2011**, *11*, 847-853.

(18) Hendriksen, B. L. M.; Frenken, J. W. M. *Phys. Rev. Lett.* **2002**, *89*, 046101.

(19) Österlund, L.; Rasmussen, P. B.; Thostrup, P.; Lægsgaard, E.; Stensgaard, I.; Besenbacher, F. *Phys. Rev. Lett.* **2001**, *86*, 460-463.

(20) Tao, F.; Dag, S.; Wang, L. W.; Liu, Z.; Butcher, D. R.; Salmeron, M.; Somorjai, G. A. *Nano Lett.* **2009**, *9*, 2167-2171.

(21) Thostrup, P.; Vestergaard, E. K.; An, T.; Lægsgaard, E.; Besenbacher, F. *J. Chem. Phys.* **2003**, *118*, 3724-3730.

(22) Somorjai, G. A.; Park, J. Y. *Angew. Chem., Int. Ed.* **2008**, *47*, 9212-9228.

(23) Vang, R. T.; Lægsgaard, E.; Besenbacher, F. *Phys. Chem. Chem. Phys.* **2007**, *9*, 3460-3469.

(24) Salmeron, M.; Schlögl, R. *Surf. Sci. Rep.* **2008**, *63*, 169-199.

(25) Starr, D. E.; Liu, Z.; Havecker, M.; Knop-Gericke, A.; Bluhm, H. *Chem. Soc. Rev.* **2013**, *42*, 5833-5857.

(26) Longwitz, S. R.; Schnadt, J.; Vestergaard, E. K.; Vang, R. T.; Laegsgaard, E.; Stensgaard, I.; Brune, H.; Besenbacher, F. *J. Phys. Chem. B* **2004**, *108*, 14497-14502.

(27) Bandlow, J.; Kaghazchi, P.; Jacob, T.; Papp, C.; Tränkenschuh, B.; Streber, R.; Lorenz, M. P. A.; Fuhrmann, T.; Denecke, R.; Steinrück, H. P. *Phys. Rev. B* **2011**, *83*, 174107.

(28) Günther, S.; Scheibe, A.; Bluhm, H.; Haevecker, M.; Kleimenov, E.; Knop-Gericke, A.; Schlögl, R.; Imbihl, R. *J. Phys. Chem. C* **2008**, *112*, 15382-15393.

(29) Held, G.; Jones, L. B.; Seddon, E. A.; King, D. A. *J. Phys. Chem. B* **2005**, *109*, 6159-6163.

(30) Wang, J. G.; Li, W. X.; Borg, M.; Gustafson, J.; Mikkelsen, A.; Pedersen, T. M.; Lundgren, E.; Weissenrieder, J.; Klikovits, J.; Schmid, M.; Hammer, B.; Andersen, J. N. *Phys. Rev. Lett.* **2005**, *95*, 256102.

(31) Li, W. X.; Österlund, L.; Vestergaard, E. K.; Vang, R. T.; Matthiesen, J.; Pedersen, T. M.; Lægsgaard, E.; Hammer, B.; Besenbacher, F. *Phys. Rev. Lett.* **2004**, *93*, 146104.

(32) Butcher, D. R.; Grass, M. E.; Zeng, Z.; Aksoy, F.; Bluhm, H.; Li, W.-X.; Mun, B. S.; Somorjai, G. A.; Liu, Z. *J. Am. Chem. Soc.* **2011**, *133*, 20319.

(33) Tao, F.; Tang, D. C.; Salmeron, M.; Somorjai, G. A. *Rev. Sci. Instrum.* **2008**, *79*, 084101.

(34) Grass, M. E.; Karlsson, P. G.; Aksoy, F.; Lundqvist, M.; Wannberg, B.; Mun, B. S.; Hussain, Z.; Liu, Z. *Rev. Sci. Instrum.* **2010**, *81*, 053106.

(35) Aksoy, F.; Grass, M. E.; Joo, S. H.; Jabeen, N.; Hong, Y. P.; Hussain, Z.; Mun, B. S.; Liu, Z. *Nucl. Instrum. Methods Phys. Res., Sect. A* **2011**, *645*, 260-265.

(36) Powell, C. J.; Jablonski, A. *NIST Electron Inelastic Mean Free Path Database, version 1.2*; National Institute of Standards and Technology: Gaithersburg, MD, 2010.

(37) Van Hove, M. A.; Somorjai, G. A. *Surf. Sci.* **1980**, *92*, 489-518.

(38) Moulder, J. F.; Stickle, W. F.; Sobol, P. E.; Bomben, K. D. *Handbook of X-ray Photoelectron Spectronscopy*; Perkin-Elmer Corporation: Eden Prarie, MN, 1992.

(39) Légaré, P.; Lindauer, G.; Hilaire, L.; Maire, G.; Ehrhardt, J. J.; Jupille, J.; Cassuto, A.; Guillot, C.; Lecante, J. *Surf. Sci.* **1988**, *198*, 69-78.

(40) Hecq, M.; Hecq, A.; Delrue, J. P.; Robert, T. *J. Less Common Met.* **1979**, *64*, P25-P37.

(41) Hilaire, L.; Guerrero, G. D.; Légaré, P.; Maire, G.; Krill, G. *Surf. Sci.* **1984**, *146*, 569-582.

(42) Peuckert, M.; Bonzel, H. P. *Surf. Sci.* **1984**, *145*, 239-259.

(43) Gland, J. L.; Sexton, B. A.; Fisher, G. B. *Surf. Sci.* **1980**, *95*, 587-602.

(44) Materer, N.; Starke, U.; Barbieri, A.; Döll, R.; Heinz, K.; Van Hove, M. A.; Somorjai, G. A. *Surf. Sci.* **1995**, *325*, 207-222.

(45) Parker, D. H.; Bartram, M. E.; Koel, B. E. *Surf. Sci.* **1989**, *217*, 489-510.

(46) Puglia, C.; Nilsson, A.; Hernnäs, B.; Karis, O.; Bennich, P.; Mårtensson, N. *Surf. Sci.* **1995**, *342*, 119-133.

(47) Jiang, P.; Porsgaard, S.; Borondics, F.; Köber, M.; Caballero, A.; Bluhm, H.; Besenbacher, F.; Salmeron, M. *J. Am. Chem. Soc.* **2010**, *132*, 2858-2859.

(48) Krasnikov, S. A.; Murphy, S.; Berdunov, N.; McCoy, A. P.; Radican, K.; Shvets, I. V. *Nanotechnology* **2010**, *21*, 335301.

(49) Miller, D. J.; Öberg, H.; Kaya, S.; Sanchez Casalongue, H.; Friebel, D.; Anniyev, T.; Ogasawara, H.; Bluhm, H.; Pettersson, L. G. M.; Nilsson, A. *Phys. Rev. Lett.* **2011**, *107*,

195502.

(50) Devarajan, S. P.; Hinojosa Jr, J. A.; Weaver, J. F. *Surf. Sci.* **2008**, *602*, 3116-3124.

(51) Weaver, J. F.; Chen, J.-J.; Gerrard, A. L. *Surf. Sci.* **2005**, *592*, 83-103.

(52) Campbell, C. T. *Phys. Rev. Lett.* **2006**, *96*, 066106.

(53) Feibelman, P. J.; Esch, S.; Michely, T. *Phys. Rev. Lett.* **1996**, *77*, 2257.

(54) Stipe, B. C.; Rezaei, M. A.; Ho, W. *Science* **1998**, *279*, 1907-1909.

(55) Stipe, B. C.; Rezaei, M. A.; Ho, W.; Gao, S.; Persson, M.; Lundqvist, B. I. *Phys. Rev. Lett.* **1997**, *78*, 4410-4413.

(56) Shirley, D. A. *Phys. Rev. B* **1972**, *5*, 4709-4714.

(57) Salmeron, M.; Brewer, L.; Somorjai, G. A. *Surf. Sci.* **1981**, *112*, 207-228.

(58) Seriani, N.; Pompe, W.; Ciacchi, L. C. *J. Phys. Chem. B* **2006**, *110*, 14860-14869.

(59) Gu, Z.; Balbuena, P. B. *J. Phys. Chem. C* **2007**, *111*, 9877-9883.

Chapter 4

Structure and Chemical State of the Pt(557) Surface during Hydrogen Oxidation and Carbon Monoxide Oxidation

(This chapter covers similar materials as in Zhu, Z. *et al.*, *J. Am. Chem. Soc.* **2013**, *135*, 12560-12563 – reproduced with permission, copyright 2013 American Chemical Society.)

Abstract

The structure of the Pt(557) surface under the H_2-O_2 mixture and the CO-O_2 mixture was investigated in this chapter. At 298 K, the surface Pt oxide clusters formed on Pt(557) by exposing to approximately 1 Torr of O_2 can readily react with H_2, and fully disappear when the H_2 partial pressure reaches 43 mTorr. Pt steps are restored after the surface Pt oxide clusters are removed by H_2. Under pure H_2 in the Torr range, the stepped structure is preserved. Water is detected as the product in the gas phase, which co-adsorbs with hydroxyl groups on Pt(557). A reference study using H_2O validates the presence of water adsorbates on the Pt(557) surface even at 10^{-7} Torr of H_2O. In the mixture of 1 Torr of CO and 1 Torr of O_2, CO-induced triangular clusters and double-sized steps are observed, whereas Pt oxide clusters are absent. The Pt(557) surface structure changes reversibly when switching the gas environment between O_2 and CO.

4.1 Introduction

A crucial question in heterogeneous catalysis involves the dependence of catalytic reactivity on the structure of the catalyst−reactant interface, and the identification of reaction intermediates and surface sites responsible for turnovers. The development of *in situ* techniques has provided great opportunities to explore these questions, by bridging the over 9 orders of magnitude pressure gap between traditional model catalytic studies (below 10^{-6} Torr) and industrial catalysis (at or above atmospheric pressures). HP-STM is a unique tool to investigate the catalyst surface reconstruction during reactions at the molecular level[1-8] and the highly mobile nature of atoms and molecules on catalytically active surfaces.[9-11] Spectroscopic techniques, especially AP-XPS, yield information on composition and oxidation states of surface species during reactions.[7-9,12-17]

Pt oxide was proposed to be an active phase on Pt surfaces during CO oxidation.[4,7,18] For example, CO oxidation is accelerated by almost 10 times on Pt(110) under O_2-rich conditions at 425 K, along with the formation of Pt oxide islands observed by *in situ* STM.[4] Switching the gas mixture into a CO-rich environment leads to the reduction of Pt oxide and simultaneously a strong decrease in CO production rate. Consequently, the oxidized Pt surface can be strictly correlated with the high catalytic activity. XPS results have revealed that the active Pt oxide on Pt(110) is similar to the oxide on as-prepared 1.5 nm Pt nanoparticles.[7] On other Pt surfaces, for instance the stepped Pt(332) surface, 1D PtO_2 chains at Pt steps are also highly active towards CO even at 220 K.[18]

Hydrogen oxidation was investigated in detail at low pressures and low temperatures. When H_2 is oxidized by O_2 at Pt surfaces in vacuum above 170 K, the water desorption temperature, the formation of hydroxyl groups (OH) via hydrogenation of chemisorbed oxygen atoms is the rate-limiting step:[19-21]

$$O(a) + H(a) \rightarrow OH(a) \quad (1)$$

$$OH(a) + H(a) \rightarrow H_2O(a) \rightarrow H_2O(g) \quad (2)$$

This reaction is autocatalytic below 170 K in vacuum, since in the presence of adsorbed water molecules, OH species can be produced through alternative reaction channels:[19-21]

$$H_2O(a) + O(a) \rightarrow 2OH(a) \quad (3)$$

$$2H_2O(a) + O(a) \rightarrow 2OH(a) + H_2O(a) \rightarrow 3OH(a) + H(a) \quad (4)$$

Despite these well-known mechanisms at low temperatures in vacuum, the mechanism under ambient pressures and temperatures is not well understood at the molecular level. The formation of Pt oxide, which can be stabilized at sufficiently high O_2 pressures, adds another parameter that needs to be considered.

This chapter follows the previous chapter by investigating the structure and chemical state of the Pt(557) surface under hydrogen oxidation and CO oxidation mixtures at 298 K. The surface Pt oxide formed on Pt(557) under near 1 Torr of O_2 is active in oxidation reactions. HP-STM has monitored the decrease in the Pt oxide coverage with the increase of H_2 partial pressures. Pt oxide can be fully removed on Pt(557) at H_2 partial pressures

below 50 mTorr. The reaction product, water, is detected to co-adsorb with hydroxyl groups on Pt(557). H_2 does not induce any structural changes on Pt(557) even at 1 Torr. Under the 1:1 CO-O_2 mixture at 2 Torr, the Pt(557) surface structure is dominated by CO, since CO-induced triangular clusters and doubling of terrace widths as well as step heights are observed. Pt oxide clusters, however, are absent at surface.

4.2 Experimental Section

STM measurements were performed in a home-built instrument containing a Au-coated high-pressure batch cell wherein reactant gases are introduced.[22] AP-XPS spectra were recorded at Beamline 9.3.2 at ALS in LBNL.[23] The Pt(557) crystal was cleaned via cycles of Ar^+ bombardment, annealing in O_2, and flashing to 1073 K in vacuum, as described in the previous chapter. The cleaning procedures were repeated till the level of contaminants was below the sensitivity of AES for HP-STM experiments and below the sensitivity of XPS for AP-XPS measurements. O_2 and H_2 were introduced separately through leak valves. All the HP-STM and AP-XPS experiments were carried out at 298 K.

4.3 Results and Discussion

4.3.1 Hydrogen Oxidation in the H_2-O_2 Mixture

Under 950 mTorr of pure O_2, the Pt(557) surface is covered by ~1 nm large surface Pt oxide clusters that are roughly aligned along the original step edges, as shown in Figure 4-1a. H_2 was added after the cluster overlayer had formed under O_2. The structural evolution of the Pt(557) surface with increasing H_2 partial pressures is monitored with STM, as displayed in Figure 4-1. The Pt oxide clusters are still distinguishable in the STM image after introducing 2 mTorr of H_2 (Figure 4-1b). At a higher H_2 partial pressure of 10 mTorr, the coverage of Pt oxide clusters becomes much smaller, with most of the remaining clusters decorating the Pt step edges (Figure 4-1c). When the H_2 partial pressure reaches 43 mTorr, the Pt oxide clusters have completely disappeared and Pt steps are restored (Figure 4-1d). Since these clusters can be readily removed at a low H_2:O_2 pressure ratio of 1:20, the high reactivity of Pt oxide towards H_2 agrees with literature reports that Pt oxide is active in hydrogen oxidation.[24-26] An induction period ranging from 10 to 80 min was reported for the reaction involving Pt oxide as the catalyst, with the length relying on the preparation of Pt oxide.[24] The imaging was started 15 min after introducing gases, and no changes in the surface structure were observed with reaction time. The induction period in our experiments, if it exists, should hence be shorter than 15 min.

In addition, under 950 mTorr of O_2 and 10 mTorr of H_2, a periodic pattern can be resolved at step edges on a small part of the surface where most clusters have been removed. Figure 4-2 shows the STM image of this periodic structure and the corresponding topography profile. The periodicity is measured as 580 pm, twice as the Pt−Pt distance. Although oxygen atoms chemisorb on the Pt step edges with the same periodicity,[6] this

pattern under the H_2-O_2 mixture is unlikely due to the oxygen chemisorption, because only chemisorbed water and OH groups are present under such condition, as described later in Figure 4-4. One possible explanation to this pattern is the 1D hydrogen bond chain of water molecules at the (100)-oriented Pt steps.[27] The hydrogen bond chain structure at step edges may also involve OH groups. Higher resolution and possibly theoretical calculations are demanded to establish an appropriate model this pattern.

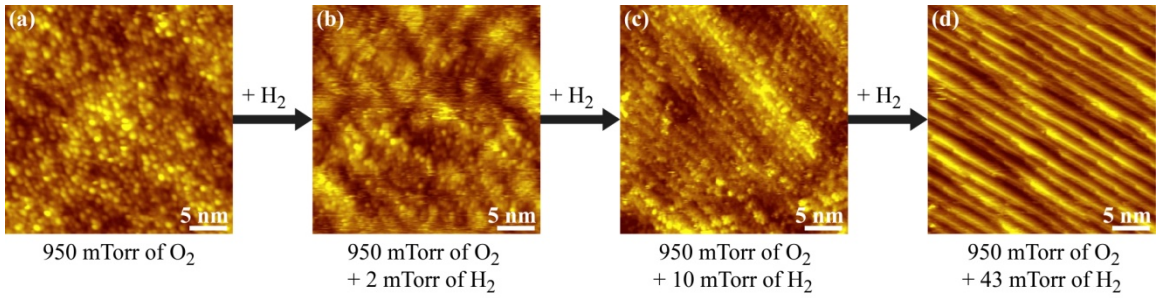

Figure 4-1. STM images of the Pt(557) surface. (a) Under 950 mTorr of O_2, the surface is covered by Pt oxide clusters approximately 1 nm in diameter. The clusters are roughly aligned along the step edges. (b-d) Under a mixture of 950 mTorr of O_2 and (b) 2 mTorr, (c) 10 mTorr, and (d) 43 mTorr of H_2, the coverage of Pt oxide decreases with increasing H_2 partial pressures until the Pt oxide clusters ultimately disappear.

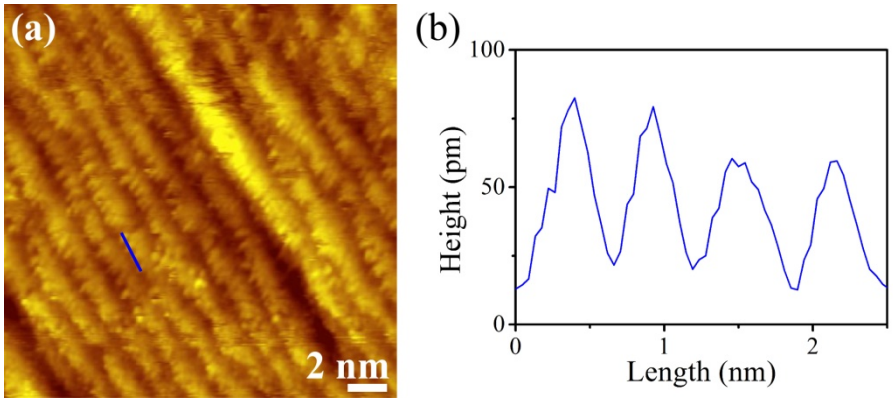

Figure 4-2. (a) STM image of Pt(557) under 950 mTorr of O_2 and 10 mTorr of H_2 and (b) topography profile of the blue line in (a) Periodic structures appear at a small part of the surface, and the topography profile of the blue line shows a periodicity of ~580 pm.

The Pt(557) surface structure under pure H_2 was investigated as a reference for understanding the structural changes in Figure 4-1. STM images reveal that the stepped structure is preserved when Pt(557) was exposed to 100 mTorr of H_2 at 298 K (Figure 4-3a). The average terrace width is 1.4 nm, the same value as the terrace width of clean Pt(557) in

UHV. Interestingly, step edges are frizzy under 100 mTorr of H_2, which indicates an enhanced mobility of the Pt step atoms, probably by virtue of the attachment of hydrogen atoms. No changes in the stepped structure are observed when the H_2 pressure was increased to 1 Torr (Figure 4-3b). Only an increase in the noise level is observed, probably as a consequence of enhanced surface mobility. Therefore, unlike CO and O_2, H_2 does not induce cluster formation or step coalescence on Pt(557).

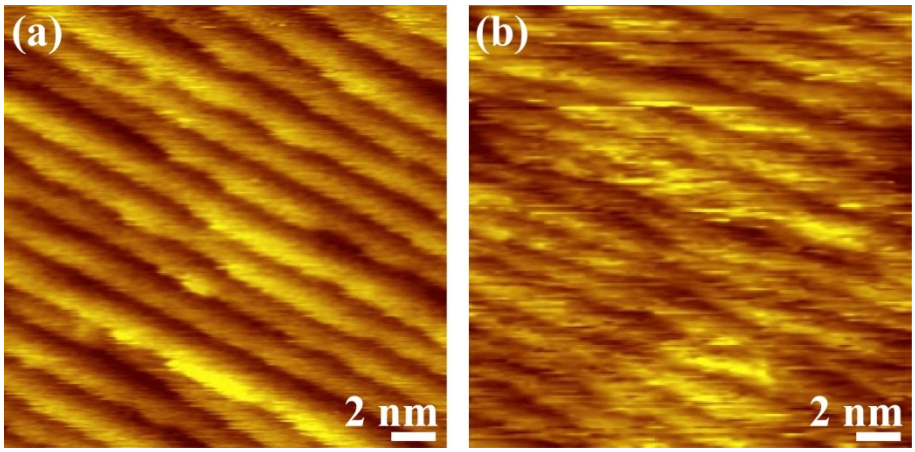

Figure 4-3. STM image of Pt(557) under (a) 100 mTorr and (b) 1 Torr of H_2. The stepped structure still retains with an average terrace width of 1.4 nm. Pt steps are much frizzier in (b) comparing to steps in (a), as a result of increased step and kink atom mobility.

In situ XPS experiments were performed under similar gas environments as in the HP-STM measurements, in order to examine the chemical state on Pt(557) during the structural evolution. Pt 4f and O 1s core level spectra were recorded at X-ray photon energies of 340 and 810 eV, which generate photoelectrons with kinetic energies of 270~280 eV and thus ensure a similar probing depth of ~0.6 nm for both elements.[28] Binding energies were calibrated with respect to the Fermi edge fixed at 0 eV in the valence band region acquired under the same conditions. The O 1s spectra are displayed in Figure 4-4 with the intensities normalized to the Pt 4f peak intensities under identical conditions. The gas-phase O_2 doublet peak (not shown) is located at 538.4 and 539.5 eV. A wide peak appears at ~530.5 eV after filling the chamber with 940 mTorr of O_2. This peak, with full width at half-maximum (fwhm) of 2.5 eV, is mainly due to the Pt oxide clusters covering the Pt(557) surface. Two other surface components may also contribute to the peak: chemisorbed oxygen that gives rise to a peak at 529.9 eV,[6] and OH groups formed by reactions with H_2 in the vacuum background gas, which produces peaks around 531 eV.[27,29,30] After the introduction of H_2, a new peak at 534.9 eV due to gas-phase water[31-33] appears and grows with H_2 partial pressures, indicating that water is the product.

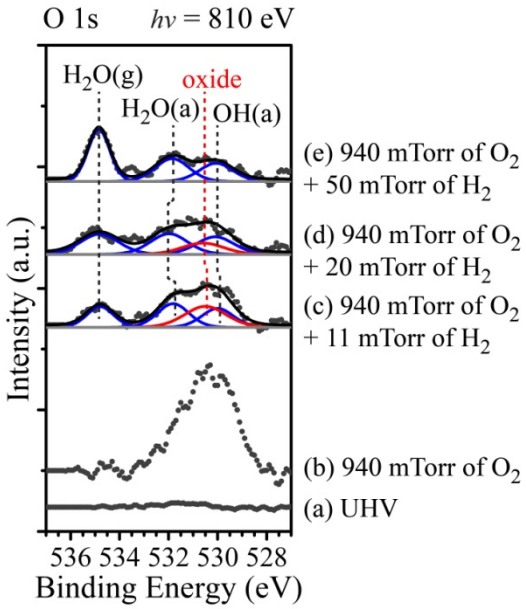

Figure 4-4. O 1s spectra of Pt(557) acquired with an incident X-ray photon energy of 810 eV (a) in UHV, (b) under 940 mTorr of O_2, and after addition of H_2 at partial pressures of (c) 11, (d) 20, and (e) 50 mTorr. The gas-phase O_2 1s peak characterized by a doublet at 538.4 and 539.5 eV is outside the range of the figure. The deconvoluted spectra illustrate how the introduction of H_2 results in the progressive decrease and the final disappearance of surface Pt oxide (red). Water is formed in the gas phase upon the introduction of H_2.

Meanwhile, the intensity of the initial surface Pt oxide peak greatly decreases with the addition of H_2, concomitant with the decrease in oxide cluster coverage in STM images. Significant changes in the O 1s peak shape are also observed, indicative of the formation of various oxygen-related species. In order to analyze the surface chemical states, the O 1s spectra in Figure 4-4c-e recorded under the H_2-O_2 mixture were deconvoluted using the gas-phase water peak and three surface components. The surface components include the Pt oxide peak at ~530.5 eV as in Figure 4-4b, chemisorbed H_2O peak at ~531.9 eV, and chemisorbed OH peak at ~530.1 eV. The assignment of chemisorbed H_2O and OH peaks agrees with literature values[27,30] and a recent study by Nilsson *et al.*,[34] where O 1s binding energies of chemisorbed H_2O and OH are 531.7 and 530.3 eV when they bond to each other. When the H_2 partial pressure reaches 50 mTorr (Figure 4-4e), the H_2O and OH peaks are sufficient for a good fit. The absence of the surface Pt oxide component agrees with STM results that Pt oxide clusters are removed at H_2 partial pressures above 43 mTorr. In addition, under our conditions of water and H_2 gas phase in the mTorr range, little chemisorbed oxygen can be present at the Pt(557) surface, since adsorbed H_2O molecules readily react with chemisorbed oxygen atoms to form OH species through reactions (3) and (4), which are fast enough to proceed at ambient temperatures.[20]

Under a H_2 partial pressure of 11 to 20 mTorr (Figure 4-4c,d), the surface Pt oxide component at 530.5 eV needs to be included in the deconvolution of O 1s spectra for a good fit. Because O 1s peaks of Pt oxide and OH groups are separated by only 0.4 eV, their relative intensity ratio can largely vary with slight changes in fitting parameters. To remedy this problem, the ratio of chemisorbed H_2O to OH peak areas was constrained to a fixed value—the ratio in the spectrum under 940 mTorr of O_2 and 50 mTorr H_2, when Pt oxide is absent. The deconvolution results show that the surface Pt oxide peak, marked by red curves, declines and ultimately disappears with the addition of H_2, along with the growth of the gas-phase water peak. In contrast, the peaks of chemisorbed H_2O and OH retain their intensities. Hydrogen atoms, which cannot be detected by STM or XPS in our experiments, are also likely to chemisorb on the Pt(557) surface during the reaction. Diffusion of hydrogen into subsurface sites, which typically happens on Pd surfaces,[35] cannot happen since the energy barrier for hydrogen atoms to diffuse into the subsurface is 0.66 and 0.99 eV on Pt(111) and Pt(100), respectively.[36,37] Such high activation energies should strongly inhibit hydrogen diffusion into the subsurface at 298 K.

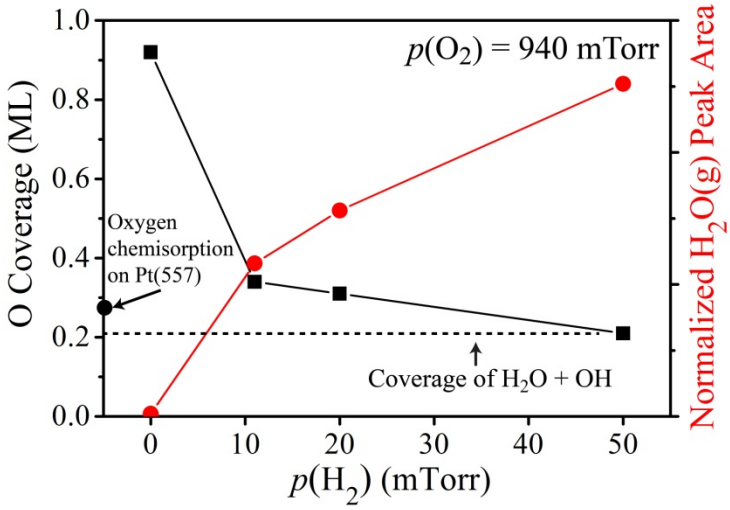

Figure 4-5. Changes in total oxygen coverage on Pt(557) (black squares) and normalized water gas peak area (red circles) with H_2 partial pressures when keeping the O_2 partial pressure at 940 mTorr. Reactions between Pt oxide and H_2 are responsible for the initial rapid decrease in the oxygen coverage and the initial increase in the normalized gas-phase water peak area. The total coverage of chemisorbed H_2O and OH remains constant at ~0.21 ML above 11 mTorr of H_2.

The total amount of surface oxygen, i.e. the oxygen coverage, can be estimated from the ratio of integrated areas of all surface O 1s peaks to Pt 4f peaks. Peak areas from 0.25 ML oxygen on Pt(111) at 10^{-7} Torr are used to calibrate the coverage.[38,39] Figure 4-5 shows that,

as the H_2 partial pressure increases, the oxygen coverage decreases rapidly and the amount of water in the gas phase increases rapidly while oxide is present at the surface. Starting at 0.92 ML on the oxide-covered surface under 940 mTorr of O_2, the oxygen coverage sharply drops to 0.34 ML after 11 mTorr of H_2 is introduced, accompanied by a sharp increase in the area of the gas-phase water peak. The oxygen coverage drops to 0.31 ML after raising the H_2 partial pressure to 20 mTorr, and further to 0.21 ML after adding 50 mTorr of H_2 which completely removes all the surface Pt oxide. Along with a moderate decline in oxygen coverage, the growth of the water gas peak also becomes slower. In addition, the total coverage of chemisorbed H_2O and OH stays at ~0.21 ML under all three H_2 partial pressures, indicating that the removal of Pt oxide is exclusively responsible for the drop in oxygen coverage by reaction with H_2.

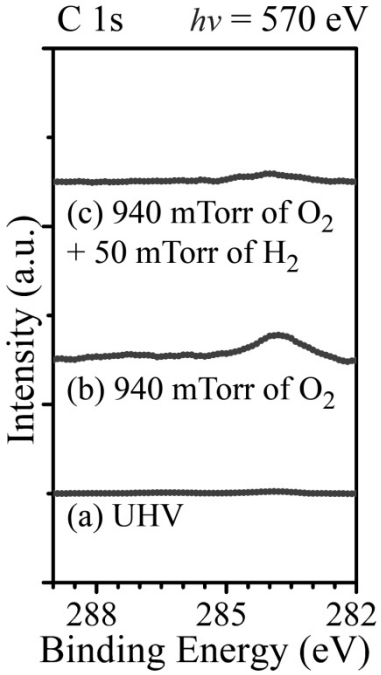

Figure 4-6. C 1s spectra of Pt(557) (a) in UHV, (b) under 940 mTorr of O_2, and (c) after adding 50 mTorr of H_2 into 940 mTorr of O_2. The surface is initially free of carbon contaminants in UHV. A small peak appears at 284 eV after introducing O_2, which represents hydrocarbon species. The C 1s peak significantly decreases in intensity with the introduction of H_2.

Carbon contamination is always a concern in surface science studies, as the presence of carbon-related species may block the adsorption of reactants by occupying certain surface sites. Carbon contamination typically arises from CO and hydrocarbon molecules in the vacuum background gases and on chamber walls. Figure 4-6 shows the C 1s spectra recorded during the hydrogen oxidation experiments. The Pt(557) surface is free of any

carbon contaminants in UHV, but a small peak at 284 eV grows with the introduction of 940 mTorr of O_2. By using 0.50 ML CO on Pt(557) at 5×10^{-9} Torr as the calibration,[3] the carbon coverage is less than 0.03 ML in Figure 4-6b. This C 1s peak nearly disappears after adding 50 mTorr of H_2. Local heat from the occurrence of hydrogen oxidation reaction may activate the oxidation of carbon contaminants by O_2. The carbon coverage is below 0.01 ML under the H_2-O_2 mixture. Surface contamination by carbon therefore can be negligible because of the low coverage while studying the Pt(557) surface structure in hydrogen oxidation.

4.3.2 H_2O Adsorption on Pt(557)

A control experiment regarding H_2O adsorption on Pt(557) was performed at the AP-XPS workstation, in order to verify that H_2O can chemisorb on Pt(557) at 298 K. The recorded O 1s spectra are displayed in Figure 4-7. Figure 4-7a shows that H_2O is indeed able to adsorb on Pt(557) even at low pressures such as 10^{-7} Torr, giving rise to two peaks at 532.8 and 531.0 eV, corresponding to chemisorbed H_2O and OH gropus.[27,30] The positions of these two peaks deviate from the same components in Figure 4-4, because the chemical environment is different owing to the absence of hydrogen. The coverage of H_2O and OH is 0.18 ML, close to the constant coverage of ~0.21 ML during the catalytic reaction.

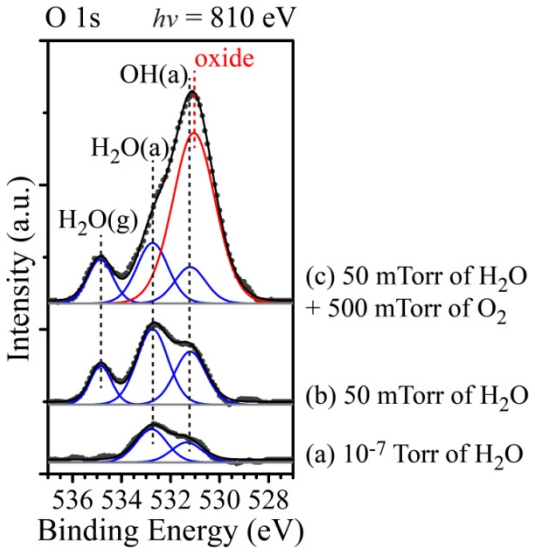

Figure 4-7. O 1s spectra of Pt(557) under (a) 10^{-7} Torr and (b) 50 mTorr of water, and (c) after adding 500 mTorr of O_2 into 50 mTorr of water. Water chemisorbs on Pt(557) at room temperature. With a subsequent dosage of 500 mTorr of O_2, Pt oxide can still form on the Pt(557) surface that is pre-covered by water.

When the H_2O pressure is raised to 50 mTorr, the gas-phase water peak appears at 534.9 eV, as in Figure 4-7b. The chemisorbed H_2O and OH peaks do not shift in binding energy,

and the relative area ratio of H_2O to OH peak remains the same. In addition, the total coverage of H_2O and OH increases to 0.42 ML. 500 mTorr of O_2 was subsequently introduced to study whether the adsorption of H_2O blocks the formation of Pt oxide. Figure 4-7c shows that a strong peak, which is highlighted in red, exists at 530.6 eV if fixing the position and relative intensity of H_2O and OH peaks. This peak is located at the same position as the surface Pt oxide component formed under pure O_2, implying that the Pt oxide can still form on the Pt(557) surface pre-covered by water.

4.3.3 CO Oxidation in the CO-O_2 Mixture

Figure 4-8 shows the structure of the Pt(557) surface under the mixture of 1 Torr of O_2 and 1 Torr of CO. CO was introduced into the high-pressure STM cell after resolving the Pt oxide clusters under O_2. After the addition of CO, Pt oxide clusters have disappeared all across the Pt(557) surface. The Pt(557) surface structure is dominated by CO under the CO-O_2 mixture, since the triangular Pt clusters of ~2 nm in size can be observed on most of the surfaces, as in Figure 4-8a. On the other parts where Pt clusters are not observed, wavy steps are resolved, as in Figure 4-8b. The average terrace width in Figure 4-8b is 2.4 nm, indicating that the terrace widths and step heights are both doubled, which is undoubtedly induced by CO, since it was illustrated in the previous chapter that O_2 does not cause step coalescence on Pt(557) at 298 K.

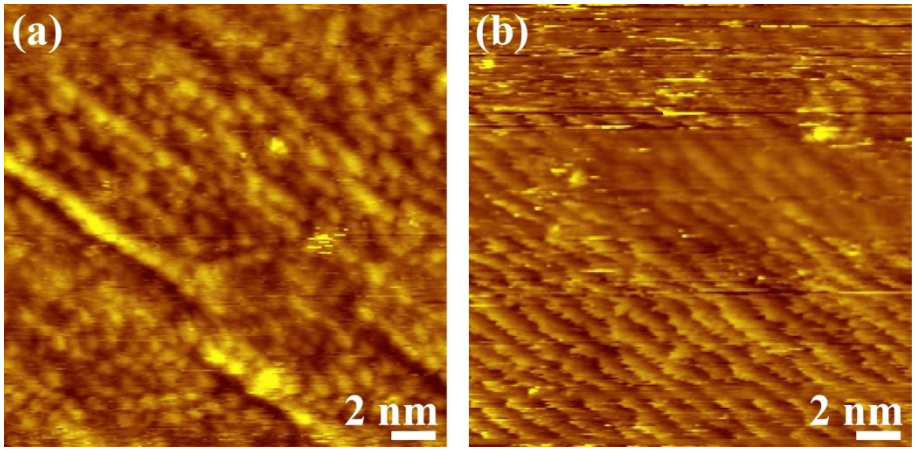

Figure 4-8. STM images of Pt(557) under the mixture of 1 Torr of O_2 and 1 Torr of CO. CO was introduced after the Pt oxide clusters were formed under O_2. Both (a) triangular Pt clusters and (b) doubling of terraces and steps are observed on different areas of the crystal surface. No Pt oxide clusters were present after the addition of CO.

The blurred clusters in Figure 4-8a and the noise in Figure 4-8b suggest the low image quality under the mixture of CO and O_2. The low quality is due to the poor performance of STM tips, since the tip selection is the biggest challenge when studying the surface

structure under the CO-O_2 mixture. Traditional electrochemically etched tungsten tips immediately lose the conductivity while exposing to O_2, because tungsten is promptly oxidized to form a thick insulating tungsten oxide layer. On the other hand, the $Pt_{0.8}Ir_{0.2}$ tips, although stable under O_2, restructures readily under CO, since the tip surface is much rougher than the Pt crystal sample. The fast restructuring process on the tip hence inhibits acquisition of high quality STM data, as the tip structure must have changed many times during 5 min that is required to record an STM image. Even the Au-coated $Pt_{0.8}Ir_{0.2}$ tips, which perform quite well under CO and its mixture with C_2H_4 (Chapter 5), are not stable enough under the CO oxidation mixture. Structural evolution on Pt(557) while varying the CO:O_2 pressure ratio was consequently not investigated.

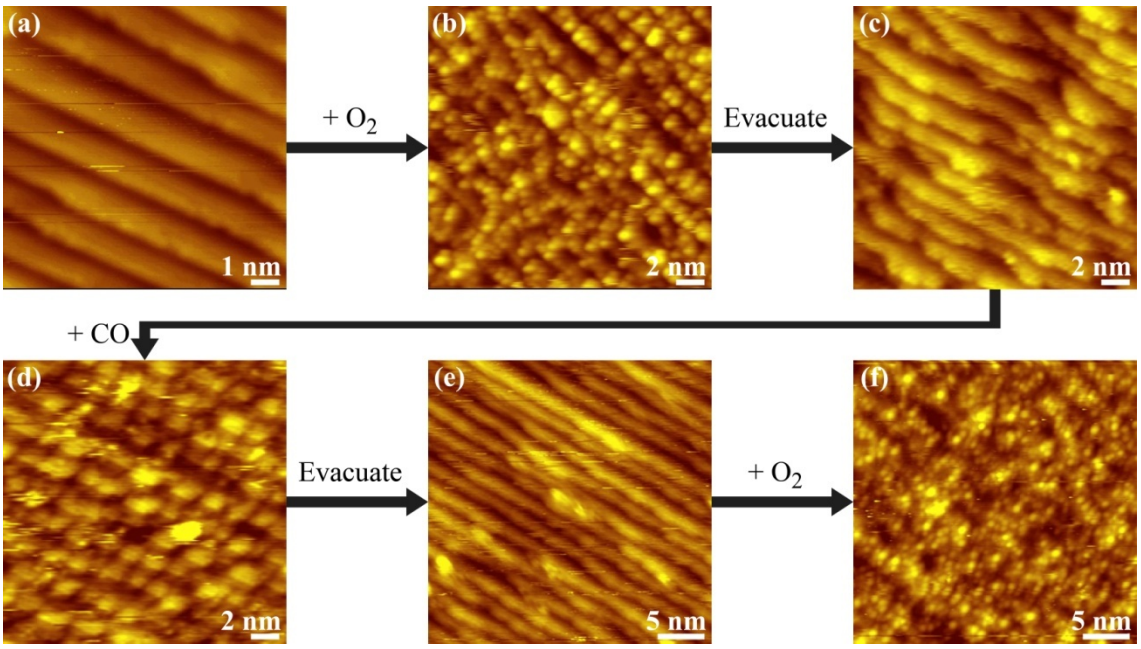

Figure 4-9. STM images of the Pt(557) surface while switching the gas between O_2 and CO. (a) The steps are initially clean in UHV. (b) Under 1 Torr of O_2, Pt oxide clusters appear roughly along the step edges. (c) Most of the Pt oxide clusters disappear upon evacuating O_2. (d) After introducing 1 Torr of CO, Pt clusters of ~2 nm in diameter are observed. (e) The CO-induced Pt clusters disappear and the stepped structure is restored with the evacuation of CO, and (f) Pt oxide clusters are formed again with the introduction of 1 Torr of O_2. The Pt(557) surface structure could vary reversibly between O_2 and CO.

The Pt(557) surface structure was studied while switching the gas between O_2 and CO instead. Figure 4-9 shows a series of STM images acquired in an O_2-CO-O_2 cycle. Starting in UHV with straight steps and clean terraces (Figure 4-9a), the Pt(557) surface is covered by nanometer-sized Pt oxide clusters roughly aligned along the original step

directions (Figure 4-9b). These clusters almost disappear with the evacuation of O_2 to 10^{-8} Torr, as in Figure 4-9c, which was discussed in the previous chapter. After adding 1 Torr of CO into the high-pressure STM cell, Pt steps have broken into clusters that look similar to the clusters observed when introducing CO onto the clean Pt(557) surface, as in Figure 4-9d. Since the chemisorbed oxygen atoms and some residual Pt oxide are present after evacuating O_2,[6] CO can undoubtedly react with all the surface oxygen species on Pt(557) at 298 K, in agreement with results on other Pt surfaces.[7,18]

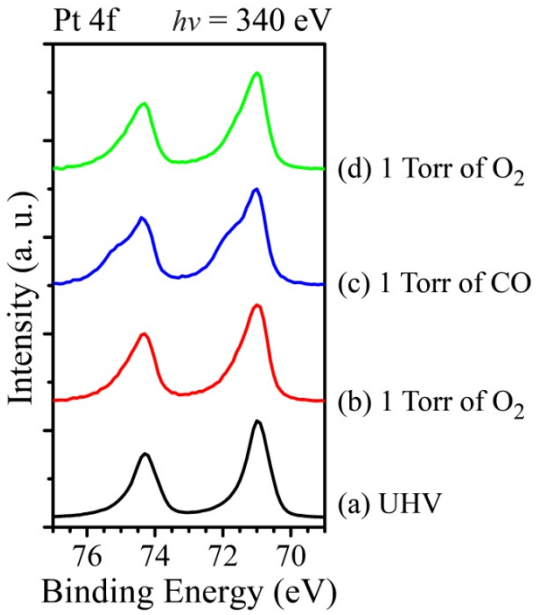

Figure 4-10. Pt 4f spectra of the Pt(557) surface acquired with incident energy of 340 eV (a) in UHV, (b) under 1 Torr of O_2, (c) after evacuating O_2 and introducing 1 Torr of CO, and (d) after evacuating CO and introducing 1 Torr of O_2. The Pt 4f spectra change reversibly with the gas environments as well, in agreement with STM results.

Figure 4-9e shows that, with the evacuation of CO to 10^{-8} Torr, the Pt clusters vanish on Pt(557) and the Pt steps are restored. The disappearance of CO-induced clusters accords with the results previously published in our group,[3] as the CO coverage has decreased by one-third after evacuation. Accordingly, the repulsion between chemisorbed CO molecules is not high enough to maintain the kink sites and Pt clusters. Pt atoms diffuse back to fill in the step vacancies, leading to the relative straight steps that have lower energy according to theoretical calculations.[3] When 1 Torr of O_2 was subsequently introduced again, small Pt oxide clusters are formed, as shown in Figure 4-9f, indicating that all the adsorbed CO molecules are removed by O_2, probably through forming CO_2. The Pt oxide clusters show higher density in Figure 4-9f than in Figure 4-9b. In addition, the clusters now appear blurred, since the STM tip inevitably gets blunt after staying

under O_2 and CO for a few hours.

AP-XPS results have also demonstrated that the structure of the Pt(557) surface can vary reversibly while switching the gas conditions between O_2 and CO. Figure 4-10 shows the Pt 4f spectra acquired in an O_2-CO-O_2 cycle. The spectra after evacuating gases are not displayed for clarity. With the introduction of 1 Torr of O_2, the Pt 4f peaks become wider, accompanied by the appearance of a shoulder at 71.6 eV from the surface Pt oxide,[6] as discussed in the previous chapter. After evacuating O_2 and introducing 1 Torr of CO, a prominent high-binding energy component grows at 72.1 eV, in agreement with the low-coordinated Pt atoms at cluster edges bonded with CO molecules.[3] This feature corresponding to Pt atoms at cluster edges disappears with the evacuation of CO and the re-introduction of 1 Torr of O_2, whereas surface Pt oxide reappears at 71.6 eV.

4.4 Conclusions

In summary, the surface Pt oxide on Pt(557) formed under approximately 1 Torr of O_2 is highly reactive to H_2. The effects of the hydrogen oxidation reaction are visible by STM at a low H_2 partial pressure of 2 mTorr. When raising the H_2 partial pressure, the smaller amount of Pt oxide in STM images and the weaker oxide peak in O 1s spectra illustrate that the reaction proceeds via consumption of Pt oxide, whereas the amount of chemisorbed H_2O and OH species remains constant at ~0.21 ML. Ultimately, at H_2 partial pressures greater than 43 mTorr, the surface Pt oxide is fully removed. The surface Pt oxide can also be removed by CO under 2 Torr of 1:1 CO-O_2 mixture. Both HP-STM and AP-XPS have revealed the reversible structural changes of the Pt(557) surface while switching the gas environment between O_2 and CO.

4.5 References

(1) Besenbacher, F.; Thostrup, P.; Salmeron, M. *MRS Bull.* **2012**, *37*, 677-681.

(2) Vang, R. T.; Lægsgaard, E.; Besenbacher, F. *Phys. Chem. Chem. Phys.* **2007**, *9*, 3460-3469.

(3) Tao, F.; Dag, S.; Wang, L. W.; Liu, Z.; Butcher, D. R.; Bluhm, H.; Salmeron, M.; Somorjai, G. A. *Science* **2010**, *327*, 850-853.

(4) Hendriksen, B. L. M.; Frenken, J. W. M. *Phys. Rev. Lett.* **2002**, *89*, 046101.

(5) Österlund, L.; Rasmussen, P. B.; Thostrup, P.; Lægsgaard, E.; Stensgaard, I.; Besenbacher, F. *Phys. Rev. Lett.* **2001**, *86*, 460-463.

(6) Zhu, Z.; Tao, F.; Zheng, F.; Chang, R.; Li, Y.; Heinke, L.; Liu, Z.; Salmeron, M.; Somorjai, G. A. *Nano Lett.* **2012**, *12*, 1491-1497.

(7) Butcher, D. R.; Grass, M. E.; Zeng, Z.; Aksoy, F.; Bluhm, H.; Li, W.-X.; Mun, B. S.; Somorjai, G. A.; Liu, Z. *J. Am. Chem. Soc.* **2011**, *133*, 20319.

(8) Merte, L. R.; Knudsen, J.; Eichhorn, F. M.; Porsgaard, S.; Zeuthen, H.; Grabow, L. C.; Lægsgaard, E.; Bluhm, H.; Salmeron, M.; Mavrikakis, M.; Besenbacher, F. *J. Am.*

Chem. Soc. **2011**, *133*, 10692-10695.

(9) Montano, M.; Bratlie, K. M.; Salmeron, M.; Somorjai, G. A. *J. Am. Chem. Soc.* **2006**, *128*, 13229-13234.

(10) Vestergaard, E. K.; Vang, R. T.; Knudsen, J.; Pedersen, T. M.; An, T.; Lægsgaard, E.; Stensgaard, I.; Hammer, B.; Besenbacher, F. *Phys. Rev. Lett.* **2005**, *95*, 126101.

(11) Tang, D. C.; Hwang, K. S.; Salmeron, M.; Somorjai, G. A. *J. Phys. Chem. B* **2004**, *108*, 13300-13306.

(12) Salmeron, M.; Schlögl, R. *Surf. Sci. Rep.* **2008**, *63*, 169-199.

(13) Starr, D. E.; Liu, Z.; Havecker, M.; Knop-Gericke, A.; Bluhm, H. *Chem. Soc. Rev.* **2013**, *42*, 5833-5857.

(14) Zhang, C.; Grass, M. E.; McDaniel, A. H.; DeCaluwe, S. C.; El Gabaly, F.; Liu, Z.; McCarty, K. F.; Farrow, R. L.; Linne, M. A.; Hussain, Z.; Jackson, G. S.; Bluhm, H.; Eichhorn, B. W. *Nat. Mater.* **2010**, *9*, 944-949.

(15) Grass, M. E.; Zhang, Y.; Butcher, D. R.; Park, J. Y.; Li, Y.; Bluhm, H.; Bratlie, K. M.; Zhang, T.; Somorjai, G. A. *Angew. Chem., Int. Ed.* **2008**, *47*, 8893-8896.

(16) Tao, F.; Grass, M. E.; Zhang, Y.; Butcher, D. R.; Renzas, J. R.; Liu, Z.; Chung, J. Y.; Mun, B. S.; Salmeron, M.; Somorjai, G. A. *Science* **2008**, *322*, 932-934.

(17) Tao, F.; Grass, M. E.; Zhang, Y.; Butcher, D. R.; Aksoy, F.; Aloni, S.; Altoe, V.; Alayoglu, S.; Renzas, J. R.; Tsung, C. K.; Zhu, Z.; Liu, Z.; Salmeron, M.; Somorjai, G. A. *J. Am. Chem. Soc.* **2010**, *132*, 8697-8703.

(18) Wang, J. G.; Li, W. X.; Borg, M.; Gustafson, J.; Mikkelsen, A.; Pedersen, T. M.; Lundgren, E.; Weissenrieder, J.; Klikovits, J.; Schmid, M.; Hammer, B.; Andersen, J. N. *Phys. Rev. Lett.* **2005**, *95*, 256102.

(19) Bedürftig, K.; Völkening, S.; Wang, Y.; Wintterlin, J.; Jacobi, K.; Ertl, G. *J. Chem. Phys.* **1999**, *111*, 11147-11154.

(20) Michaelides, A.; Hu, P. *J. Am. Chem. Soc.* **2001**, *123*, 4235-4242.

(21) Völkening, S.; Bedürftig, K.; Jacobi, K.; Wintterlin, J.; Ertl, G. *Phys. Rev. Lett.* **1999**, *83*, 2672-2675.

(22) Tao, F.; Tang, D. C.; Salmeron, M.; Somorjai, G. A. *Rev. Sci. Instrum.* **2008**, *79*, 084101.

(23) Grass, M. E.; Karlsson, P. G.; Aksoy, F.; Lundqvist, M.; Wannberg, B.; Mun, B. S.; Hussain, Z.; Liu, Z. *Rev. Sci. Instrum.* **2010**, *81*, 053106.

(24) Finch, G. I.; Murison, C. A.; Stuart, N.; Thomson, G. P. *Proc. R. Soc. London, A* **1933**, *141*, 414-434.

(25) Gentry, S. J.; Firth, J. G.; Jones, A. *J. Chem. Soc., Faraday Trans.* **1974**, *70*, 600-604.

(26) L'vov, B. V.; Galwey, A. K. *J. Therm. Anal. Calorim.* **2013**, *112*, 815-822.

(27) Endo, O.; Nakamura, M.; Sumii, R.; Amemiya, K. *J. Phys. Chem. C* **2012**, *116*, 13980-13984.

(28) Powell, C. J.; Jablonski, A. *NIST Electron Inelastic Mean Free Path Database, version 1.2*; National Institute of Standards and Technology: Gaithersburg, MD, 2010.

(29) Norton, P. R. *J. Catal.* **1975**, *36*, 211-223.

(30) Schiros, T.; Näslund, L.-Å.; Andersson, K.; Gyllenpalm, J.; Karlberg, G. S.; Odelius, M.; Ogasawara, H.; Pettersson, L. G. M.; Nilsson, A. *J. Phys. Chem. C* **2007**, *111*, 15003-15012.

(31) Andersson, K.; Ketteler, G.; Bluhm, H.; Yamamoto, S.; Ogasawara, H.; Pettersson, L. G. M.; Salmeron, M.; Nilsson, A. *J. Am. Chem. Soc.* **2008**, *130*, 2793-2797.

(32) Yamamoto, S.; Andersson, K.; Bluhm, H.; Ketteler, G.; Starr, D. E.; Schiros, T.; Ogasawara, H.; Pettersson, L. G. M.; Salmeron, M.; Nilsson, A. *J. Phys. Chem. C* **2007**, *111*, 7848-7850.

(33) Yamamoto, S.; Kendelewicz, T.; Newberg, J. T.; Ketteler, G.; Starr, D. E.; Mysak, E. R.; Andersson, K. J.; Ogasawara, H.; Bluhm, H.; Salmeron, M.; Brown, G. E.; Nilsson, A. *J. Phys. Chem. C* **2010**, *114*, 2256-2266.

(34) Casalongue, H. S.; Kaya, S.; Nilsson, A.; Ogasawara, H., Private Communications.

(35) Schauermann, S.; Nilius, N.; Shaikhutdinov, S.; Freund, H.-J. *Acc. Chem. Res.* **2013**, *46*, 1673-1681.

(36) Ferrin, P.; Kandoi, S.; Nilekar, A. U.; Mavrikakis, M. *Surf. Sci.* **2012**, *606*, 679-689.

(37) Greeley, J.; Mavrikakis, M. *J. Phys. Chem. B* **2005**, *109*, 3460-3471.

(38) Materer, N.; Starke, U.; Barbieri, A.; Döll, R.; Heinz, K.; Van Hove, M. A.; Somorjai, G. A. *Surf. Sci.* **1995**, *325*, 207-222.

(39) Gland, J. L.; Sexton, B. A.; Fisher, G. B. *Surf. Sci.* **1980**, *95*, 587-602.

Chapter 5

Influence of Step Geometries on Pt Surface Reconstruction under Ethylene and Carbon Monoxide

(This chapter covers similar materials as Zhu, Z. *et al.* in preparation.)

Abstract

The structure of two stepped Pt crystal surfaces, Pt(332) and Pt(557), was studied under C_2H_4, CO, and their gas mixtures at pressures in the Torr range at 298 K by HP-STM and AP-XPS. Both techniques show that the two crystal surfaces respond differently to the exposure of gases. Pt clusters are observed on both crystals but in different shapes under 500 mTorr of CO. A subsequent introduction of 500 mTorr of C_2H_4 removes the clusters and restores the steps on Pt(332) as a result of ethylidyne adsorption at the (111) steps, whereas the CO-induced clusters remain on Pt(557) because the (100) steps are not proper for ethylidyne adsorption. While reversing the gas dosage sequence, periodic adsorption patterns due to ethylidyne are resolved at step edges on Pt(332) but not on Pt(557) under 500 mTorr of C_2H_4. Pt clusters are observed on neither surface after further adding 500 mTorr of CO. The step orientation thus plays a crucial role in influencing surface reconstruction at high gas pressures.

5.1 Introduction

The low-coordinated surface sites, for example atomic step and kink positions, often have higher heat of adsorption, lower adsorption barrier, and higher sticking probability than terrace atoms when binding with reactants.[1-7] In addition, chemical bonds in reactants are readily broken at step sites upon adsorption.[7-11] Although the strong chemisorption at step sites may sometimes inhibit the occurrence of reactions,[12] these low-coordinated sites are usually viewed as the real active sites for heterogeneous catalysis.[1-3,8,9,13] Higher activity at step sites was indeed observed in a variety of solid−gas interface reactions such as hydrogen-deuterium exchange reaction,[14-16] CO oxidation,[13,17] metal oxide formation,[18,19] and ammonia synthesis.[20,21] Reactions occurring at the solid−liquid interface and electrochemical reactions also proceed rapidly at step sites.[22-24]

In addition to enhancing catalytic performances, low-coordinated sites promote drastic restructuring processes of the catalyst surfaces in response to adsorbed reactant molecules.[19,25-28] High concentration of step sites can be controllably produced using stepped surfaces with high Miller-indices, which are thus ideal model systems to resemble real catalysts for investigation of surface reconstruction. Two step orientations with (111) and (100) microfacets are present near (111) terraces of fcc crystal structures. These two steps are hence denoted as (111) and (100) steps. Since step orientations are critical in influencing binding sites, bond strengths, and diffusion and activation barriers that are important in heterogeneous catalysis, distinct catalytic behaviors and reconstruction phenomena can be observed at different step sites. For instance, 1D Rh oxide is continuous at (100) Rh steps but defective at (111) Rh steps.[29] The growth of 1D Rh oxide into a 2D oxide layer is hindered at (100) steps but fast at (111) steps below 523 K, because the defect-free 1D oxide increases the oxygen diffusion barrier.

Structural changes due to co-adsorption of two or more gases have called considerable attention in surface science studies, because most reactions involve two or more reactant species present at catalyst surfaces. In addition, the structure affected by the competition between reactants and poisonous species is also critical in heterogeneous catalysis. The co-adsorption of CO and C_2H_4 on Pt, an important co-adsorption system, has been studied at elevated pressures on both low Miller-index surfaces and supported catalysts.[30-33] The Pt surface structure has been shown to be strongly influenced by CO and C_2H_4 adsorption and by their competition during co-adsorption, depending on the sequence of gas dosage. On Pt surfaces pre-covered by CO, the sites for irreversible ethylene adsorption are almost all blocked. However, when ethylene was introduced first, CO is able to displace π-bonded ethylene and di-σ-bonded ethylene because the open and mobile ethylidyne adsorption unit cell also accommodates CO molecules.

Despite a number of studies about CO and C_2H_4 co-adsorption on Pt surfaces with vibrational techniques and temperature programmed desorption, the Pt surface structure is not well understood at the molecular level. On the Pt(111) surface, CO and ethylidyne form

a hexagonal pattern, with CO occupying the top and bridge sites and ethylidyne residing on three-fold hollow sites.[34] This chapter explores the reconstruction of two stepped Pt surfaces, Pt(332) and Pt(557) by HP-STM and AP-XPS in the presence of C_2H_4, CO, and their gas mixtures in the Torr range. Step orientations play a crucial role in determining surface reconstruction at high gas pressures. CO creates clusters in different shapes on the two surfaces at 500 mTorr. 500 mTorr of C_2H_4 results in periodic pattern at the step edges on Pt(332) but not on Pt(557). Most importantly, C_2H_4 post-adsorption removes the clusters on Pt(332) formed under pure CO, whereas Pt clusters on Pt(557) remain upon introducing ethylene. CO post-adsorption, however, does not change the structures induced by ethylene, although AP-XPS reveals nearly half monolayer of CO on both Pt surfaces.

5.2 Experimental Section

STM experiments were conducted in a transportable home-built system consisting of an STM chamber and a preparation chamber that are separated by a gate valve.[35] Both chambers are kept under base pressures of 10^{-10} Torr. Before STM measurements, the Pt crystals were prepared via cycles of ion bombardment and annealing. A typical cycle involves Ar^+ bombardment at 3×10^{-5} Torr at 1000 eV, O_2 annealing at 5×10^{-8} Torr at 923 K and a final flashing to 1073 K in UHV. After the last flashing step in UHV, crystals were cooled down to 298 K with a cooling rate of 1 K/sec. The preparation cycles were repeated until no carbon and oxygen contaminants were detected at surface by AES at 298 K. Commercial $Pt_{0.8}Ir_{0.2}$ tips with a 50-nm thick Au-coating layer were used to record all the STM images at 298 K. All the STM images were recorded with a sample bias of +0.2 V and a tunneling current of 0.1 nA.

AP-XPS experiments were performed at Beamline 9.3.2 at ALS in LBNL.[36] The apparatus also comprises two UHV chambers—one for XPS measurements and the other for sample preparation. The base pressures of the two chambers are in the 10^{-9} Torr range. Pt crystals were cleaned by following the identical procedures to those in the STM experiments. Pt surfaces were analyzed with XPS survey spectra to ensure the absence of any contaminants before gas introduction.

Pt 4f, C 1s and O 1s core level spectra were obtained at 298 K at X-ray photon energies of 340 eV, 570 eV and 810 eV, respectively. Kinetic energies of photoelectrons were therefore 270~280 eV for all three elements, which ensured the same probing depth of ~0.6 nm.[37] Valence band spectra were acquired together with the core level spectra for energy calibration, by setting the Fermi edge in the valence band spectra at 0 eV. The intensity of C 1s and O 1s spectra was normalized to Pt 4f spectra taken together under each condition. Shirley-type background was subtracted from each spectrum before peak deconvolution and area integration. CO coverage was calibrated relative to 0.50 ML on both Pt crystals at 298 K,[25] and the coverage of C_2H_4 was estimated by assuming the same atomic sensitivity of carbon atoms in CO and C_2H_4, i.e. the C 1s peak area of 0.01 ML C_2H_4 is twice as the

peak area of 0.01 ML CO.

5.3 Results and Discussion

5.3.1 Clean Surfaces

Figure 5-1 shows the STM images of clean Pt(332) and Pt(557) surfaces in UHV along with the corresponding ball models. The two surfaces were both cut at an angle 10˚ off the (111) plane but along opposite directions, with miscut angles below 0.1˚. Both surfaces have six-atom wide hexagonally close-packed (111) terraces, whereas the monatomic steps are oriented along (111) and (100) directions on Pt(332) and Pt(557), respectively. Pt steps on the clean surfaces appear straight in the STM images. The average terrace widths are 1.4 nm on both surfaces, which accords with the calculated values based on the Pt atomic radius of 139 pm.[38]

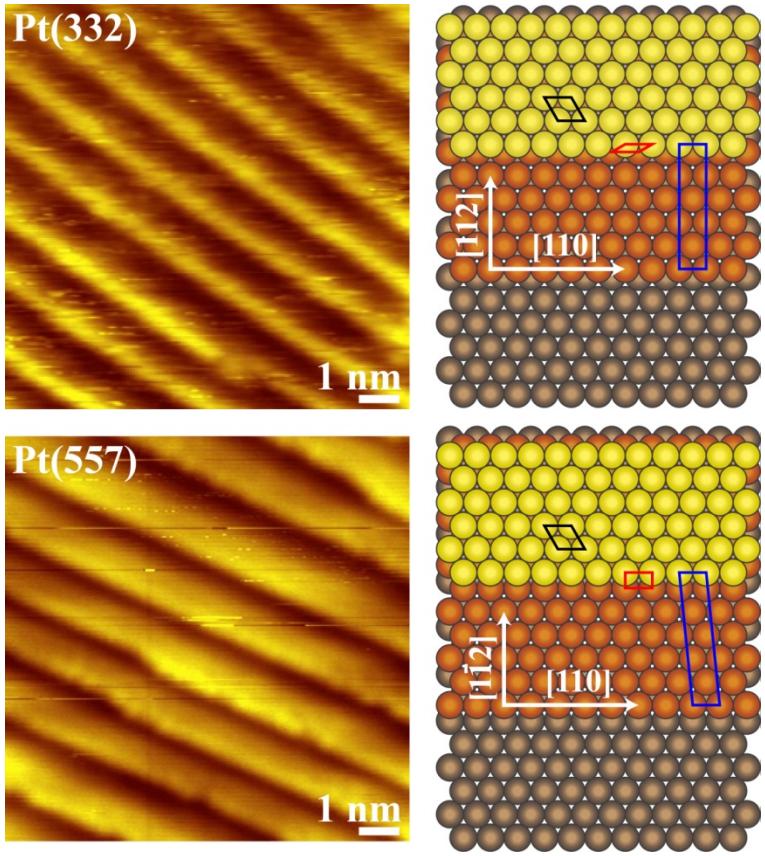

Figure 5-1. (left) STM images and (right) the ball models of (top) Pt(332) and (bottom) Pt(557) surfaces. The STM images were acquired in UHV with a base pressure of 10^{-10} Torr. Black, red, and blue parallelograms in the ball models mark the unit cell of terraces, steps, and the surfaces, respectively.

5.3.2 Ethylene Adsorption on Pt Surfaces Pre-Covered by CO

Effect of step orientation on Pt surface reconstruction was first studied by introducing 500 mTorr of CO and subsequently 500 mTorr of C_2H_4. Figure 5-2a shows that part of the Pt steps on Pt(332) break into clusters in parallelograms after adding under 500 mTorr of pure CO, which agrees with our prior studies under similar CO pressures.[25] The rest of the steps without clusters are still straight on Pt(332), on which a periodic pattern can be roughly resolved, as shown in Figure 5-2b. The periodicity is measured as 570 pm from the line profile, close to twice as Pt−Pt distances. This structure is unlikely due to the c(4 × 2) pattern on Pt(111) terraces at 0.50 ML, because Moiré pattern is observed at high CO pressures.[39] Detailed structure of this adsorption pattern requires information on the terraces.

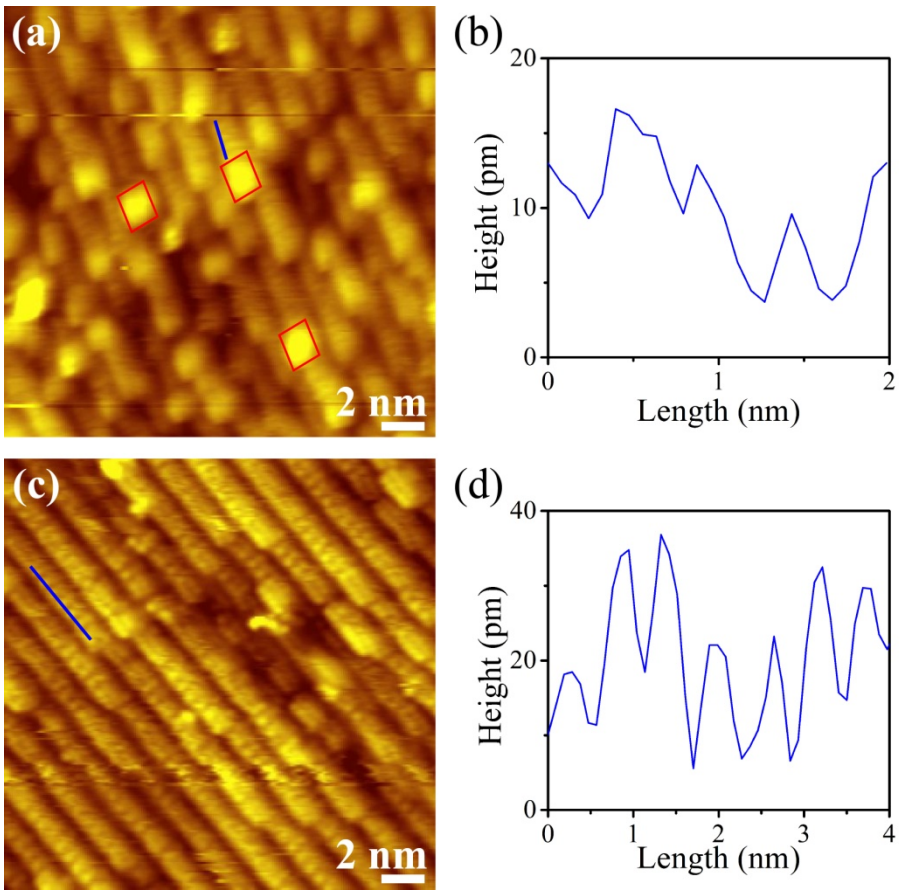

Figure 5-2. (a) STM image of Pt(332) under 500 mTorr of CO and (b) the line profile of the blue line in (a). Clusters in parallelograms are formed on Pt(332) under 500 mTorr of CO as highlighted in (a). CO adsorption is observed at the step edges where clusters are not formed. (c) STM image of Pt(332) after subsequently adding 500 mTorr of C_2H_4 into 500 mTorr of CO and (d) the topography profile of the line in (c). Pt clusters disappear on Pt(332) after introducing C_2H_4. Periodic adsorption pattern is resolved more clearly.

Upon further introducing 500 mTorr of C_2H_4, Figure 5-2c shows that over 80% of the Pt clusters on Pt(332) originally formed under CO disappear, which suggests that C_2H_4 is able to adsorb on the Pt(332) surface pre-covered by CO. The presence of three-fold sites at steps allows C_2H_4 adsorption on the CO-covered Pt(332) surface, as was revealed in our previous studies on supported Pt nanoparticles.[32] The periodic pattern with a periodicity of 570 pm is resolved more clearly at the step edges, with the topography profile displaying in Figure 5-2d. Although CO gives a c(4 × 2) pattern[39] on Pt(111) terraces and ethylidyne gives a (2 × 2) pattern[40] that both contain twice periodicity, these structures actually form at pressures in the 10^{-7} Torr range. At elevated pressures, the CO-C_2H_4 mixture induces a Moiré pattern on Pt(111) terraces similar to the pattern formed by CO alone.[34,39] However, the similar contrast in the periodic pattern in Figure 5-2d implies that Moiré pattern is not formed. The periodic structure at the step edges is tentatively ascribed to the adsorption of CO and ethylidyne together.

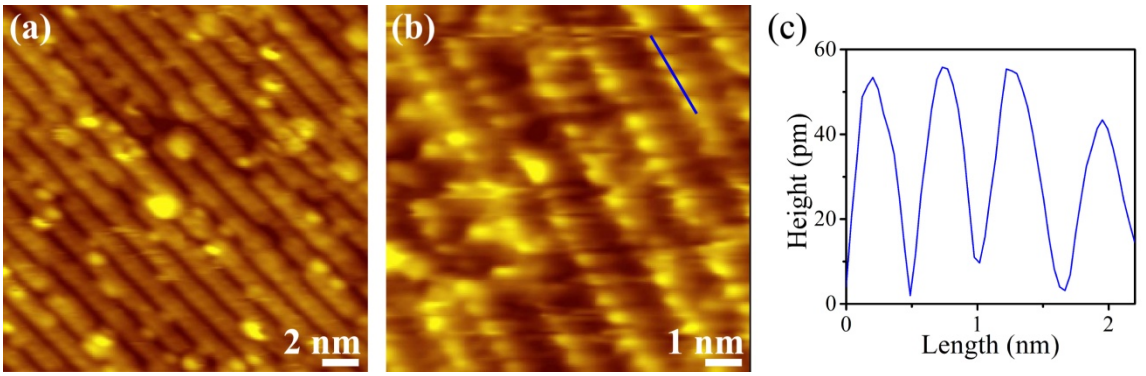

Figure 5-3. STM images of Pt(332) under 500 mTorr of CO and 2.5 Torr of C_2H_4 at (a) low and (b) high magnification. The CO-induced clusters all disappear at the step edges and some new bright features appear on the terraces. Zooming in at the step edges shows the periodic pattern at the step edges. (c) Topography profile of the blue line in (b) showing the periodicity of 570 pm.

The Pt(332) surface structure continues changing with the further increase of the C_2H_4 partial pressure. Figure 5-3a illustrates that, when 2.5 Torr of C_2H_4 is introduced, the CO-induced clusters completely vanish on Pt(332). New bright features with round shape and approximately 1 nm in size are observed at the step proximity on the upper terraces. Since the relative contrast between these features and Pt steps differs from the contrast between the clusters and Pt steps in Figure 5-2a, the bright spots are attributed to the weakly adsorbed ethylene-related species. Further vibrational spectroscopy measurements are under plan to identify the chemical composition of the surface species. The periodic structure is still seen when zooming in at the step edges, as in Figure 5-3b. Figure 5-3c

shows the topography profile of the blue line in Figure 5-3b with the periodicity remaining at 570 pm.

Structural changes on Pt(557) upon the same gas introduction process are different from the phenomena observed on Pt(332). As displayed in Figure 5-4a, Pt clusters are formed on all the Pt steps on Pt(557) when 500 mTorr of CO is initially dosed. No periodic adsorption pattern is resolved because Pt clusters are adjacent to each other, leaving no space between clusters. These clusters are triangular, different from the clusters on Pt(332) in shape, in consistence with our prior reports.[25] The average cluster size of 2 nm both along the steps and vertical to steps indicates that the cluster formation is preceded by a doubling transition of terrace widths and step heights. Figure 5-4b demonstrates that neither the removal of Pt clusters nor the appearance of periodic patterns at step edges after adding 500 mTorr of C_2H_4, probably because the four-fold sites at (100) steps are inappropriate for ethylidyne adsorption.

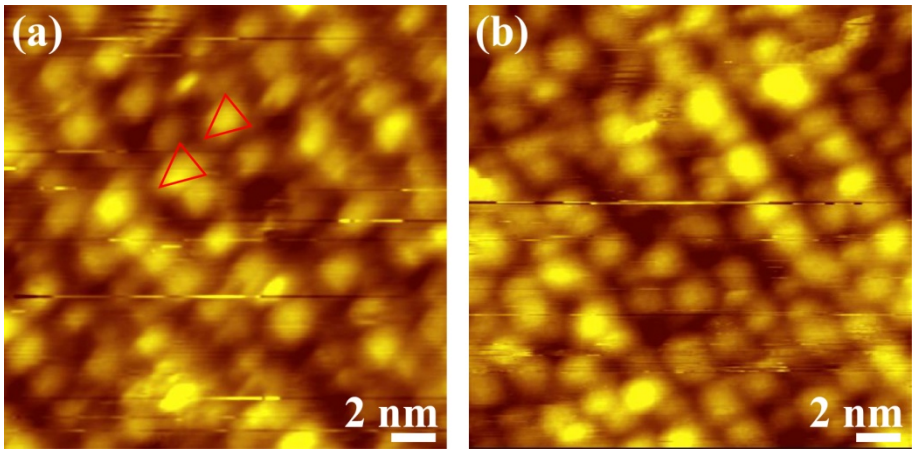

Figure 5-4. STM images of Pt(557) under (a) 500 mTorr of CO and (b) after subsequently adding 500 mTorr of C_2H_4. All the steps on Pt(557) break into triangular clusters of 2 nm in size on average under 500 mTorr of CO. These clusters remain on Pt(557) with the further introduction of 500 mTorr of C_2H_4.

Detailed analysis of the C 1s and O 1s spectra also reveals the different reconstruction on Pt(332) and Pt(557), as shown in Figure 5-5 and Figure 5-6. Under 500 mTorr of CO, C 1s and O 1s spectra can be both deconvoluted into three components corresponding to CO molecules in the gas phase, at top sites, and at bridge sites.[41,42] Hydrocarbon contamination from chamber background gases, usually at around 284 eV in C 1s spectra, is not observed. However, a higher proportion of CO molecules reside on top sites on Pt(332) than on Pt(557). The top-to-bridge CO ratio, estimated based on the deconvoluted O 1s peak areas, is 3.0 on the Pt(332) surface but 2.3 on the Pt(557) surface. The preference of CO on top sites on Pt(332) is due to the exclusive adsorption on top sites at (111) steps, in contrast

with the adsorption on both top and bridge sites at (100) steps.[43] In addition, the CO coverage is 0.88 ML on Pt(332) and 0.93 ML on Pt(557) at 500 mTorr. The higher CO coverage on Pt(557) under the same CO pressure leads to the stronger repulsion between adsorbed CO molecules. In order to remedy the repulsive interaction between CO, more Pt atoms on Pt(557) diffuse along the steps to form clusters having a higher concentration of low-coordinated kink sites, leading to the higher cluster coverage on Pt(557).

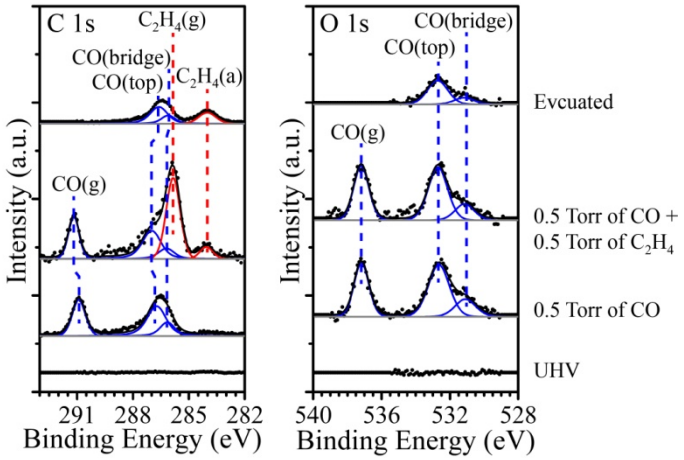

Figure 5-5. C 1s and O 1s spectra of Pt(332) recorded in UHV, under 500 mTorr of CO, after adding 500 mTorr of C_2H_4, and after gas evacuation. Blue lines denote CO-related species in the gas phase and at surface, and red lines represent ethylene-related species. C_2H_4 is able to chemisorb on the Pt(332) surface that is pre-covered by CO. The coverage of C_2H_4 retains on Pt(332) after gas evacuation, whereas CO partially desorbs.

After introducing C_2H_4, not only does a peak appear at ~286.0 eV in the C 1s spectra owing to the gas-phase C_2H_4, but a small feature also grows at ~284.1 eV as the evidence of ethylene-related adsorbates on stepped Pt surfaces. The adsorption of ethylene on stepped Pt surfaces pre-covered by CO is directly evidenced by AP-XPS measurements. The C_2H_4 coverage is estimated to be 0.08 and 0.05 ML on Pt(332) and Pt(557), with the CO coverage decreasing to 0.80 and 0.88 ML, respectively. One ethylene molecule seems to displace one CO molecule during co-adsorption, because the C_2H_4 coverage is equal to the CO coverage decrease. Since the (111) steps on Pt(332) provide extra three-fold sites for ethylidyne adsorption, Pt(332) accommodates more C_2H_4 than Pt(557). The increase in top-to-bridge CO ratio to 3.3 on Pt(332) indicates CO adsorption site exchanges caused by ethylene-related adsorbates. Ethylidyne molecules drive the Pt atoms at the cluster edges to move back to the step sites. In contrast, since the four-fold sites at (100) steps on Pt(557) do not admit ethylidyne adsorption, clusters remain and the top-to-bridge CO ratio retains at 2.3 on Pt(557) with the addition of C_2H_4.

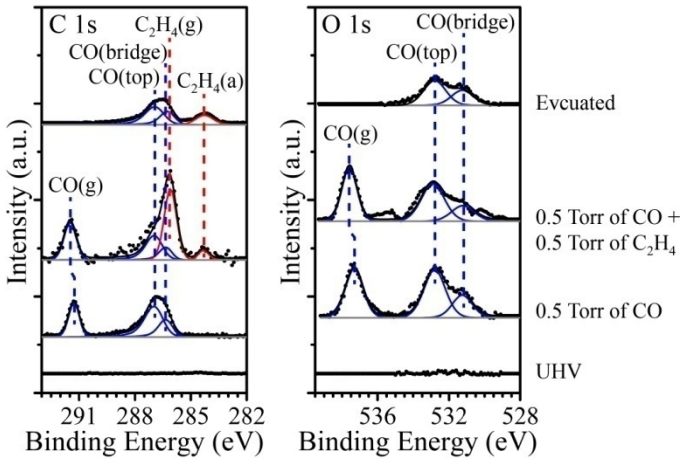

Figure 5-6. C 1s and O 1s spectra of Pt(557) under CO and C_2H_4. These spectra were taken in UHV, under 500 mTorr of CO, after adding 500 mTorr of C_2H_4, and after gas evacuation. Blue and red lines denote CO-related and ethylene-related species, respectively. The Pt(557) surface pre-covered by CO is able to accommodate C_2H_4 as well, although the ethylene-related adsorbate peak is less intense than that on Pt(332). Ethylene-related adsorbates remain upon gas evacuation, but part of the adsorbed CO desorbs.

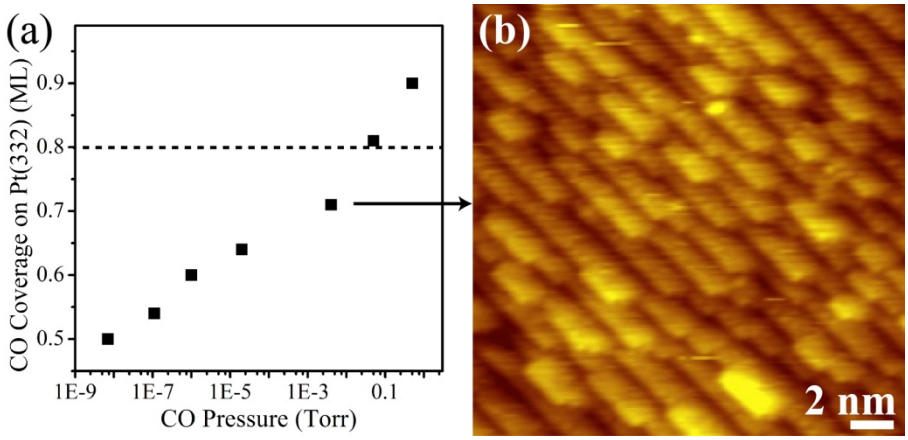

Figure 5-7. (a) Changes of CO coverage on Pt(332) with respect to CO pressures. The dash line marks 0.80 ML CO, the CO coverage on the cluster-free Pt(332) surface after adding 500 mTorr of C_2H_4 into 500 mTorr of CO. Approximately 50 mTorr of pure CO gives a coverage of 0.80 ML on Pt(332). (b) STM image of Pt(332) under 7 mTorr of CO (~0.73 ML), showing the formation of CO-induced clusters, which look similar to the clusters under 500 mTorr of CO. Pt clusters can be formed at a pure CO coverage below 0.80 ML.

However, the lower CO coverage on Pt(332) may provide an alternative explanation for

the disappearance of clusters that the critical CO coverage to induce clusters on Pt(332) is between 0.80 and 0.88 ML. From the trend of the CO coverage on Pt(332) with respect to the CO pressure in Figure 5-7a, a reference experiment was performed under 7 mTorr of pure CO which gives 0.73 ML CO on Pt(332). Figure 5-7b shows that Pt clusters can still form at this low CO coverage. It is hence undoubtedly the adsorption of ethylidyne at step sites that causes the Pt clusters to disappear on Pt(332). Ethylene-related adsorbates are present on both Pt surfaces after evacuating the XPS chamber to 10^{-8} Torr, which further verifies the adsorption of C_2H_4 the stepped Pt surfaces pre-covered by CO. The C_2H_4 coverage does not change on both surfaces, whereas the CO coverage decreases to 0.49 ML on Pt(332) and to 0.63 ML on Pt(557) owing to partial desorption.

5.3.3 CO Adsorption on Pt Surfaces Pre-Covered by Ethylene

Surface restructuring processes when introducing CO after C_2H_4 are distinct from the phenomena observed when adding CO prior to C_2H_4 on both Pt(332) and Pt(557) surfaces. Figure 5-8a shows that short periodic patterns are resolved at part of step edges on Pt(332) under 500 mTorr of C_2H_4. The line profile in Figure 5-8d shows the periodicity of 570 pm, which can correspond to C_2H_4 adsorption. C_2H_4 is likely to convert to ethylidyne after adsorption, since three-fold fcc hollow sites are present on (111)-oriented terraces and steps on Pt(332). Since ethylidyne forms a (2 × 1) pattern at 0.50 ML on Pt(111) terraces,[40] and in the sense that XPS analysis shown below estimates the C_2H_4 coverage to be 0.50 ML on Pt(332), the pattern is due to the ethylidyne adsorption. Whether ethylidyne resides on upper terraces or at steps is currently hardly determined, because the blunt STM tip due to the 50-nm thick Au layer is not able to image the structure on the narrow terrace of 1.4 nm in width. Although steps appear roughened in Figure 5-8a, it is the absence of ethylidyne at part of the steps that leads to distinct contrast in the image, which looks as if the kink sites are formed.

Figure 5-8b demonstrates that further adding 500 mTorr of CO does not lead to any obvious structural changes. CO-induced clusters are not observed even 4 h after the introduction of CO. Because ethylene-related adsorbates bond to a few Pt atoms, for instance, each ethylidyne molecule bonds to three Pt atoms, the Pt diffusion barrier can be significantly increased, because Pt−C bond breaking is needed prior to Pt atom diffusion. Additionally, the ethylene-saturated Pt(332) surface does not admit as much CO as the clean Pt(332) surface. The repulsion between CO molecules is thus not sufficiently strong to push Pt atoms to diffuse. Since the CO−CO repulsion is a major driving force for Pt diffusion and cluster formation,[25] CO-induced Pt clusters cannot form on the Pt(332) surface pre-covered by C_2H_4. The periodic structure observed under pure C_2H_4 is also clearly resolved after adding CO while zooming in at the steps, as in Figure 5-8c. Figure 5-8e displays that the periodicity remains at 570 pm. This periodic pattern is due to either the adsorption of ethylidyne alone or its co-adsorption with CO.

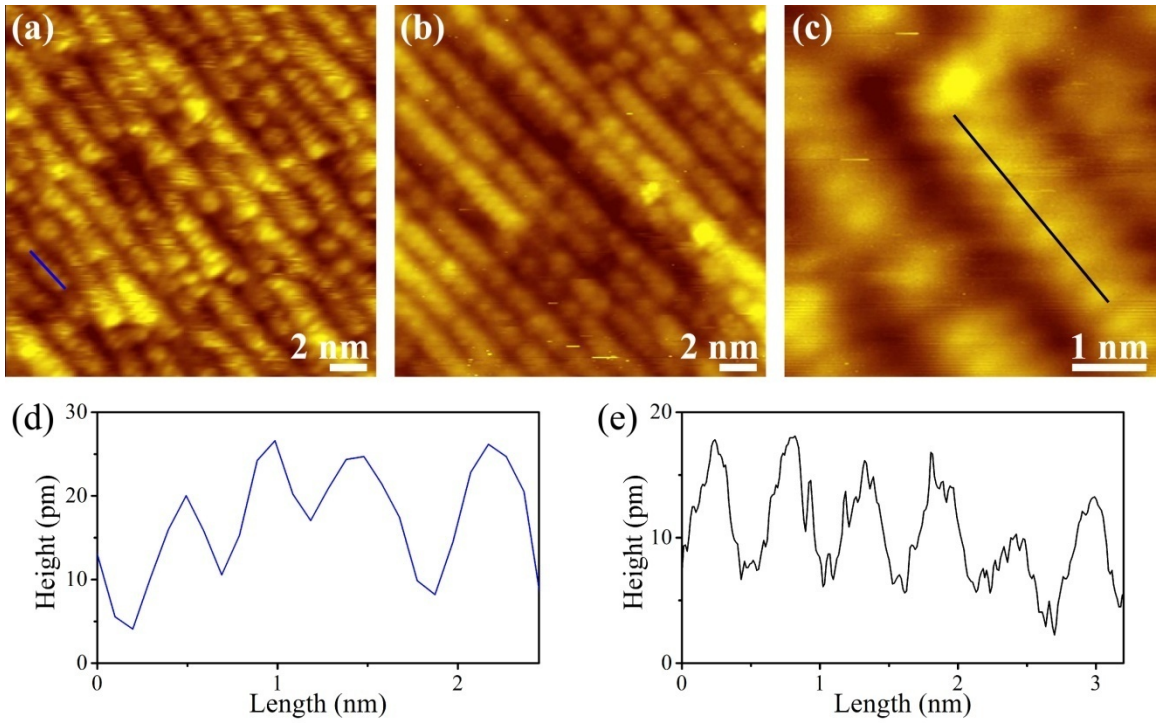

Figure 5-8. STM images and topography profiles of Pt(332) under C_2H_4 and its mixture with CO. (a) Short periodic patterns due to ethylidyne adsorption are observed at steps on Pt(332) under 500 mTorr of C_2H_4. (b,c) After subsequently introducing 500 mTorr of CO, no Pt clusters are formed. A periodic structure is clearly seen at the step edges in the high magnification STM image in (c). (d,e) Line profiles of the blue line in (a) and the black line in (c), respectively, showing the periodicity of 570 pm from ethylidyne adsorption and the co-adsorption with CO.

The reconstruction on Pt(557) during the same gas introduction process is shown in Figure 5-9. As in Figure 5-9a, no periodic structure is observed at step edges under 500 mTorr of C_2H_4, since ethylidyne cannot occupy the four-fold sites at (100) steps on Pt(557). Instead, a few separate bright spots of 800 pm in size, with the line profile in Figure 5-9c, are decorating the step edges. These spots are attributed to ethylene-related adsorbates at the (100) steps, possibly vinylidene. C_2H_4 is easier to adsorb at (111) steps on Pt(332), in accordance with methane adsorption results that C−H bonds are easier to break at (111) steps than at (100) steps.[44] When 500 mTorr of CO was subsequently added while keeping the C_2H_4 partial pressure at 500 mTorr, the surface structure does not change obviously with similar bright species also being observed at the step edges, as in Figure 5-9b. Although some steps do turn meandering upon adding CO, triangular clusters do not appear on Pt(557) regardless of the CO exposure time, similar to the results on Pt(332).

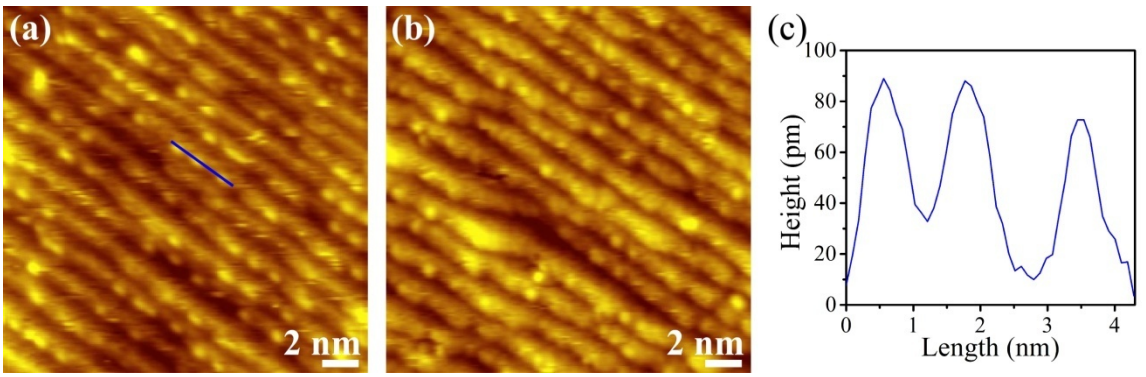

Figure 5-9. STM images of Pt(557) recorded (a) under 500 mTorr of C_2H_4 and (b) after subsequent addition of 500 mTorr of CO. A few bright spots instead of periodic patterns are resolved at the step edges. Further introducing CO does not lead to cluster formation on Pt(557). (c) Topography profile of the blue line in (a) showing that the bright spots at the step edges are separated by at least 1 nm.

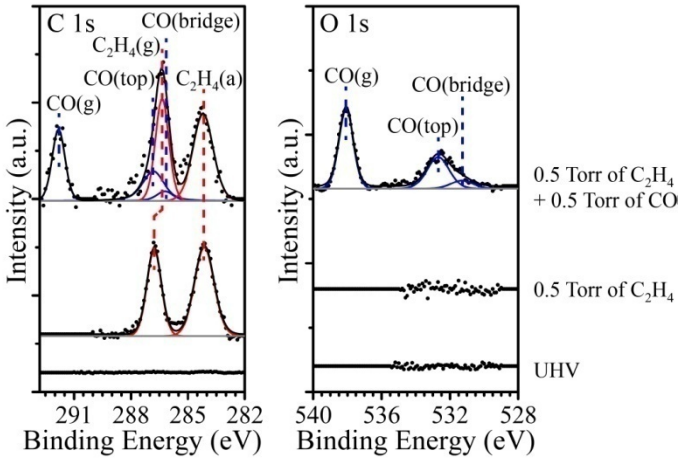

Figure 5-10. C 1s and O 1s spectra of Pt(332) under C_2H_4 and CO. These spectra were recorded in UHV, under 500 mTorr of C_2H_4, and after adding 500 mTorr of CO. Although pre-covered by ethylene-related adsorbates, Pt(332) can still accommodate about half a monolayer of CO. CO only displaces less than 10% of ethylene-related adsorbates.

Figure 5-10 and Figure 5-11 display the C 1s and O 1s spectra of both Pt surfaces recorded under 500 mTorr of C_2H_4 and after subsequent addition of 500 mTorr of CO. Under 500 mTorr of C_2H_4, two peaks are observed in C 1s spectra at ~286.2 eV and ~284.2 eV that originate from gas-phase C_2H_4 and ethylene-related adsorbates, respectively. Even though ethylidyne is considered as the major adsorbate on Pt(332) and Pt(557) because of the ethylidyne peak position at 284.3 eV,[45] detailed adsorbate composition is hard to

determine on the sole basis of XPS spectra. C−H stretch frequencies in vibrational spectra are required to determine the type of adsorbates. The total C_2H_4 coverage is estimated as ~0.50 ML on both surfaces. The absence of any O 1s peaks under 500 mTorr of C_2H_4 indicates no contamination from CO in the background gases. CO chemisorbs on both Pt surfaces as soon as 500 mTorr of CO is introduced, as shown by the growth of top-CO and bridge-CO peaks in O 1s spectra at ~532.8 and ~531.3 eV, respectively. Most of the ethylene-related adsorbates are not replaced by CO, since the C 1s peaks at ~284.2 eV keep 90% of the initial intensity on both surfaces. The gas-phase C_2H_4 peaks downshift by 0.5 eV because the sample work function has increased as a result of CO adsorption.[41,46] Both Pt surfaces admit ~0.50 ML CO, which illustrates that the ethylene-saturated stepped Pt surfaces are open to CO adsorption. However, CO does not prefer the same adsorption sites while adsorbing on the stepped surfaces pre-covered by C_2H_4. From the peak areas in O 1s spectra, the top-to-bridge CO ratio is 4.0 on Pt(332) but 0.7 on Pt(557). Such discrepancy in CO preferential adsorption sites could be due to distinct structures initially under pure C_2H_4 resulted from the different step orientations.

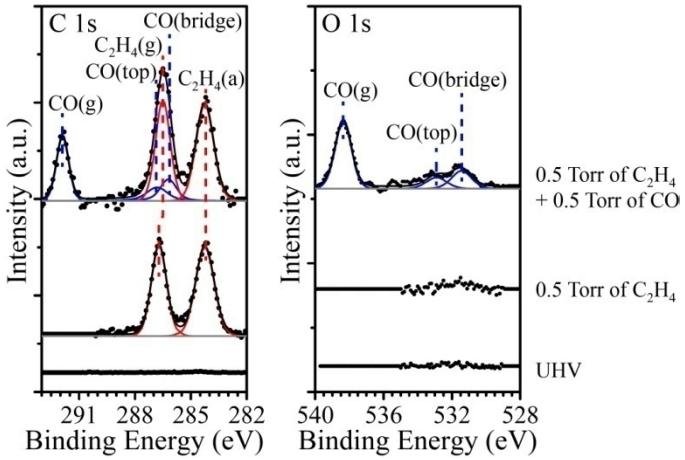

Figure 5-11. C 1s and O 1s spectra of Pt(557) taken in UHV, under 500 mTorr of C_2H_4, and after adding 500 mTorr of CO. The Pt(557) surface pre-covered by C_2H_4 also admits about 0.50 ML CO. Less than 10% of ethylene-related adsorbate molecules are displaced by CO.

5.4 Conclusions

In conclusion, surface restructuring processes on Pt(332) and Pt(557), which have the same terraces but differ in step orientations, are investigated under the mixture of C_2H_4 and CO in the Torr range at 298 K. HP-STM and AP-XPS results reveal that surface reconstruction relies on the step geometry as well as the sequence of gas introduction. When adding CO first, nanometer-sized Pt clusters are formed at step edges on both Pt(332) and Pt(557), although the cluster shapes are different. The subsequent addition of C_2H_4 can remove Pt

clusters on Pt(332) owing to ethylidyne adsorption, whereas clusters on Pt(557) are preserved. AP-XPS spectra demonstrate that C_2H_4 is capable of adsorbing on both Pt surfaces pre-covered by CO at a low coverage, through displacing a similar amount of CO. Under 500 mTorr of pure C_2H_4, ethylidyne leads to a periodic structure at (111) steps on Pt(332). In contrast, no periodic structure is resolved at (100) steps on Pt(557). The subsequent CO introduction does not create any Pt clusters, probably since the CO coverage is lower in co-adsorption with ethylidyne, and because the strong Pt−ethylidyne bonding increases the Pt diffusion barrier. AP-XPS results have shown that the C_2H_4 and CO coverage are similar on both Pt surfaces. The preferential adsorption sites of CO are also affected by step orientations—CO prefers to occupy top sites on Pt(332) as compared to on Pt(557) under the same gas environments.

5.5 References

(1) Somorjai, G. A.; Li, Y. *Introduction to Surface Chemistry and Catalysis*; 2nd ed.; Johns Wiley & Sons, Inc.: Hoboken, NJ, 2010.

(2) Vattuone, L.; Savio, L.; Rocca, M. *Surf. Sci. Rep.* **2008**, *63*, 101-168.

(3) Yates, J. J. T. *J. Vac. Sci. Technol., A* **1995**, *13*, 1359-1367.

(4) Abild-Pedersen, F.; Lytken, O.; Engbæk, J.; Nielsen, G.; Chorkendorff, I.; Nørskov, J. K. *Surf. Sci.* **2005**, *590*, 127-137.

(5) Siddiqui, H. R.; Chen, P. J.; Guo, X.; J. T. Yates, Jr. *J. Chem. Phys.* **1990**, *92*, 7690-7699.

(6) Kim, J.; Samano, E.; Koel, B. E. *J. Phys. Chem. B* **2006**, *110*, 17512-17517.

(7) Gee, A. T.; Hayden, B. E. *J. Chem. Phys.* **2000**, *113*, 10333-10343.

(8) Vang, R. T.; Honkala, K.; Dahl, S.; Vestergaard, E. K.; Schnadt, J.; Lægsgaard, E.; Clausen, B. S.; Nørskov, J. K.; Besenbacher, F. *Nat. Mater.* **2005**, *4*, 160-162.

(9) Zambelli, T.; Wintterlin, J.; Trost, J.; Ertl, G. *Science* **1996**, *273*, 1688-1690.

(10) Nørskov, J. K.; Bligaard, T.; Rossmeisl, J.; Christensen, C. H. *Nature Chem.* **2009**, *1*, 37-46.

(11) Gee, A. T.; Hayden, B. E.; Mormiche, C.; Kleyn, A. W.; Riedmuller, B. *J. Chem. Phys.* **2003**, *118*, 3334-3341.

(12) Xu, J.; Henriksen, P.; Yates, J. J. T. *J. Chem. Phys.* **1992**, *97*, 5250-5252.

(13) Hendriksen, B. L. M.; Ackermann, M. D.; van Rijn, R.; Stoltz, D.; Popa, I.; Balmes, O.; Resta, A.; Wermeille, D.; Felici, R.; Ferrer, S.; Frenken, J. W. M. *Nature Chem.* **2010**, *2*, 730-734.

(14) Bernasek, S. L.; Siekhaus, W. J.; Somorjai, G. A. *Phys. Rev. Lett.* **1973**, *30*, 1202-1204.

(15) Lin, T. H.; Somorjai, G. A. *J. Chem. Phys.* **1984**, *81*, 704-709.

(16) Salmeron, M.; Gale, R. J.; Somorjai, G. A. *J. Chem. Phys.* **1979**, *70*, 2807-2818.

(17) Lewis, H. D.; Burnett, D. J.; Gabelnick, A. M.; Fischer, D. A.; Gland, J. L. *J. Phys.*

Chem. B **2005**, *109*, 21847-21857.

(18)Okada, M.; Vattuone, L.; Moritani, K.; Savio, L.; Teraoka, Y.; Kasai, T.; Rocca, M. *Phys. Rev. B* **2007**, *75*, 233413.

(19)Zhu, Z.; Tao, F.; Zheng, F.; Chang, R.; Li, Y.; Heinke, L.; Liu, Z.; Salmeron, M.; Somorjai, G. A. *Nano Lett.* **2012**, *12*, 1491-1497.

(20)Dahl, S.; Logadottir, A.; Egeberg, R. C.; Larsen, J. H.; Chorkendorff, I.; Törnqvist, E.; Nørskov, J. K. *Phys. Rev. Lett.* **1999**, *83*, 1814-1817.

(21)Logadóttir, Á.; Nørskov, J. K. *J. Catal.* **2003**, *220*, 273-279.

(22)Housmans, T. H. M.; Koper, M. T. M. *J. Phys. Chem. B* **2003**, *107*, 8557-8567.

(23)Kuzume, A.; Herrero, E.; Feliu, J. M. *J. Electroanal. Chem.* **2007**, *599*, 333-343.

(24)Spendelow, J. S.; Xu, Q.; Goodpaster, J. D.; Kenis, P. J. A.; Wieckowski, A. *J. Electrochem. Soc.* **2007**, *154*, F238-F242.

(25)Tao, F.; Dag, S.; Wang, L. W.; Liu, Z.; Butcher, D. R.; Bluhm, H.; Salmeron, M.; Somorjai, G. A. *Science* **2010**, *327*, 850-853.

(26)Batteas, J. D.; Dunphy, J. C.; Somorjai, G. A.; Salmeron, M. *Phys. Rev. Lett.* **1996**, *77*, 534-537.

(27)Sander, M.; Imbihl, R.; Schuster, R.; Barth, J. V.; Ertl, G. *Surf. Sci.* **1992**, *271*, 159-169.

(28)Hahn, E.; Schief, H.; Marsico, V.; Fricke, A.; Kern, K. *Phys. Rev. Lett.* **1994**, *72*, 3378-3381.

(29)Klikovits, J.; Schmid, M.; Merte, L. R.; Varga, P.; Westerström, R.; Resta, A.; Andersen, J. N.; Gustafson, J.; Mikkelsen, A.; Lundgren, E.; Mittendorfer, F.; Kresse, G. *Phys. Rev. Lett.* **2008**, *101*, 266104.

(30)Ainsworth, M. K.; McCoustra, M. R. S.; Chesters, M. A.; Sheppard, N.; De La Cruz, C. *Surf. Sci.* **1999**, *437*, 9-17.

(31)Chen, P.; Kung, K. Y.; Shen, Y. R.; Somorjai, G. A. *Surf. Sci.* **2001**, *494*, 289-297.

(32)Rioux, R. M.; Hoefelmeyer, J. D.; Grass, M.; Song, H.; Niesz, K.; Yang, P.; Somorjai, G. A. *Langmuir* **2007**, *24*, 198-207.

(33)Lundwall, M. J.; McClure, S. M.; Goodman, D. W. *J. Phys. Chem. C* **2010**, *114*, 7904-7912.

(34)Tang, D. C.; Hwang, K. S.; Salmeron, M.; Somorjai, G. A. *J. Phys. Chem. B* **2004**, *108*, 13300-13306.

(35)Tao, F.; Tang, D. C.; Salmeron, M.; Somorjai, G. A. *Rev. Sci. Instrum.* **2008**, *79*, 084101.

(36)Grass, M. E.; Karlsson, P. G.; Aksoy, F.; Lundqvist, M.; Wannberg, B.; Mun, B. S.; Hussain, Z.; Liu, Z. *Rev. Sci. Instrum.* **2010**, *81*, 053106.

(37)Powell, C. J.; Jablonski, A. *NIST Electron Inelastic Mean Free Path Database, version 1.2*; National Institute of Standards and Technology: Gaithersburg, MD, 2010.

(38)Dean, J. A. *Lange's Handbook of Chemistry*; 15th ed.; McGraw-Hill Professional,

1998.

(39) Longwitz, S. R.; Schnadt, J.; Vestergaard, E. K.; Vang, R. T.; Laegsgaard, E.; Stensgaard, I.; Brune, H.; Besenbacher, F. *J. Phys. Chem. B* **2004**, *108*, 14497-14502.

(40) Land, T. A.; Michely, T.; Behm, R. J.; Hemminger, J. C.; Comsa, G. *J. Chem. Phys.* **1992**, *97*, 6774-6783.

(41) Norton, P. R.; Goodale, J. W.; Selkirk, E. B. *Surf. Sci.* **1979**, *83*, 189-227.

(42) Montano, M.; Bratlie, K. M.; Salmeron, M.; Somorjai, G. A. *J. Am. Chem. Soc.* **2006**, *128*, 13229-13234.

(43) Tränkenschuh, B.; Papp, C.; Fuhrmann, T.; Denecke, R.; Steinrück, H. P. *Surf. Sci.* **2007**, *601*, 1108-1117.

(44) Papp, C.; Tränkenschuh, B.; Streber, R.; Fuhrmann, T.; Denecke, R.; Steinrück, H. P. *J. Phys. Chem. C* **2007**, *111*, 2177-2184.

(45) Freyer, N.; Pirug, G.; Bonzel, H. P. *Surf. Sci.* **1983**, *126*, 487-494.

(46) Axnanda, S.; Scheele, M.; Mao, B.; Crumlin, E.; Chang, R.; Shan, K.; Mohamed, F.; Alivisatos, A. P.; Liu, Z. *in preparation*.

Chapter 6

Changes in Structure and Mobility on the Pt(100)-hex Surface Induced by Ethylene and its Mixture with Hydrogen and Carbon Monoxide

(This chapter covers similar materials as in Zhu, Z. *et al.*, *J. Phys. Chem. C* **2013**, *117*, 2799-2804 – reproduced with permission, copyright 2013 American Chemical Society; and Butcher, D. R.; Zhu, Z. *et al.*, *Chem. Commun.* **2013**, *49*, 6903-6905 – reproduced by permission of the Royal Society of Chemistry.)

Abstract

This chapter is devoted to studies in the structure and mobility of the Pt(100) surface in the presence of gas-phase ethylene, and its mixture with hydrogen and carbon monoxide at 298 K. HP-STM shows that the hexagonal reconstruction on the clean Pt(100) surface is preserved under 1 Torr of C_2H_4. The Pt(100) surface is saturated by mobile ethylidyne and di-σ-bonded ethylene adsorbates. The concept of surface mobility also applies to the metal atoms, because ethylene-related adsorbates weaken Pt−Pt bonds and thus facilitate displacements of Pt atoms in the hexagonal layer. At 5×10^{-6} Torr of C_2H_4, co-adsorbed CO from background gases lifts the reconstruction, with the excess Pt atoms from the initial hexagonal layer forming Pt islands across the surface. The chemisorption of CO from vacuum background gases, in the nominally pure C_2H_4, is revealed by AP-XPS. Adsorbates are mobile and the Pt(100) catalyst is active under the mixture of 500 mTorr of C_2H_4 and 500 mTorr of H_2, but adding 3 mTorr of CO into the C_2H_4-H_2 mixture quenches the mobility and deactivates the Pt catalyst. Meanwhile, the hexagonal reconstruction is also lifted.

6.1 Introduction

The Pt(100) surface is an appealing system in surface science studies, because it shows structures that are different from those of the bulk layers. LEED measurements revealed that above 440 K in vacuum, the topmost layer of the clean surface rearranges from the square lattice characteristic of the bulk planes to a densely packed quasi-hexagonal layer.[1-5] The long-range periodicity of the reconstructed surface was found to be (5 × 20) or (5 × 25) with respect to that of the (1 × 1) bulk structure, which is generally denoted as Pt(100)-hex.[2] The surface strain resulted from the lattice mismatch between the hexagonal overlayer and the square bulk termination is balanced by the energy gain through the close packing.[6] When heating the Pt(100)-hex surface to above 1100 K, the top hexagonal layer rotates by 0.7º with respect to the second layer, forming a superstructure named as Pt(100)-hex-R0.7º.[2,5] Both Pt(100)-hex and Pt(100)-hex-R0.7º reconstructions can be lifted by exposure to CO,[7-14] O_2,[14-16] NO,[13,17,18] and benzene,[11] leading to the formation of islands by the excess Pt atoms from the initial hexagonally reconstructed Pt(100) surface.

Ethylene hydrogenation has long been studied as a model reaction in heterogeneous catalysis on Pt catalysts. This reaction is structure insensitive, since the turnover rate was observed to be independent on the Pt catalyst structure.[19-22] Investigation of ethylene adsorption structure on Pt catalysts can help understand the structure insensitivity of ethylene hydrogenation. Early studies of ethylene adsorption on Pt(100)-hex have revealed that C_2H_4 adsorbs molecularly as a di-σ-bonded complex at 120 K, favoring the three-fold hollow sites at the surface.[23] At 350 K, all the di-σ-bonded ethylene rearranges to ethylidyne that centers on three-fold sites as well, with the hydrogen generated by the reaction desorbing from the surface. In contrast, on the (1 × 1) Pt(100) surface, C_2H_4 decomposes through another pathway in which vinylidene is suggested as the intermediate. At high pressures (35 Torr) of C_2H_4 at room temperature, SFG vibrational spectra have shown that both ethylidyne and di-σ-bonded ethylene are present on the Pt(100) surface.[24] At catalytically active temperatures and pressures, the most reactive pathway for ethylene hydrogenation involves the π-bonded ethylene species, whereas the reaction of hydrogen with ethylidyne and di-σ-bonded ethylene occurs relatively slowly.

It was reported in literature that C_2H_4 is able to remove the hexagonal reconstruction on Pt(100), like CO, O_2 and NO,. Exposure of Pt(100)-hex to C_2H_4 at room temperature leads to the disappearance of the one-fifth order diffraction spots in LEED.[25,26] Using STM, Ritter *et al.*[13] first observed a heterogeneous nucleation process beginning at lattice defects for the ethylene-induced removal of the hexagonal reconstruction, followed by anisotropic growth of the (1 × 1) structure related to the orientation of the original reconstructed surface. Rønning *et al.*[27] showed that 2×10^{-8} mbar of C_2H_4 can cause the (1 × 1) island domains to form on Pt(100)-hex-R0.7º. In a series of experiments with C_2H_4 exposures ranging from 9 to 72 L, the islands were found to grow following the direction of stripes on the reconstructed surface. Heating the ethylene-saturated Pt(100) surface in vacuum does

not lead to graphite formation as is the case on Pt(111), but results in a partial relaxation of the surface back to the hexagonal layer at 670 K. The outermost layer is fully rearranged to the quasi-hexagonal pattern above 900 K.[27]

The advent of *in situ* characterization techniques such as HP-STM and AP-XPS renders it possible to study the important reconstruction processes of catalyst surfaces, in the presence of gases well beyond the pressure limits that were previously accessible. Apart from unraveling surface structure at the molecular level under gas environments close to real catalytic conditions,[11,28-33] HP-STM can reveal dynamic aspects such as adsorbate mobility and its correlation with catalytic activity.[34-37] The mobility of adsorbed species at the catalyst surface is a crucial requisite for reactant molecules to access favorable sites for catalytic turnovers. In contrast, immobile species that strongly chemisorb on the surface can hinder the diffusion of reactants, block the active sites, and ultimately deactivate the catalysts. A less studied aspect of the surface mobility is the movement of catalyst atoms, which can be facilitated by the weakening of metal−metal bonds as a result of the chemisorption of reactants.

Our group have observed that, during the hydrogen and deuterium exchange reaction (200 mTorr of H_2 and 20 mTorr of D_2 at 298 K), no surface order is discernible on Pt(111) in the STM images by virtue of the high adsorbate mobility.[35] Both the adsorbate diffusion and the reaction stop upon introducing CO, accompanied by the formation of ordered CO adsorption patterns. Chemisorbed CO molecules poison the reaction through raising the diffusion barrier for reactants and blocking the active sites.[37] Partial desorption of CO by heating to 345 K and above regenerates ensembles of vacancy sites for adsorption as well as dissociation of reactants and opens adsorbate diffusion pathways, hence reactivating the Pt catalyst.[35]

This chapter studies structure and mobility on Pt(100) under pure C_2H_4 and under the mixture of C_2H_4, H_2 and CO at pressures in the Torr range. The hexagonal reconstruction is preserved on Pt(100) under 1 Torr of C_2H_4, and both ethylene-related adsorbates and substrate Pt atoms are mobile on the surface. At 5×10^{-6} Torr of C_2H_4, however, background CO co-adsorbs with C_2H_4 and lifts the hexagonal reconstruction, which cannot be re-established when further increasing the C_2H_4 pressure to 1 Torr. Under 1 Torr of 1:1 C_2H_4-H_2 mixture, the adsorbates move rapidly with the occurrence of ethylene hydrogenation, whereas subsequent introduction of 3 mTorr of CO suppresses the adsorbate mobility and deactivates the Pt catalyst. The hexagonal reconstruction on the Pt(100) surface is also lifted by CO adsorption.

6.2 Experimental Section

HP-STM experiments were conducted in the home-built system that was described in Chapter 2.[38] A clean Pt(100)-hex crystal was prepared by Ar^+ sputtering at 1000 eV at 298 K for 20 min, annealing at 10^{-7} Torr of O_2 at 923 K for 5 min and annealing in vacuum at

1073 K for 15 min. The sputtering and annealing cycles were repeated until the Auger spectra showed the absence of impurities on the Pt(100)-hex sample surface. All the STM images were recorded at 298 K using electrochemically etched tungsten tips,[39] with a sample bias of +0.1~0.2 V and a tunneling current of 0.1~0.2 nA.

AP-XPS measurements were carried out at Beamline 9.3.2 at ALS in LBNL.[40,41] The Pt(100)-hex crystal was cleaned by the identical procedure to that before STM experiments, and the surface was analyzed with XPS to confirm that no contaminants were present. Pt 4f, C 1s and O 1s core level spectra were acquired at incident X-ray photon energies of 340 eV, 570 eV and 810 eV, respectively, such that photoelectrons with similar kinetic energies (~280 eV) were generated, in order to ensure the same surface sensitivity (~0.6 nm) for all the elements.[42] The energy position of each XPS spectrum was calibrated with respect to the Fermi edge at 0 eV. After intensity normalization and background subtraction, the integrated peak areas were employed to monitor the CO and C_2H_4 coverage on Pt(100). The CO coverage is estimated based on the O 1s to Pt 4f peak area ratio, with a calibration using 0.50 ML CO on Pt(557) at 5×10^{-9} Torr.[28] The coverage of C_2H_4 is estimated through the C 1s to Pt 4f area ratio, by assuming the same sensitivity factor of carbon atoms in C_2H_4 and CO.

Catalytic studies were performed in a batch reactor equipped with a boron nitride heater and a re-circulation pump for gas mixing. Since the reactor is not equipped with a sputter ion gun and because the base pressure of the reactor is in the 10^{-7} Torr range, the Pt(100) crystal was cleaned in the reactor by cycles of annealing in O_2 and in vacuum. The gas composition of the reaction mixture was detected by gas chromatograph with a thermal conductivity detector. The conversion of C_2H_4 was measured in a time scale comparable to the durations of HP-STM and AP-XPS experiments.

6.3 Results and Discussion

6.3.1 Clean Pt(100)-hex

Figure 6-1a,b show the model of the Pt(100)-hex surface, in which a quasi-hexagonal overlayer of Pt atoms reside on top of the underlying (100) plane.[1] The distances between the Pt atoms in the topmost hexagonal layer have decreased by 3.8% relative to the bulk value,[43] such that six rows of atoms in the reconstructed layer commensurately fit over five rows of atoms in the substrate along the [011] direction. The quasi-hexagonal overlayer accordingly contains ~25% more Pt atoms than the (1×1) layer. Figure 6-1c,d show the STM image of the clean Pt(100)-hex surface and a 7 nm topography line profile along the [011] direction, respectively. The mismatch between the top two layers results in ~30 pm modulation of the atomic heights along the [011] direction, causing the appearance of parallel stripes under STM. The average spacing between the stripes is 1.4 nm, as shown in Figure 6-1d, in accordance with the width of five atomic rows on the substrate.

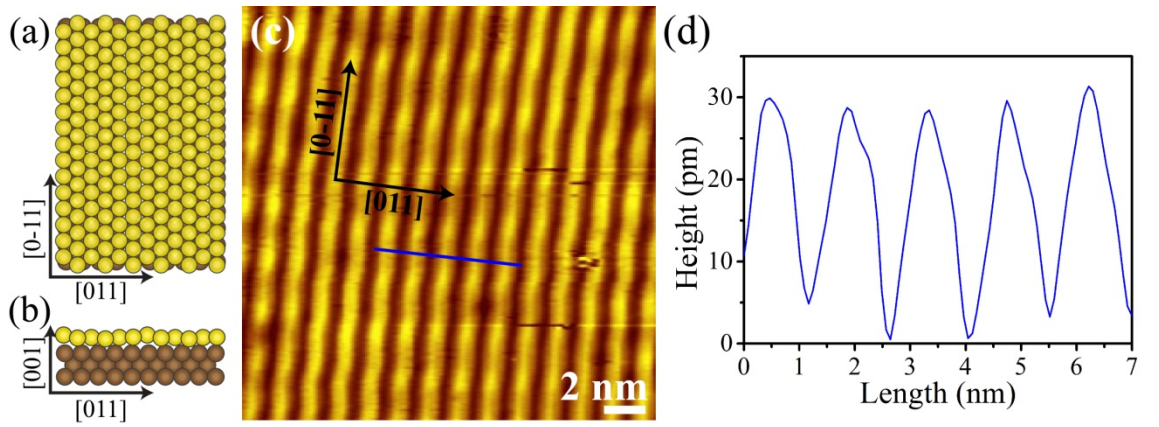

Figure 6-1. (a) Top view and (b) side view of the model of the Pt(100)-hex surface. Yellow and brown balls represent the surface and the bulk layers, respectively. Only the first layer is hexagonally reconstructed. (c) STM image of Pt(100)-hex in UHV and (d) the topographic profile of the line in (c). The periodicity along the [011] direction is 1.4 nm and the height corrugation is ~30 pm, compared to a monatomic step height of 220 pm.

6.3.2 High Pressures of C_2H_4

Figure 6-2a shows that, after introducing 1 Torr of C_2H_4 into the HP-STM system, the stripes characteristic of the hexagonal reconstruction are preserved. The structure is stable under 1 Torr of C_2H_4 at 298 K even after several hours of exposure. A line scan profile along the [011] direction, as in Figure 6-2b, reveals that the row periodicity remains at 1.4 nm. Since the major species on Pt(100) at high C_2H_4 pressures are ethylidyne and di-σ-bonded ethylene that both favor three-fold hollow sites on the hexagonal overlayer,[24] the reconstruction appears to be preserved by these species. The height corrugation increases from ~30 to ~120 pm, because the presence of ethylidyne and di-σ-bonded ethylene alters the electronic structure of the Pt(100)-hex surface, which affects the tunneling probability and hence changes the apparent heights. The high coverage of ethylidyne and di-σ-bonded ethylene at high gas pressures also enhances the noise level at surface, causing some stripes to distort.

In addition, ethylidyne and di-σ-bonded ethylene adsorbates diffuse rapidly across the surface under 1 Torr of C_2H_4 in the time scale of STM imaging, in the sense that the stripes become blurred in Figure 6-2a as compared with the sharp stripes in UHV in Figure 6-1c, with no molecular details of the adsorbates resolved. Similarly, on the close-packed Pt(111) surface, ethylidyne is not resolvable by STM unless the system is cooled to below 230 K, although a sharp (2 × 2) pattern is observable by LEED above 230 K.[44] The high mobility of ethylidyne adsorbates on Pt(111) is due to the low diffusion barrier of ~0.11 eV.[45] Given the similarity in atomic packing between the Pt(100)-hex and Pt(111) surfaces, the energy barrier for ethylidyne diffusion on Pt(100)-hex can be small as well, which causes the adsorbate structure to be not resolvable.

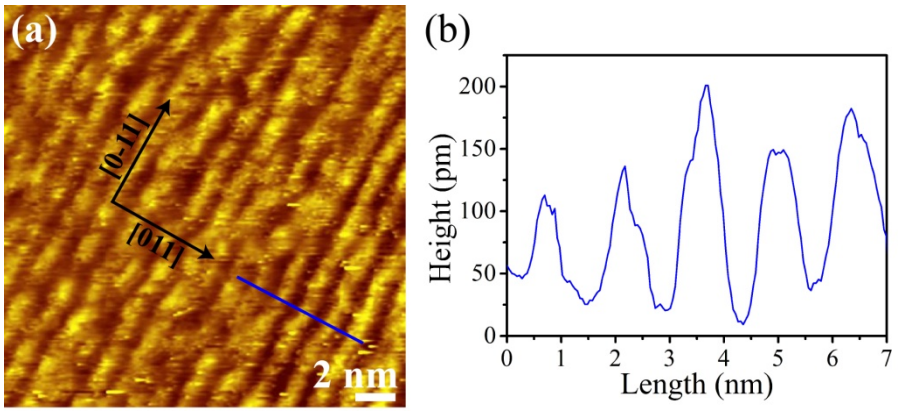

Figure 6-2. (a) STM image of Pt(100)-hex after the introduction of C_2H_4 to increase the pressure from 10^{-10} to 1 Torr. The stripes indicate that the hexagonal reconstruction is preserved. (b) Line scan profile of the blue line in (a). The periodicity along the [011] direction remains at 1.4 nm, whereas the average corrugation increases to ~120 pm.

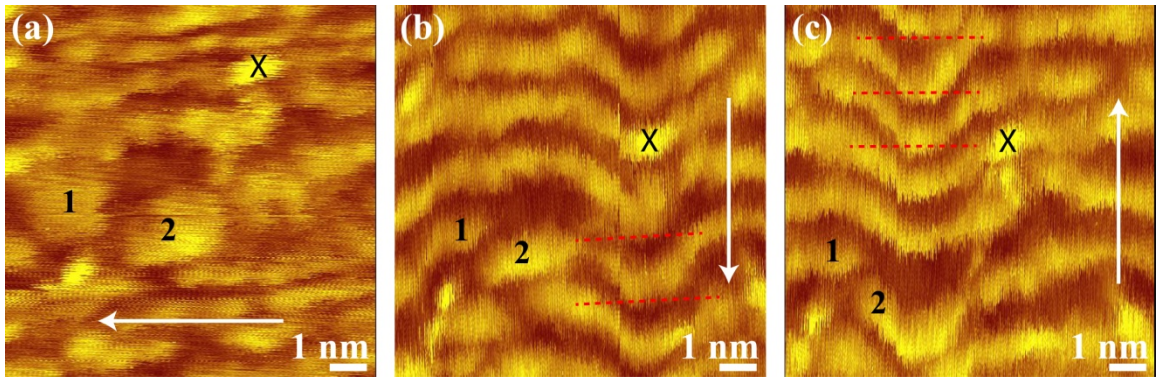

Figure 6-3. STM images of Pt(100)-hex taken under 1 Torr of C_2H_4. The white arrows mark the tip scanning direction: horizontal scans in (a) and vertical scans in (b) and (c). An impurity feature marked by "X" helps locate the relative positions of the waves of the misfit reconstruction. Figures (b) and (c) show the distortion caused by interaction with the STM tip which "pushes" the crest of the dislocation wave along the displacement direction, i.e., perpendicular to the corrugated rows.

An interesting and unexpected observation under this condition is that the Pt atoms in the hexagonal layer covered by ethylene-related adsorbates can also move under the influence of the tip, as revealed by the series of STM images in Figure 6-3. In Figure 6-3a, the tip scans from right to left, roughly parallel to the orientation of the stripes, whereas the tip scans from top to bottom and from bottom to top in Figure 6-3b,c, perpendicular to the stripes. An impurity shared by all three images, highlighted by "X", provides a spatial

reference of the location. Other defects are also present that distort the alignment of the stripes, for example the stripes appear fragmented in the locations marked by "1" and "2". When the tip scans along the stripes, the stripes appear roughly linear. However, with the tip scanning in the perpendicular direction, the stripes became distorted as shown in Figure 6-3b,c. The fragment "2" now becomes connected with the stripe on the right. Interestingly, the stripes are found to displace up or down in the image in units of the stripe period (1.4 nm), as shown by the red dashed lines. When the scanning direction makes an angle of 60º or less with the stripes, the distortion is small or not visible.

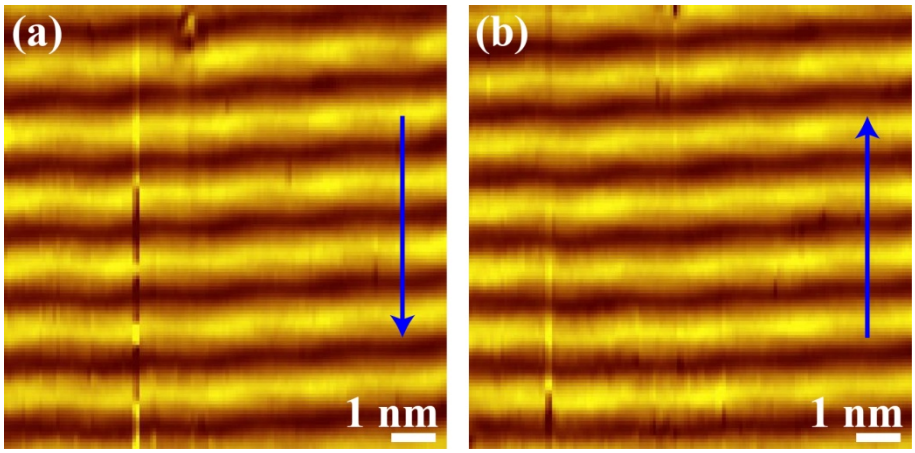

Figure 6-4. STM images of the clean Pt(100)-hex surface when scanning perpendicular to the stripes. The tip scans (a) from top to bottom and (b) from bottom to top. No surface waves are observed.

These observations can be explained by a displacement of the corrugation profile of the hexagonal layer of Pt atoms. This displacement is akin to the movement of a wave where the crest shifts when atoms in the top hexagonal layer move a small lateral distance over the substrate, resulting in a much larger displacement of the wave phase by one period. Such displacements are facilitated by the weakened Pt−Pt interactions between the first and second layers due to the adsorption of ethylene, since this waving structure is not observed on the clean Pt(100)-hex surface in the absence of ethylene-related adsorbates. Figure 6-4 displays that, when the tip scans perpendicular to the stripes in UHV, the stripes characteristic of the hexagonal layer are straight without any distortion.

Important information regarding surface composition is obtained from the peaks in the Pt 4f, C 1s and O 1s core level spectra, as shown in Figure 6-5. The spectra were collected in UHV, at 1 Torr of C_2H_4, and after gas evacuation. Pt(100)-hex is free of contaminants prior to gas introduction. At 1 Torr of C_2H_4, a shoulder arises at 71.6 eV in the Pt 4f spectrum from the surface atoms bonded to the ethylene-related adsorbates. In the C 1s spectrum, the peak at 286.8 eV is characteristic of gas-phase C_2H_4,[46] whereas the other

broad peak at 284.1 eV from surface hydrocarbon species can be deconvoluted into two components at 284.3 eV and 283.6 eV, which correspond to ethylidyne and di-σ-bonded ethylene, respectively.[47] XPS spectra have thus verified the assignment of ethylene-related adsorbates on Pt(100)-hex to ethylidyne and di-σ-bonded ethylene. The ethylidyne peak area is three times larger than the area of the di-σ-bonded ethylene peak.

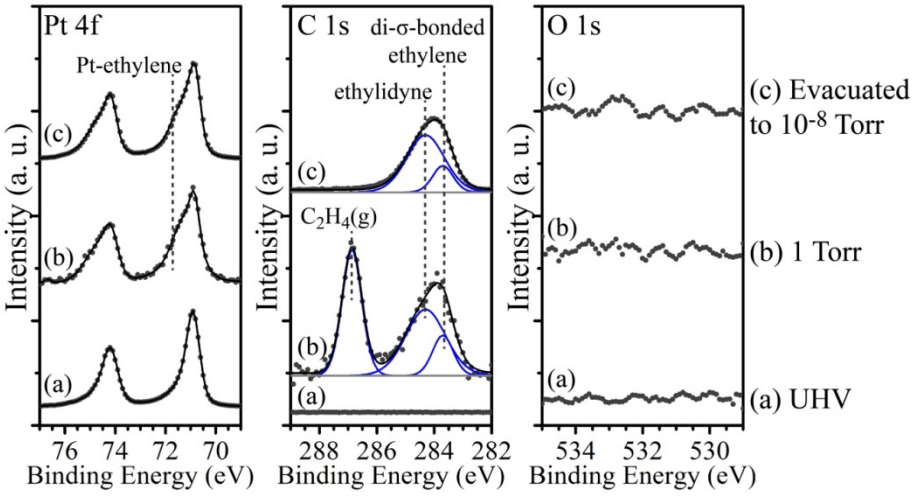

Figure 6-5. (left) Pt 4f; (center) C 1s; and (right) O 1s XPS spectra of Pt(100)-hex obtained (a) in UHV, (b) after dosing 1 Torr of C_2H_4, and (c) after gas evacuation. A Shirley-type background was subtracted from all the spectra, with the intensities scaled based on the normalization of Pt 4f peaks. Ethylidyne and di-σ-bonded ethylene saturate the surface when the C_2H_4 gas pressure reaches 1 Torr. The di-σ-bonded ethylene peak decreases in intensity after the removing gas-phase C_2H_4. The absence of oxygen peaks indicates background CO does not accumulate on Pt(100) under 1 Torr of C_2H_4.

Upon C_2H_4 evacuation to 10^{-8} Torr, the gas-phase C_2H_4 peak disappears as expected. Di-σ-bonded ethylene also partially desorbs from surface, which leads to a small decrease in the intensity of the di-σ-bonded ethylene component and thus a slight change in the overall peak shape at 284.1 eV. The partial desorption of di-σ-bonded ethylene at 298 K accords with literature reports that di-σ-bonded ethylene has two desorption peaks at 280 and 330 K.[23] The ethylidyne peak, however, remains unchanged upon evacuating C_2H_4. The absence of any O 1s peak indicates that background CO does not adsorb on Pt(100)-hex with the saturation of ethylidyne and di-σ-bonded ethylene.

The Pt(100) surface structure after evacuating C_2H_4 to 10^{-8} Torr was also studied by STM. As shown in Figure 6-6a, the stripes are still roughly maintained after removing C_2H_4 in the gas phase, indicating that the hexagonal reconstruction is still largely preserved, even though some stripes have been segmented into short pieces. The

periodicity along the [011] direction remains at 1.4 nm. On part of the Pt(100) surface, for example at the bottom left of Figure 6-6a, some stripes have broken into small islands, evidencing the lifting of the reconstruction. Subsequently, when 10^{-6} Torr of C_2H_4 is refilled into the HP-STM system, the bright stripes representative of the hexagonal reconstruction are no longer present. Figure 6-6b shows that the stripes have been replaced by 2~3 nm monatomic islands covering the entire surface, because background CO slowly accumulates onto the Pt(100) surface. The CO accumulation causes the partial (Figure 6-6a) and complete (Figure 6-6b) lifting of the hexagonal reconstruction on Pt(100), which will be further discussed in detail in the next section.

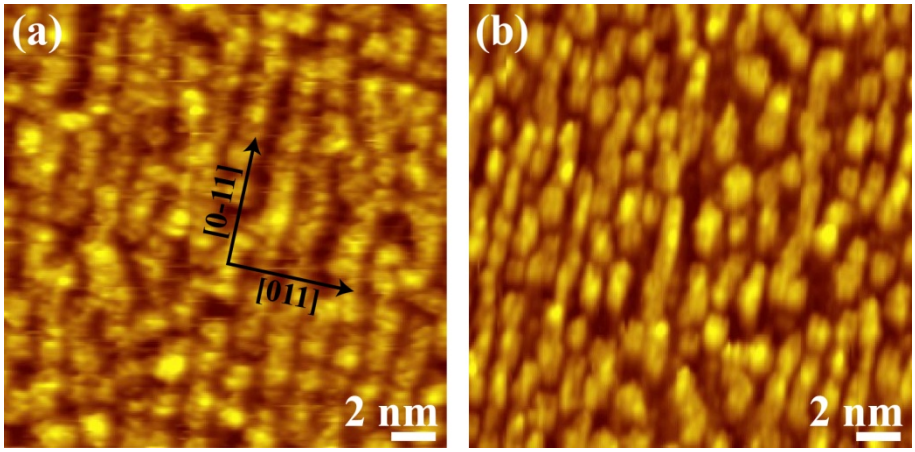

Figure 6-6. STM images of Pt(100)-hex (a) after evacuating C_2H_4 from 1 to 10^{-8} Torr, and (b) after subsequently refilling C_2H_4 to 10^{-6} Torr. The hexagonal reconstruction is roughly maintained upon evacuation, but is lifted after refilling C_2H_4 to 10^{-6} Torr.

6.3.3 Low Pressures of C_2H_4

In contrast to the observations under 1 Torr of C_2H_4 in Figure 6-2a, Figure 6-7a shows that, when exposing the clean Pt(100)-hex surface to 5×10^{-6} Torr of C_2H_4, all the bright stripes characteristic of the hexagonal reconstruction have disappeared. These stripes are replaced by a large amount of islands formed by the ~25% excess Pt atoms in the initial reconstructed surface, similar to the results in Figure 6-6b upon refilling C_2H_4 after evacuation to similar pressures. The line scan profile along the [011] direction in Figure 6-7c reveals that the island heights are ~120 pm, which is smaller than a monatomic Pt step (~220 pm) because of the close distance of islands and the finite tip radius. These islands preferentially grow following the orientation of the original bright stripes. As shown in the histograms in Figure 6-7d,e, which represent measurements of over 200 islands, the islands are 2.3 nm long along the [0-11] direction and 1.4 nm wide along the [011] direction. Moreover, the island structure is stable for several hours after a subsequent dosage of C_2H_4 to 1 Torr, as in Figure 6-7b. The hexagonal reconstruction does not re-appear with the

increase of the C_2H_4 pressure.

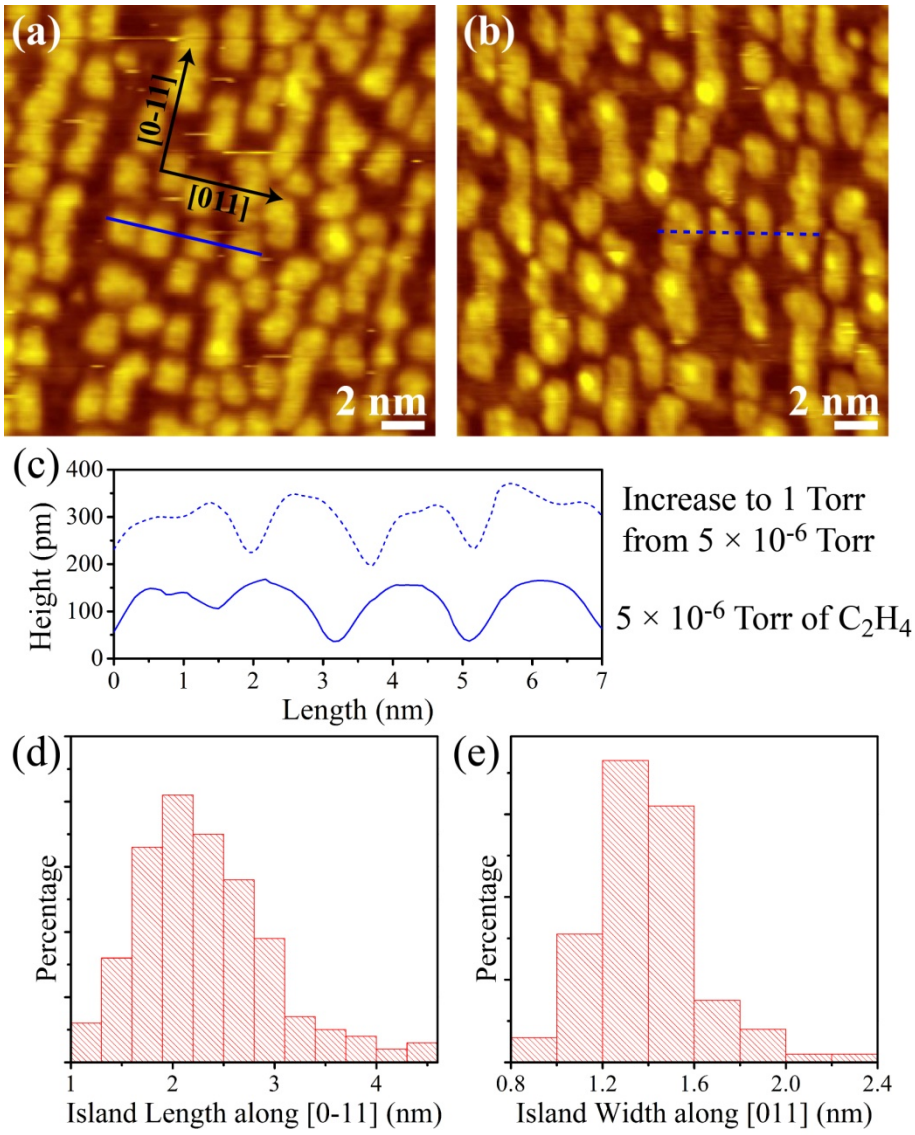

Figure 6-7. (a) STM image of Pt(100)-hex taken at 5×10^{-6} Torr of C_2H_4. The hexagonal reconstruction is lifted and the excess Pt atoms grow islands along the [0-11] direction. (b) STM image of Pt(100)-hex after increasing C_2H_4 pressure to 1 Torr from (a). The surface structure does not change from that at the initial lower pressure. (c) Topographic profiles along the blue lines in (a) and (b). The average corrugation of islands is ~120 pm in both cases. (d, e) Histograms of island sizes along [0-11] and [011] directions, respectively. The islands are 2.3 nm in length and 1.4 nm in width on average.

AP-XPS spectra provide more insight into the cause of the removal of the hexagonal reconstruction at low partial pressures of C_2H_4. Figure 6-8 displays Pt 4f, C 1s and O 1s

core level spectra acquired in UHV, at 5×10^{-6} Torr, after further increasing the C_2H_4 pressure to 1 Torr from 5×10^{-6} Torr, and after evacuation to 10^{-9} Torr. At 5×10^{-6} Torr of C_2H_4, the main C 1s peak is located at 283.7 eV for ethylene-related adsorbate species bonded to the Pt(100) surface.[48] Importantly, another feature at 286 eV is observed, which is characteristic of CO chemisorbed on Pt(100).[47] The CO peak assignment is rationalized by the presence of two O 1s peaks at 532.5 and 531.4 eV, which are assigned to CO on top and bridge sites, respectively.[36,49]

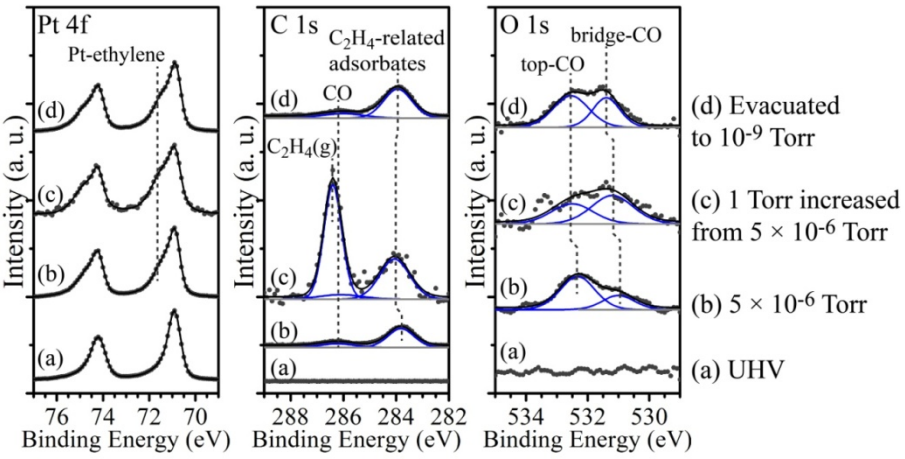

Figure 6-8. Evolution of Pt 4f (left), C 1s (center) and O 1s (right) XPS spectra with changes in C_2H_4 pressures. The spectra were taken under (a) UHV, (b) at 5×10^{-6} Torr of C_2H_4, (c) at 1 Torr of C_2H_4 increased from 5×10^{-6} Torr, and (d) after evacuation. All the spectra are normalized with respect to the intensity of Pt 4f peaks acquired under the same conditions, after a Shirley-type background subtraction. The adsorption of C_2H_4 also gives rise to the shoulder at 71.6 eV in the Pt 4f spectra. Changes in energy and intensity of the ethylene-related peaks with pressure are observed. The O 1s peaks clearly illustrates that CO incorporates onto the surface at low C_2H_4 pressures and stays on Pt(100) with the further introduction of C_2H_4.

The presence of chemisorbed CO, along with the fact that the islands in Figure 6-7a look similar to pure CO-induced islands on Pt(100) under STM,[10,11] strongly suggests that CO plays an important role in lifting the hexagonal reconstruction. The CO originates from background gases in the chamber and increases owing to displacement from the chamber walls by new gas species. At 1 Torr of C_2H_4, the saturation of ethylidyne leaves almost no vacancy on the Pt(100) surface for CO to adsorb. In addition, the short mean free path of residual background CO molecules at 1 Torr significantly decreases the probability for CO to reach the Pt surface. As a result, the hexagonal reconstruction remains under 1 Torr of C_2H_4. On the other hand, at 5×10^{-6} Torr of C_2H_4, the background CO can reach the surface

because of a longer mean free path, and adsorb owing to its strong chemisorption energy, producing a CO coverage of ~0.13 ML in our experiments.

When the C_2H_4 pressure is increased from 5×10^{-6} to 1 Torr, the CO and the gas-phase C_2H_4 C 1s peaks overlap. However, the O 1s peaks are still visible in the spectra. The bridge-CO peak becomes more intense than the top-CO peak, but the total CO coverage remains at ~0.13 ML. The shift of the surface ethylene peak to 284.0 eV suggests a change in the adsorbates on the surface, which causes some top-CO to diffuse to bridge sites. CO also lowers the amount of ethylene on the Pt(100) surface with (1 × 1) islands to be ~40% lower than that on the hexagonally reconstructed Pt(100) surface, as calculated from the areas of relevant C 1s and Pt 4f peaks. After C_2H_4 evacuation, the ethylene-related adsorbate peak shifts down to 283.9 eV in the C 1s spectra, and the CO peak, previously buried under the C_2H_4 gas peak, becomes visible again. The top-CO and bridge-CO now have similar intensity, accompanied with an increase of the CO coverage to ~0.17 ML.

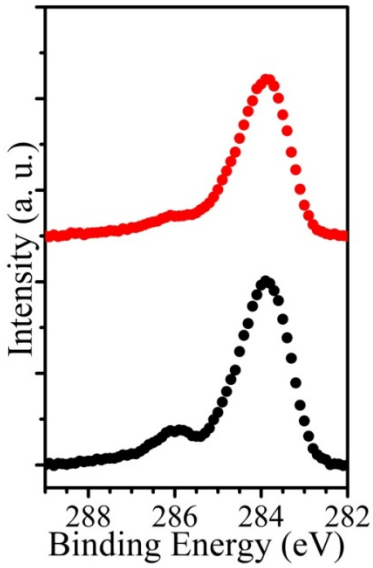

Figure 6-9. C 1s spectra of Pt(100) after evacuation from 1 Torr of C_2H_4 (increased from 5×10^{-6} Torr). The black spectrum was acquired immediately after evacuation, and the red one was recorded after heating to 500 K and then cooling to 298 K. Most of CO desorbs from Pt(100) upon heating to 500 K.

Heating the Pt(100) surface to 500 K after evacuation leads to partial desorption of CO. As in Figure 6-9, the black spectrum, which is identical to the C 1s spectrum in Figure 6-8d, shows a small peak at 286 eV next to the main peak at 283.9 eV. This small peak stems from chemisorbed CO as described previously. The red spectrum, recorded after heating the Pt(100) crystal to 500 K and cooling down to 298 K, displays a less prominent CO feature at 286 eV, implying that some CO desorbs from Pt(100) at 500 K, consistent with

temperature-programmed desorption results in literature.[9] The position and the intensity of the ethylene-related adsorbate peaks do not change during the heating-cooling process.

6.3.4 Mixture of C_2H_4 with H_2 and CO

The mobility of surface species on Pt(100)-hex was then investigated under a C_2H_4-H_2 mixture by sequentially introducing 500 mTorr of C_2H_4 and 500 mTorr of H_2 into the HP-STM cell. Figure 6-10a,b display two STM images acquired with different scan rates. At the lower rate (60 nm/s) in Figure 6-10a, no surface features can be discerned, because the adsorbates move faster than the tip on Pt(100). This phenomenon accords with our past reports on the Pt(111) surface.[35-37] When scanning at a higher rate (150 nm/s), surface structures can be resolved, because the reorganization processes of surface species now cannot be completed during the short interaction time with the tip. Bright stripes are observed in Figure 6-10b, which indicates that the hexagonal reconstruction is roughly maintained. The topography profile of the blue line vertical to the stripes shows that the average periodicity between the stripes remains at 1.4 nm, as in Figure 6-10c. Some bright spots with ~600 pm in diameter and ~50 pm in height appear on the stripes, as shown by the topography of the black line in Figure 6-10c.

Figure 6-10d,e show that, after adding 3 mTorr of CO into the C_2H_4-H_2 mixture, the surface mobility is immediately quenched, because structures can be resolved at the scan rate of both 60 nm/s and 150 nm/s. In addition, the hexagonal reconstruction is lifted, and the excess Pt atoms in the initial hexagonal layer form ~2 nm wide islands across the Pt(100) surface, as displayed in the topography profile in Figure 6-10f. Changes in mobility, activity, and structures are due to the adsorption of CO, as verified by AP-XPS. H_2 was not used in the AP-XPS experiments since turbo pumps in the differential pumping system do not pump H_2 efficiently, which strongly attenuates the XPS signal. Figure 6-11a,b shows that CO is initially absent at the Pt(100) surface in UHV and under 900 mTorr of C_2H_4. Two O 1s peaks, evidencing the CO chemisorption on Pt(100), grow after decreasing the C_2H_4 pressure to 500 mTorr and subsequently dosing 10 mTorr of CO, as in Figure 6-11c. More than 90% of the ethylene-related adsorbates remain on the Pt(100) surface after CO incorporation, in agreement with results on other Pt surfaces,[50-52] since the area of C 1s peak at ~284 eV decreases by less than 10%. Ethylidyne and di-σ-bonded ethylene may convert to vinylidene, since the island structure on Pt(100) does not have three-fold sites.[23]

Under 900 mTorr of C_2H_4, a total amount of ~0.83 ML C_2H_4 is present at the Pt(100) surface. After evacuating C_2H_4 to 500 mTorr and introducing 10 mTorr of CO, the C_2H_4 coverage decreases to ~0.78 ML and ~0.30 ML CO chemisorbs onto Pt(100). The amount of adsorbed CO is much more than that of desorbed C_2H_4, because the CO-induced island formation opens more adsorption sites on the surface. Accordingly, the Pt(100) surface can accommodate more adsorbates in the co-adsorption of C_2H_4 and CO.

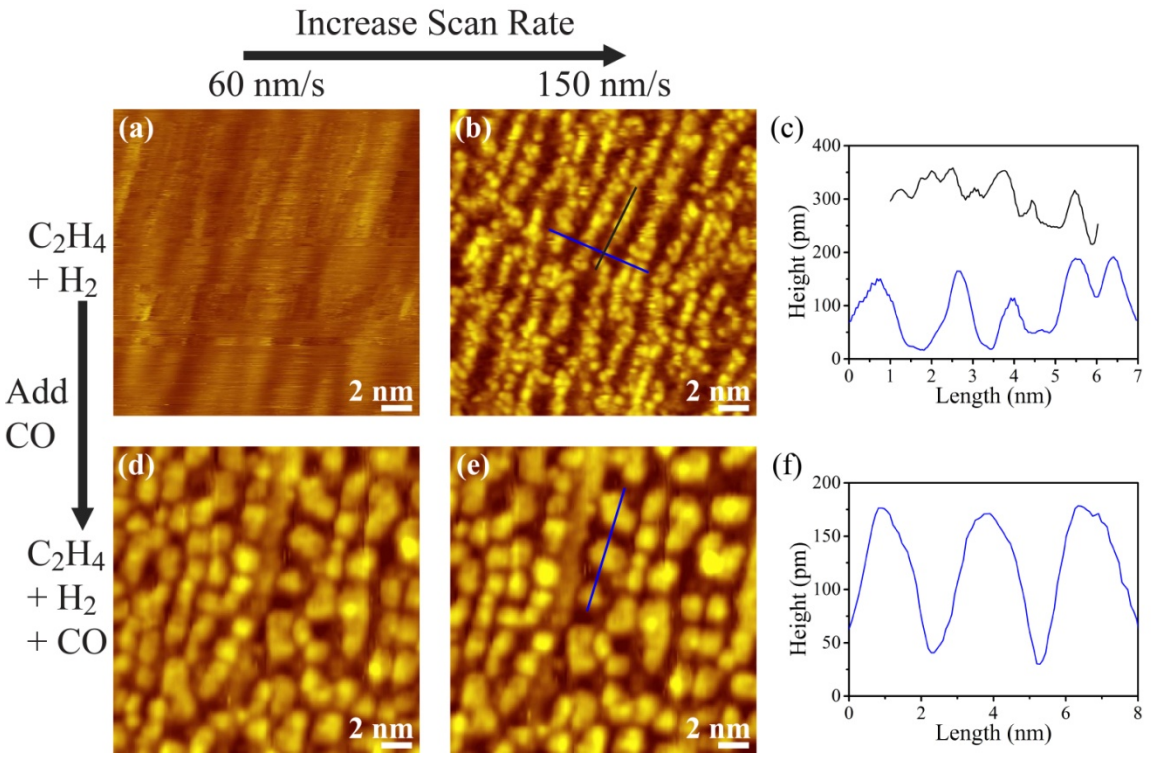

Figure 6-10. Top: STM images of Pt(100)-hex under the mixture of 500 mTorr of C_2H_4 and 500 mTorr of H_2 at a scan speed of (a) 60 nm/s and (b) 150 nm/s. No clear structures can be seen in (a) owing to rapid motion of surface atoms and molecules whereas at the higher scan rate in (b), surface structures are resolved. The topography profiles of the blue and the black lines in (b) are shown in (c). Bottom: STM images of Pt(100) recorded after addition of 3 mTorr of CO into the mixture of 500 mTorr of C_2H_4 and 500 mTorr of H_2, at the scan rate of (d) 60 nm/s and (e) 150 nm/s. CO quenches the adsorbate mobility and lifts the reconstruction, producing Pt islands of around 2 nm in lateral size. (f) Line profile of the blue line in (e).

Additional to changes in coverage, the position of C 1s peaks has also shifted after introducing CO. Two peaks can be observed at 900 mTorr of C_2H_4, one at 286.9 eV from the gas-phase C_2H_4 and the other at 284.2 eV from ethylene-related adsorbates, mainly ethylidyne and di-σ-bonded ethylene. With the introduction of CO, the ethylene-related adsorbate peak shifts down towards 284.0 eV, suggesting changes in the chemical state of the ethylene-related adsorbate, most likely into vinylidene. The C 1s peak of chemisorbed CO is buried under the gas-phase C_2H_4 peak, which shifts downwards to 286.5 eV since CO adsorption changes the sample work function.

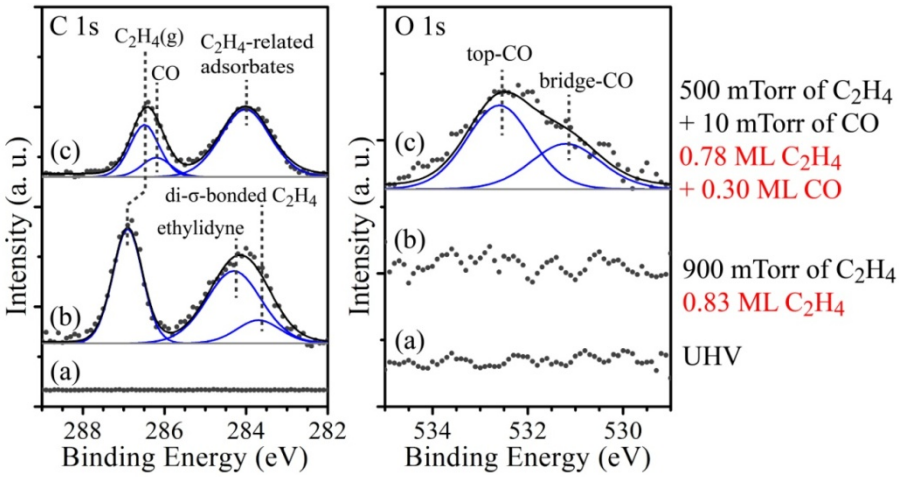

Figure 6-11. Normalized (left) C 1s and (right) O 1s core level spectra of the Pt(100) surface recorded (a) in UHV, (b) under 900 mTorr of C_2H_4, and (c) after decreasing the C_2H_4 pressure to 500 mTorr and adding 10 mTorr of CO. A Shirley-type background was subtracted from the spectra before normalization to the Pt 4f peak intensities obtained under the same gas environments. CO chemisorbs onto the Pt(100) surface and forms a mixture with ethylene-related adsorbates. 95% of the ethylene-related adsorbates estimated according to the peak area remain on Pt(100) upon the addition of CO.

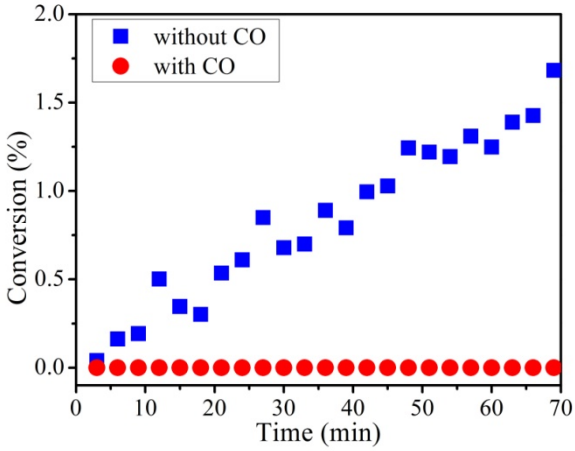

Figure 6-12. Conversion of ethylene to ethane on the Pt(100) surface in a 1:1 ethylene hydrogenation reaction mixture as a function of time. The Pt(100) catalyst is active without CO (blue squares) but inactive with CO (red circles).

In order to comprehend the correlation between mobility and activity on the Pt(100) surface, catalytic studies were performed in a batch reactor that is equipped with a boron nitride heater and a re-circulation pump for gas mixing. Because the base pressure of the

reactor is ~10^{-7} Torr and the pressure gauge in the reactor reads only down to 0.1 Torr, the reactions were carried out at a higher total pressure of gas mixtures but under a similar pressure ratio to the ratio in Figure 6-10. The reactor was initially filled with 10 Torr of C_2H_4, 10 Torr of H_2, and 740 Torr of He at 298 K. As shown in Figure 6-12, the ethylene conversion slowly increases with reaction time in the time scale of HP-STM and AP-XPS experiments, which indicates a catalytically active Pt(100) surface. In contrast, under the mixture of 10 Torr of C_2H_4, 10 Torr of H_2, 0.1 Torr of CO, and 740 Torr of He, when the surface mobility is quenched by CO, no conversion is detected at 298 K. Accordingly, the chemisorption of CO is not only quenches the diffusion of ethylene-related adsorbates, but also renders the Pt(100) surface inactive in ethylene hydrogenation.

6.4 Conclusions

In summary, using HP-STM and AP-XPS, the interaction between the Pt(100)-hex surface and C_2H_4 and its mixture with H_2 and CO was studied at pressures up to 1 Torr at 298 K. Under 1 Torr of C_2H_4, the Pt(100)-hex surface retains the hexagonal reconstruction while being covered with a mobile layer of di-σ-bonded ethylene and ethylidyne, which occupy the three-fold hollow sites on the hexagonally reconstructed Pt(100) surface. The saturation of ethylene-related adsorbates prevents the adsorption of background CO, which has also a lower incidence rate on the surface owing to the shorter mean free path at 1 Torr. At 5×10^{-6} Torr of C_2H_4, however, background CO molecules are able to co-adsorb on Pt(100). The reconstruction is therefore lifted, with 2~3 nm islands forming across the surface. Further increasing the C_2H_4 pressure from 5×10^{-6} to 1 Torr does not re-establish the hexagonal reconstruction owing to the presence of CO.

Except for adsorbates, Pt atoms in the hexagonally reconstructed layer on Pt(100) are also mobile under the influence of the tip under 1 Torr of C_2H_4. Scanning perpendicular to the stripes induces lateral movement of Pt atoms and a displacement of the corrugation maximum of the stripes along the scanning direction. The displacement stems from the weakened interaction of surface Pt atoms to bulk Pt, because of the bonding of the topmost Pt layer to adsorbates. Under 1 Torr of 1:1 C_2H_4-H_2 mixture, the adsorbates move fast enough such that no features can be discerned at 60 nm/s, whereas short bright stripes are resolved at a higher scan rate (150 nm/s). Adding 3 mTorr of CO into the C_2H_4-H_2 mixture suppresses the adsorbate mobility and lifts the reconstruction on Pt(100). Reaction studies have revealed that the mobile surface without CO is active, whereas the immobile surface upon CO addition is deactivated in ethylene hydrogenation.

6.5 References

(1) Hagstrom, S.; Lyon, H. B.; Somorjai, G. A. *Phys. Rev. Lett.* **1965**, *15*, 491-493.

(2) Heilmann, P.; Heinz, K.; Müller, K. *Surf. Sci.* **1979**, *83*, 487-497.

(3) Heinz, K.; Lang, E.; Strauss, K.; Müller, K. *Surf. Sci. Lett.* **1982**, *120*, L401-L404.

(4) Heinz, K.; Lang, E.; Strauss, K.; Müller, K. *Appl. Surf. Sci.* **1982**, *11/12*, 611-624.

(5) Van Hove, M. A.; Koestner, R. J.; Stair, P. C.; Bibérian, J. P.; Kesmodel, L. L.; BartoŠ, I.; Somorjai, G. A. *Surf. Sci.* **1981**, *103*, 189-217.

(6) Fiorentini, V.; Methfessel, M.; Scheffler, M. *Phys. Rev. Lett.* **1993**, *71*, 1051-1054.

(7) Norton, P. R.; Da Vies, J. A.; Creber, D. K.; Sitter, C. W.; Jackman, T. E. *Surf. Sci.* **1981**, *108*, 205-224.

(8) Behm, R. J.; Thiel, P. A.; Norton, P. R.; Ertl, G. *J. Chem. Phys.* **1983**, *78*, 7437-7447.

(9) Thiel, P. A.; Behm, R. J.; Norton, P. R.; Ertl, G. *J. Chem. Phys.* **1983**, *78*, 7448-7458.

(10) Tao, F.; Dag, S.; Wang, L. W.; Liu, Z.; Butcher, D. R.; Salmeron, M.; Somorjai, G. A. *Nano Lett.* **2009**, *9*, 2167-2171.

(11) Butcher, D. R. Ph.D. Dissertation, University of California, Berkeley, 2010.

(12) Martin, R.; Gardner, P.; Bradshaw, A. M. *Surf. Sci.* **1995**, *342*, 69-84.

(13) Ritter, E.; Behm, R. J.; Pötschke, G.; Wintterlin, J. *Surf. Sci.* **1987**, *181*, 403-411.

(14) Borg, A.; Hilmen, A. M.; Bergene, E. *Surf. Sci.* **1994**, *306*, 10-20.

(15) Griffiths, K.; Jackman, T. E.; Davies, J. A.; Norton, P. R. *Surf. Sci.* **1984**, *138*, 113-124.

(16) Norton, P. R.; Griffiths, K.; Bindner, P. E. *Surf. Sci.* **1984**, *138*, 125-147.

(17) Bonzel, H. P.; Brodén, G.; Pirug, G. *J. Catal.* **1978**, *53*, 96-105.

(18) Mase, K.; Murata, Y. *Surf. Sci.* **1992**, *277*, 97-108.

(19) Somorjai, G. A.; Li, Y. *Introduction to Surface Chemistry and Catalysis*; 2nd ed.; Johns Wiley & Sons, Inc.: Hoboken, NJ, 2010.

(20) Bond, G. C. *Chem. Soc. Rev.* **1991**, *20*, 441-475.

(21) Somorjai, G. A.; Roberts, M. W.; Thomas, J. M.; Sheppard, N. *Philos. Trans. R. Soc. London, A* **1986**, *318*, 81-100.

(22) Zaera, F.; Somorjai, G. A. *J. Am. Chem. Soc.* **1984**, *106*, 2288-2293.

(23) Hatzikos, G. H.; Masel, R. I. *Surf. Sci.* **1987**, *185*, 479-494.

(24) McCrea, K. R.; Somorjai, G. A. *J. Mol. Catal. A: Chem.* **2000**, *163*, 43-53.

(25) Fischer, T. E.; Kelemen, S. R. *Surf. Sci.* **1977**, *69*, 485-507.

(26) Morgan, A. E.; Somorjai, G. A. *Surf. Sci.* **1968**, *12*, 405-425.

(27) Rønning, M.; Bergene, E.; Borg, A.; Ausen, S.; Holmen, A. *Surf. Sci.* **2001**, *477*, 191-197.

(28) Tao, F.; Dag, S.; Wang, L. W.; Liu, Z.; Butcher, D. R.; Bluhm, H.; Salmeron, M.; Somorjai, G. A. *Science* **2010**, *327*, 850-853.

(29) Hendriksen, B. L. M.; Frenken, J. W. M. *Phys. Rev. Lett.* **2002**, *89*, 046101.

(30) Longwitz, S. R.; Schnadt, J.; Vestergaard, E. K.; Vang, R. T.; Laegsgaard, E.; Stensgaard, I.; Brune, H.; Besenbacher, F. *J. Phys. Chem. B* **2004**, *108*, 14497-14502.

(31) Österlund, L.; Rasmussen, P. B.; Thostrup, P.; Lægsgaard, E.; Stensgaard, I.;

Besenbacher, F. *Phys. Rev. Lett.* **2001**, *86*, 460-463.

(32) Butcher, D. R.; Grass, M. E.; Zeng, Z.; Aksoy, F.; Bluhm, H.; Li, W.-X.; Mun, B. S.; Somorjai, G. A.; Liu, Z. *J. Am. Chem. Soc.* **2011**, *133*, 20319.

(33) Zhu, Z.; Tao, F.; Zheng, F.; Chang, R.; Li, Y.; Heinke, L.; Liu, Z.; Salmeron, M.; Somorjai, G. A. *Nano Lett.* **2012**, *12*, 1491-1497.

(34) Vestergaard, E. K.; Vang, R. T.; Knudsen, J.; Pedersen, T. M.; An, T.; Lægsgaard, E.; Stensgaard, I.; Hammer, B.; Besenbacher, F. *Phys. Rev. Lett.* **2005**, *95*, 126101.

(35) Montano, M.; Bratlie, K. M.; Salmeron, M.; Somorjai, G. A. *J. Am. Chem. Soc.* **2006**, *128*, 13229-13234.

(36) Montano, M.; Salmeron, M.; Somorjai, G. A. *Surf. Sci.* **2006**, *600*, 1809-1816.

(37) Tang, D. C.; Hwang, K. S.; Salmeron, M.; Somorjai, G. A. *J. Phys. Chem. B* **2004**, *108*, 13300-13306.

(38) Tao, F.; Tang, D. C.; Salmeron, M.; Somorjai, G. A. *Rev. Sci. Instrum.* **2008**, *79*, 084101.

(39) Klein, M.; Schwitzgebel, G. *Rev. Sci. Instrum.* **1997**, *68*, 3099-3103.

(40) Aksoy, F.; Grass, M. E.; Joo, S. H.; Jabeen, N.; Hong, Y. P.; Hussain, Z.; Mun, B. S.; Liu, Z. *Nucl. Instrum. Methods Phys. Res., Sect. A* **2011**, *645*, 260-265.

(41) Grass, M. E.; Karlsson, P. G.; Aksoy, F.; Lundqvist, M.; Wannberg, B.; Mun, B. S.; Hussain, Z.; Liu, Z. *Rev. Sci. Instrum.* **2010**, *81*, 053106.

(42) Powell, C. J.; Jablonski, A. *NIST Electron Inelastic Mean Free Path Database, version 1.2*; National Institute of Standards and Technology: Gaithersburg, MD, 2010.

(43) Mortensen, J. J.; Linderoth, T. R.; Jacobsen, K. W.; Lægsgaard, E.; Stensgaard, I.; Besenbacher, F. *Surf. Sci.* **1998**, *400*, 290-313.

(44) Land, T. A.; Michely, T.; Behm, R. J.; Hemminger, J. C.; Comsa, G. *J. Chem. Phys.* **1992**, *97*, 6774-6783.

(45) Nomikou, Z.; Van Hove, M. A.; Somorjai, G. A. *Langmuir* **1996**, *12*, 1251-1256.

(46) Bukhtiyarov, V. I.; Nizovskii, A. I.; Bluhm, H.; Hävecker, M.; Kleimenov, E.; Knop-Gericke, A.; Schlögl, R. *J. Catal.* **2006**, *238*, 260-269.

(47) Freyer, N.; Pirug, G.; Bonzel, H. P. *Surf. Sci.* **1983**, *126*, 487-494.

(48) Fuhrmann, T.; Kinne, M.; Tränkenschuh, B.; Papp, C.; Zhu, J. F.; Denecke, R.; Steinrück, H.-P. *New J. Phys.* **2005**, *7*, 107.

(49) Bonzel, H. P.; Pirug, G. *Surf. Sci.* **1977**, *62*, 45-60.

(50) Ainsworth, M. K.; McCoustra, M. R. S.; Chesters, M. A.; Sheppard, N.; De La Cruz, C. *Surf. Sci.* **1999**, *437*, 9-17.

(51) Chen, P.; Kung, K. Y.; Shen, Y. R.; Somorjai, G. A. *Surf. Sci.* **2001**, *494*, 289-297.

(52) Rioux, R. M.; Hoefelmeyer, J. D.; Grass, M.; Song, H.; Niesz, K.; Yang, P.; Somorjai, G. A. *Langmuir* **2007**, *24*, 198-207.

Chapter 7

Reconstruction of the Cu(557) Surface under High Pressures of Gases and Gas Mixtures

Abstract

This chapter investigates surface restructuring processes on Cu(557) induced by CO, H_2, C_2H_4, and O_2. The phenomena are compared with those observed on Pt(557) under similar conditions. Meandering steps are observed at 100 mTorr of CO, along with the doubling transition of terrace sizes. Increasing the CO pressure to 1 Torr substantially promotes Cu diffusion on Cu(557), giving rise to 23 nm wide terraces on average. Cu clusters are not formed until the CO pressure is enhanced to 12 Torr. The at least one order of magnitude higher pressure of CO required to create clusters on Cu(557) than on Pt(557) is due to the lower heat of adsorption of CO on Cu(557). Therefore the CO coverage on Cu(557) at 1 Torr is not sufficient to stabilize the low-coordinated Cu atoms at kink sites. Cu terraces become ~10 nm wide after evacuating from 1 to 10^{-8} Torr, suggesting a partially reversible process. H_2 causes step coalescence on Cu(557), yielding 5 nm wide terraces at 500 mTorr. The structure of the Cu(557) is dominated by CO after further introducing 500 mTorr of CO. Several clusters are observed under 500 mTorr of C_2H_4, whereas subsequent addition of 500 mTorr of CO does not alter the structure on Cu(557). At 1 Torr of O_2, thick layers of Cu oxide are formed, which are hard to observe because of the poor conductivity.

7.1 Introduction

In the previous four chapters, the surface restructuring processes on flat Pt(100)-hex as well as stepped Pt(557) and Pt(332) surfaces were investigated under a variety of reactive gases. At pressures in the Torr range, the Pt surface structure is typically distinct from the structure observed below 10^{-6} Torr. In addition, low-coordinated step sites can undergo extraordinary structural evolution that does not occur on terrace sites. In order to shed more light on unraveling the correlation between the catalyst surface structure under reaction conditions and the catalytic performances, these studies need to be extended to other transition metal surfaces and even bimetallic surfaces. Ni and Pd are potential candidates because of their similar valence electron configuration to Pt, since the three elements are all in the 10^{th} group in the periodic table. However, Ni readily reacts with CO to yield $Ni(CO)_4$ that could potentially damage the vacuum, by virtue of the high vapor pressure of $Ni(CO)_4$ at 298 K. On the other hand, Pd is not proper because Pd readily reacts with H_2 existing in the vacuum background and in other gases as impurities. Although palladium hydride is unlikely to form at such low H_2 partial pressures, surface palladium hydride has been observed on a few Pd crystal surfaces.[1-3] The existence of surface palladium hydride can bring extra uncertainties difficult to rule out in explaining the experimental results.

Cu has become an appropriate substrate for *in situ* structural studies, so as to directly compare the surface restructuring processes on two metals showing distinct activity, since the filled d-band renders Cu less active than Pt. Investigation of surface reconstruction on Cu surfaces, which is anticipated to differ from restructuring on Pt, can provide insight into comprehending the difference in activity. The adsorption structure as well as dynamics of CO on Cu(111) and its vicinal surfaces has been systematically investigated for several decades.[4-10] Consensus has been reached that CO chemisorbs on top of Cu atoms on Cu(111) at 0.33 ML, forming a $(\sqrt{3} \times \sqrt{3})R30^\circ$ adsorbate layer observed by both LEED and STM.[5-7] With the increase of CO coverage at 95 K, the CO layer passes an intermediate stage at 0.44 ML that shows a $(1.5 \times 1.5)R18^\circ$ structure, before ultimately reaching a (1.39×1.39) structure at 0.52 ML.[6] The precise adsorption model of the (1.39×1.39) structure is uncertain, because the top-to-bridge ratio of adsorbed CO molecules varies with the temperature at which CO is dosed. Bartels *et al.* have revealed a (4×4) super unit cell of the adlayer with 1:1 top-to-bridge CO ratio at saturation.[7] On the Cu(211) surface with (111) terraces and (100) steps, CO exclusively occupies the top sites on both terraces and steps at coverages up to 0.50 ML between 30 and 80 K.[9] However, at 0.67 ML, the saturated coverage on Cu(211), whether CO molecules form a top-bridge or a top-top arrangement is still open to discussion.[11]At such low temperatures, the Cu(211) surface does not reconstruct with the adsorption of CO.[12]

The oxidation of Cu single crystals by O_2 has also been under intensive studies.[13-17] When the Cu(111) surface is exposed to 10^{-7} Torr of O_2 at 298 K, step edges are firstly decorated with a rim of step oxide identified as Cu_2O according to atomically resolved

STM images.[13,16] Lower terraces at step edges are the nucleation sites for Cu_2O. Step oxide subsequently grows onto the flat upper terraces, leading to the formation of $Cu_2O(111)$. Lawton *et al.* has illustrated that the initial oxidation of vicinal Cu(111) surfaces only relies on the step density but not the step orientation.[18] Provided the existence of defect sites on the Cu(111) terrace, Cu_2O can also directly form on terraces. The boundary between $Cu_2O(111)$ and Cu(111) runs along the close-packed directions. In addition, the remaining Cu(111) terraces are all separated by (100) steps, even though some Cu steps were originally oriented along the (111) direction.

In this chapter, the structure of the Cu(557) surface was monitored under some gases and gas mixtures. CO could lead to the formation of 23 nm wide terraces at 1 Torr and the appearance of clusters at 12 Torr. Cu terraces become narrower upon CO evacuation from 1 to 10^{-8} Torr, although still wider than the clean Cu(557) surface in UHV. H_2 results in the formation of large terraces, but the terraces are only 5 nm wide under 500 mTorr of H_2, narrower than terraces under similar pressures of CO. Addition of 500 mTorr of CO when keeping the H_2 partial pressure at 500 mTorr causes the terraces to grow into 20 nm in size. 500 mTorr of C_2H_4 can induce the formation of Cu clusters, which do not change with the subsequent introduction 500 mTorr of CO. 1 Torr of O_2 strongly oxidizes the Cu(557) surface, forming thick Cu oxide layers that are difficult to observe under STM because of the low conductivity. Some Cu oxide islands can be seen after the evacuation of O_2.

7.2 Experimental Section

STM experiments were performed in the home-built HP-STM instrument as in earlier chapters.[19] The Cu(557) crystal was cleaned through repeated cycles of 800-eV Ar^+ bombardment at 3×10^{-5} Torr and annealing in vacuum at 873 K. After the last annealing, the crystal was cooled down to 298 K at a cooling rate of 1 K/sec. The absence of any impurities at surface before HP-STM measurements were examined by AES. All STM images were recorded at 298 K.

7.3 Results and Discussion

7.3.1 Clean Cu(557)

The STM images of the clean Cu(557) surface are displayed in Figure 7-1. Since copper is also in the fcc crystal structure, the model of Cu(557) is exactly the same as the model of Pt(557) in Figure 3-1a. Based on the copper atomic radius of 128 pm,[20] the average terrace width of the Cu(557) surface is calculated to be 1.4 nm. Figure 7-1a shows that the Cu steps are mostly straight in UHV except a few meandering steps in the bottom left corner. The average terrace width is 1.4 nm by measuring the distances between 20 steps, consistent with the calculated value. However, after zooming in as in Figure 7-1b, the STM image becomes more blurred with respect to the image of clean Pt(557) in Figure 3-1b. Cu terraces appear wider in the top part of Figure 7-1b because of high thermal drift at the

beginning of scans. Cu steps in the higher magnified STM image are frizzy for the sake of kink diffusion along the steps.[21] Cu atoms are highly mobile along the step direction since the diffusion barrier of Cu atoms along (100) steps on Cu(111) terraces is as low as 0.30 eV,[22] much smaller than 0.84 eV for Pt atoms to move along (100) steps on Pt(111) terraces.[23,24] Consequently, STM images of the clean (557) surface are blurred, because the movement of Cu atoms can be in a similar time scale as the tip scans.

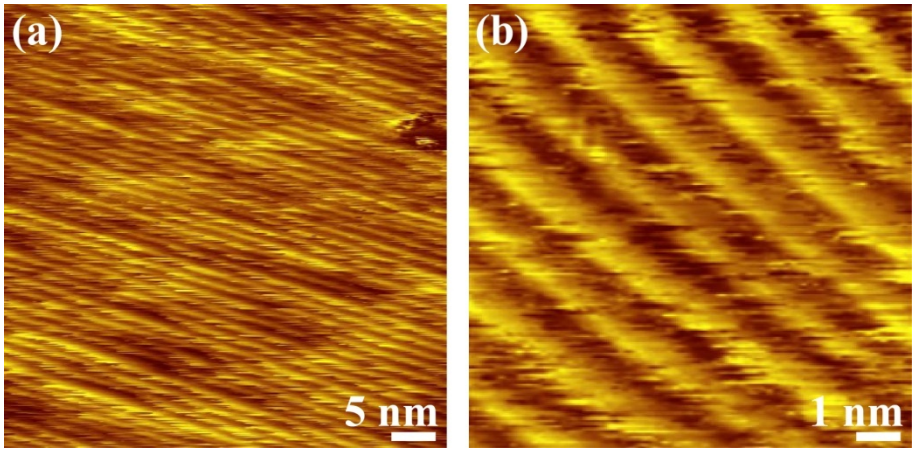

Figure 7-1. (a) Low and (b) high magnification STM images of the Cu(557) surface in UHV at a base pressure of 10^{-10} Torr. The steps are blurred owing to the high mobility of Cu atoms along the step direction at 298 K. (a) V_s = +1.5 V, I_t = 0.5 nA; (b) V_s = +50 mV, I_t = 1.0 nA.

7.3.2 CO on Cu(557)

The surface reconstruction on Cu(557) was firstly studied under CO, in order to compare with the dramatic formation of triangular clusters on Pt(557) at 1 Torr of CO.[25] Figure 7-2a shows that step meandering, along with several ~1 nm large islands, is observed under 100 mTorr of CO. In addition, the average terrace width has increased to 2.7 nm, evidencing a doubling transition of terrace widths and step heights. When the CO pressure is enhanced to 1 Torr, large Cu terraces with average widths of 23 nm have formed as a result of step coalescence, as in Figure 7-2b. Detailed surface structure is not resolvable on account of the high mobility of CO molecules on Cu surfaces even down to 40 K.[7] CO induces disparate surface reconstruction on Cu(557) and Pt(557) under the same pressure, which is mainly due to the different atomic mobility of Cu and Pt. Since the barrier for adatom diffusion on (111) terraces, the barrier for atom detaching from (100) steps, and the Ehrlich-Schwoebel barrier are all lower on Cu than on Pt,[22,24] Cu atoms can promptly move in a long distance on the Cu(557) surface to form large terraces with the adsorption of CO. In contrast, Pt atoms only move locally even at the stimulation of strong CO−CO repulsion, giving rise to kink sites and small clusters,.

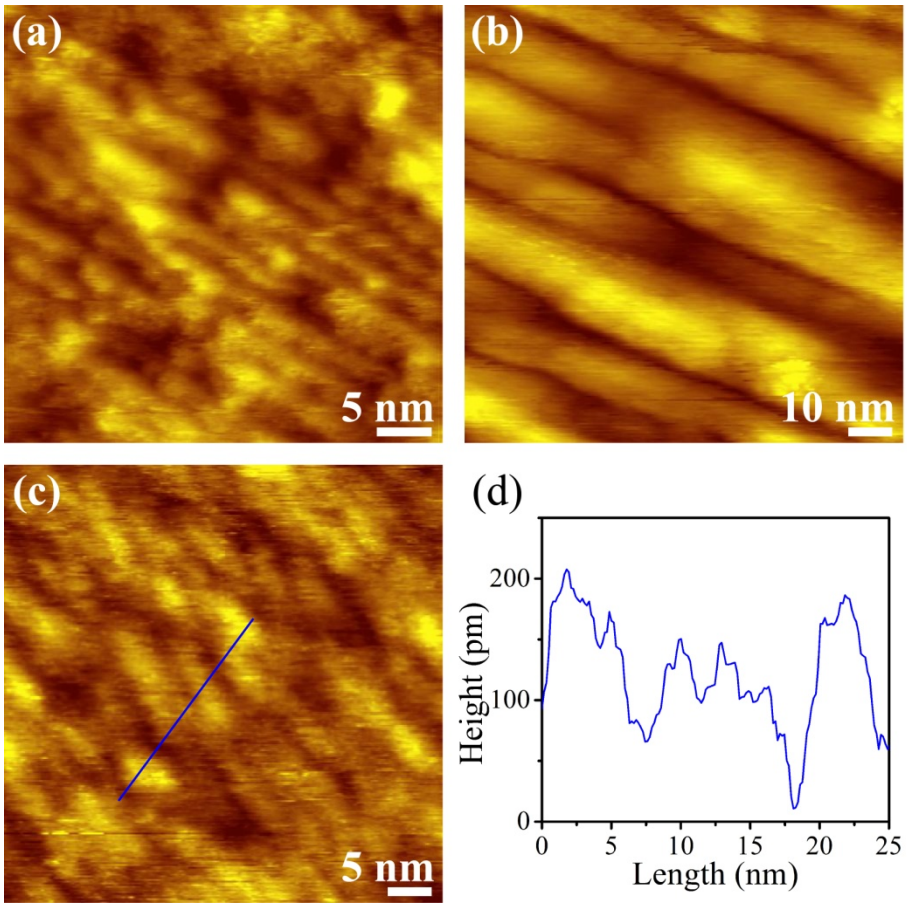

Figure 7-2. STM images of Cu(557) under (a) 100 mTorr, (b) 1 Torr, and (c) 12 Torr of CO. Cu steps become meandering upon introducing 100 mTorr of CO, and terrace widths as well as step heights are doubled. Under 1 Torr of CO, Cu terraces grow to 23 nm in width on average, but no clusters are observed. Cu clusters are formed when increasing the CO pressure to 12 Torr. (d) Line profile of the blue line in (c) showing that the clusters are 5 nm large. (a) V_s = -0.2 V, I_t = 0.1 nA; (b) V_s = +50 mV, I_t = 0.2 nA; (c) V_s = +0.1 V, I_t = 1.0 nA.

Furthermore, the lower CO coverage on Cu(557) than on Pt(557), resulted from the substantially lower CO heat of adsorption on Cu(557), can also account for the absence of Cu clusters under 1 Torr of CO, since the great number of kink sites at cluster edges need to be stabilized by sufficient adsorbate molecules. Although heat of adsorption has mainly been measured on (111) surfaces in literature, the values are important references for studies on (557) surfaces. On Cu(111), the CO heat of adsorption is 50 kJ/mol at 0 ML and 38 kJ/mol at 0.33 ML.[4] On Pt(111), the CO heat of adsorption is 180 kJ/mol at 0 ML, which decreases to 160 kJ/mol at 0.33 ML and 120 kJ/mol at 0.50 ML.[26] Moreover, CO completely desorbs on Cu(111) at 190 K in vacuum,[8] whereas the complete desorption of

CO on Pt(111) requires 560 K.[27] The substantially weaker adsorption of CO on Cu(111) suggests that the CO coverage on Cu(557) is lower than on Pt(557) at the same CO pressure. The amount of CO molecules on the Cu(557) surface at 1 Torr may thus not be large enough to stabilize clusters by bonding with Cu atoms at cluster edges, because numerous low-coordinated kink sites at cluster edges are energetically unfavorable without adsorbates. Ultimately, large Cu terraces are more stable owing to the small concentration of kink sites, which hence appear under 1 Torr of CO.

When higher pressures of CO that guarantees a higher CO coverage is introduced, the clusters indeed appear on Cu(557). Figure 7-2c shows some clusters are formed on Cu(557) under 12 Torr of CO, although the image quality is poor. Since the CO coverage on Cu(557) under 12 Torr is undoubtedly higher than the coverage under 1 Torr, Cu clusters can be stabilized by occupation of CO molecules at cluster edges. A line profile over several clusters in Figure 7-2d shows that the average cluster size is 5 nm. The low quality of the STM image is due to the quick attachment and detachment of CO molecules at the tip surface, in the sense that the $Pt_{0.8}Ir_{0.2}$ tip interacts with CO more strongly than the Cu(557) substrate. In addition, the highly mobile Cu atoms and CO molecules also render it difficult to image the Cu(557) surface structure at high CO pressures.

Figure 7-3 shows that, after evacuating CO from 1 to 10^{-8} Torr, terraces are still wide on Cu(557). Nevertheless, the average terrace size substantially decreases from 23 to 12 nm, suggesting that surface reconstruction on Cu(557) induced by CO is partially reversible. Evacuating CO from 12 to 10^{-8} Torr leads to similar phenomenon, though the STM image is not shown here owing to low image quality. The reversibility of the restructuring process on Cu(557) is similar to the observation on Pt(557), which could be due to the desorption of CO along with gas evacuation.

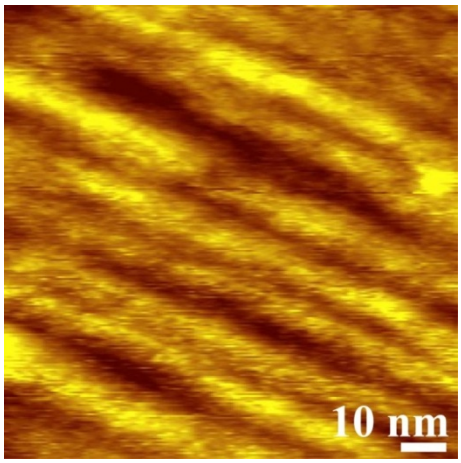

Figure 7-3. STM image of Cu(557) after evacuating CO from 1 to 10^{-8} Torr. The average width of Cu terraces decreases to 12 nm, suggesting a partially reversible restructuring process induced by CO. V_s = +0.1 V, I_t = 0.5 nA.

7.3.3 H_2 on Cu(557) and the Co-Adsorption with CO

The surface structure of Cu(557) under H_2 has also attracted considerable interest, since H_2 is the important product in the water-gas shift reaction in which Cu is a common catalyst. On Cu(110), H_2 results in the (1 × 2) missing row reconstruction at pressures greater than 2 mbar.[28] Here the effect of H_2 on the stepped Cu(557) surface structure was investigated. Figure 7-4a shows that step coalescence has occurred on part of the surface under 100 mTorr of H_2, forming several 5 nm wide terraces. The adsorption of hydrogen atoms motivates Cu atoms to diffuse along the steps. On the rest of the surface, the terrace width remains at 1.4 nm as the width on clean Cu(557). Since the same pressure of H_2 does not induce any reconstruction on Pt(557) as discussed in Chapter 4, the fact that Cu atoms are more mobile than Pt atoms can again account for the formation of large terraces. Upon increasing the H_2 pressure to 500 mTorr, almost all the 1.4 nm wide terraces grow into bigger terraces that are 6 nm wide on average, as in Figure 7-4b.

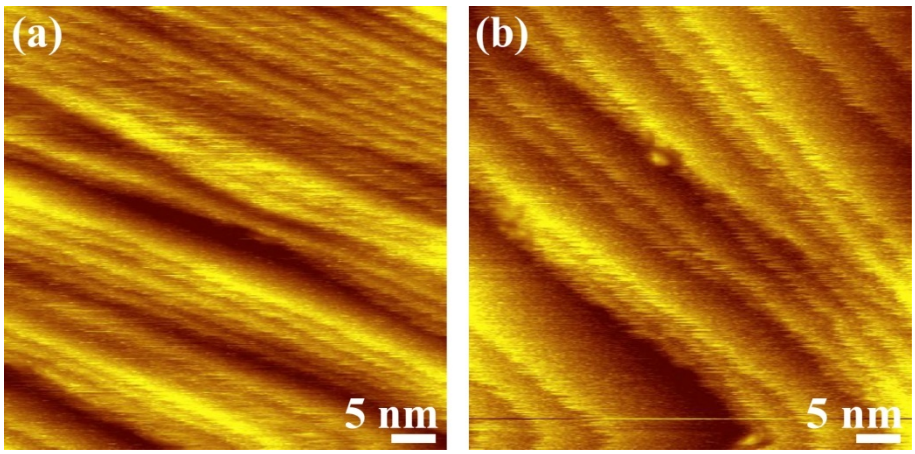

Figure 7-4. STM image of Cu(557) under (a) 100 mTorr and (b) 500 mTorr of H_2. Several terraces of 5 nm in width are observed under 100 mTorr of H_2. Step coalescence is observed on most of the Cu(557) surface with the increase of H_2 pressure to 500 mTorr. (a) V_s = -0.2 V, I_t = 0.2 nA; (b) V_s = +1.0 V, I_t = 0.5 nA.

500 mTorr of CO was subsequently dosed into the HP-STM cell while keeping the H_2 partial pressure at 500 mTorr. Figure 7-5 displays that Cu terraces become even wider with the addition of CO. The average width increases to 14 nm by measuring the distances between 10 steps in a (20 × 20) nm^2 STM image. CO appears to dominate the Cu(557) surface structure when co-adsorbing with H_2 at the same partial pressure ratio. Since the H_2 heat of adsorption on Cu(111) is 42 kJ/mol,[29] lower than the CO heat of adsorption, CO is capable of displacing some chemisorbed hydrogen atoms, giving rise to broader terraces. However, hydrogen atoms are still present on Cu(557), because H_2 does not completely

desorb from Cu(111) until 370 K and in the sense that hydrogen atoms can migrate into subsurface Cu sites.[30,31] Since the existence of hydrogen atoms can alter the adsorbate interaction, the strength of chemisorption, and Cu mobility, Cu terraces do not grow as wide as under pure CO. Similar to the images acquired under pure CO in Figure 7-2, the STM image also becomes frizzy upon the dosage of CO.

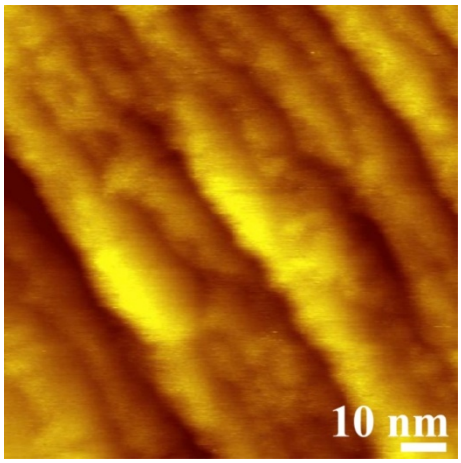

Figure 7-5. STM image of Cu(557) under 500 mTorr of H_2 and 500 mTorr of CO. CO was introduced after H_2. Terraces wider than 20 nm as a result of CO adsorption are observed, and the average terrace width increases to 14 nm. CO dominates the Cu(557) substrate structure over H_2. V_s = +0.2 V, I_t = 1.0 nA.

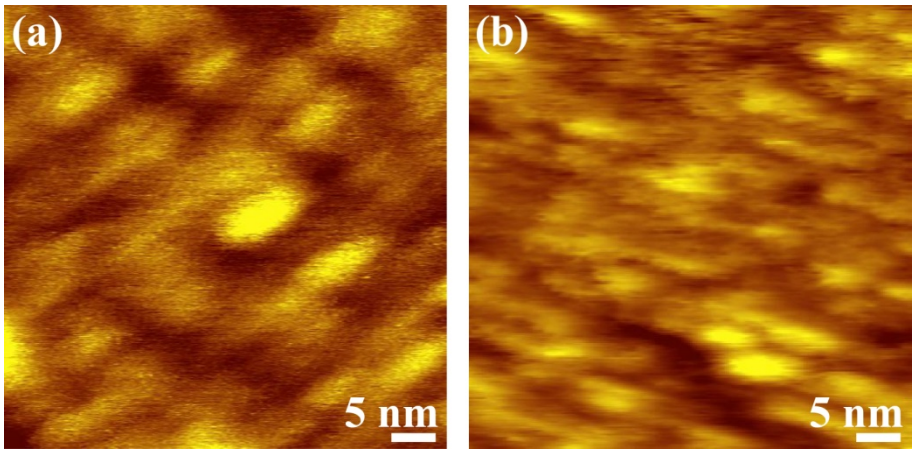

Figure 7-6. STM image of Cu(557) (a) under 500 mTorr of C_2H_4 and (b) after further adding 500 mTorr of CO. Bright Cu clusters can be observed under both cases although with poor resolution owing to high surface mobility. V_s = +0.2 V, I_t = 1.0 nA.

7.3.4 C_2H_4 on Cu(557) and the Co-Adsorption with CO

The structure of the Cu(557) surface in response to organic molecules such as C_2H_4 was also investigated. Figure 7-6a shows that, under 500 mTorr of C_2H_4, the STM image of Cu(557) is blurred, and a few round clusters of 5 nm in diameter are observed. Both experimental data and theoretical calculations illustrate that C_2H_4 binds to the Cu(111) terrace via π-adsorption, with the C−C bond lying parallel to the surface.[32-34] Since C_2H_4 weakly adsorbs on Cu(111) terraces as suggested by the desorption maximum at 120 K,[35] the chemisorbed C_2H_4 molecules may readily move with tip scans, leading to blurred STM images. The subsequent introduction of 500 mTorr of CO does not significantly alter the surface structure, as shown in Figure 7-6b. Surface mobility remains high and round clusters are still present. Terraces wider than 10 nm are absent, indicating that the incorporation of CO cannot fully remove the chemisorbed C_2H_4 molecules on Cu(557), even though C_2H_4 adsorption is significantly weaker.

7.3.5 O_2 on Cu(557)

Because O_2 can readily induce the formation of Cu_2O at step edges on Cu(111) vicinal surfaces, the oxidation of Cu(557) by high pressures of O_2 was studied. Figure 7-7a shows that no features can be clearly resolved under 1 Torr of O_2. Unlike the cases in previous chapters and in earlier sections where the inability to resolve the surface structure is due to the high surface mobility, here the low conductivity of the oxidized Cu(557) surface is the major cause of the featureless STM image. Bulk Cu_2O is a p-type semiconductor with a direct band gap of 2.2 eV.[36] Although monatomic Cu_2O layers can indeed be imaged at +0.2 V sample bias,[18] electronic conductivity substantially decreases as Cu_2O layers grow thicker. Even though further oxidation of Cu_2O into CuO may happen at 1 Torr of O_2, CuO is also a semiconductor with an indirect band gap of 1.2 eV.[37] The chemical composition of Cu oxide on Cu(557) needs to be investigated using spectroscopy techniques. Electrons hence cannot tunnel into the Cu(557) surface at +0.2 V sample bias. However, the structure of oxidized Cu(557) surface cannot be resolved under 1 Torr of O_2 even if the sample bias is enhanced to +3.0 eV, implying that the Cu oxide formed on Cu(557) is too thick for tunneling electrons to penetrate.

After O_2 is evacuated to 10^{-8} Torr, the oxidized Cu(557) surface can be roughly imaged by STM, as shown in Figure 7-7b. A great number of 5 nm wide islands are roughly aligned along the original step directions, and the terraces have appeared wider. Detailed structure of the oxidized Cu(557) surface is still hard to resolve regardless of the sample bias and the tunneling current. Cu_2O may be partially reduced by H_2 and CO in the background gases, leading to a thinner oxide layer that can be seen under STM. Studying the Cu(557) surface structure under CO-O_2 mixture or the H_2-O_2 mixture was also attempted, but featureless images were obtained under both gas conditions.

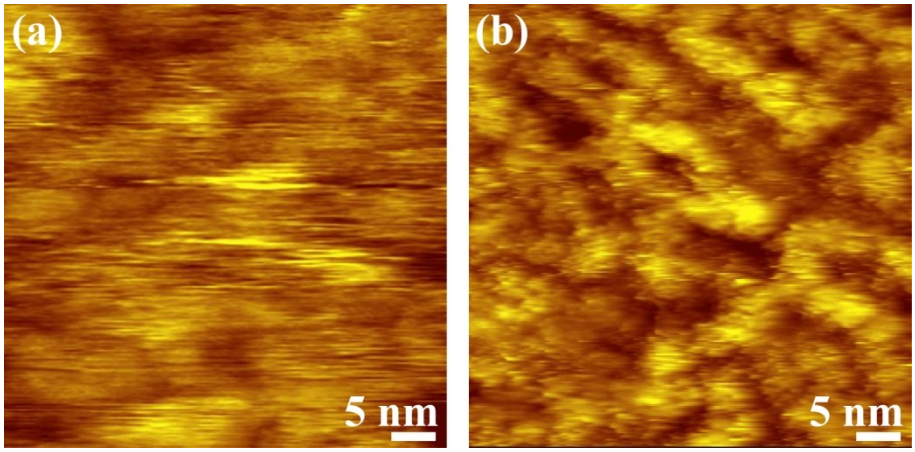

Figure 7-7. STM image of Cu(557) (a) under 1 Torr of O_2 and (b) after evacuating O_2 to 10^{-8} Torr. No features are resolved under 1 Torr of O_2 because O_2 can oxidize Cu, forming thick Cu_2O that is poorly conductive. Some clusters over 5 nm large can be roughly resolved upon evacuating the gas-phase O_2. V_s = +0.2 V, I_t = 1.0 nA.

7.4 Conclusions

In summary, the surface structure of Cu(557) was investigated under a variety of reactant gases such as CO, H_2, C_2H_4, and O_2, and the relevant gas mixtures. Meandering Cu steps appear under 100 mTorr of CO, with the doubling transition of terrace sizes. CO induces large terraces as wide as 23 nm on Cu(557) at 1 Torr, whereas the formation of Cu clusters requires higher CO pressure at 12 Torr. Detailed adsorbate structure on large terraces is not resolved because of the high surface mobility. Cu terraces become narrower upon CO evacuation but still wider than the terraces in UHV, implying the partial reversibility of the reconstruction induced by CO. H_2 causes step coalescence on Cu(557) as well, forming 5 nm wide terraces at 500 mTorr. C_2H_4 results in small clusters along with the slightly wider Cu terraces. Further introduction of 500 mTorr of CO into C_2H_4 does not change the Cu(557) surface structure, whereas CO dominates the surface structure while co-adsorbing with H_2. 1 Torr of O_2 strongly oxidizes Cu(557), leading to the formation of thick Cu oxide layers hardly discernible under STM owing to the low conductivity. Cu oxide islands can be roughly observed after evacuating O_2.

7.5 References

(1) Muschiol, U.; Schmidt, P. K.; Christmann, K. *Surf. Sci.* **1998**, *395*, 182-204.

(2) Okuyama, H.; Siga, W.; Takagi, N.; Nishijima, M.; Aruga, T. *Surf. Sci.* **1998**, *401*, 344-354.

(3) Gdowski, G. E.; Felter, T. E.; Stulen, R. H. *Surf. Sci. Lett.* **1987**, *181*, L147-L155.

(4) Hollins, P.; Pritchard, J. *Surf. Sci.* **1979**, *89*, 486-495.

(5) Hollins, P.; Pritchard, J. *Surf. Sci.* **1980**, *99*, L389-L394.

(6) Raval, R.; Parker, S. F.; Pemble, M. E.; Hollins, P.; Pritchard, J.; Chesters, M. A. *Surf. Sci.* **1988**, *203*, 353-377.

(7) Bartels, L.; Meyer, G.; Rieder, K. H. *Surf. Sci.* **1999**, *432*, L621-L626.

(8) Kirstein, W.; Krüger, B.; Thieme, F. *Surf. Sci.* **1986**, *176*, 505-529.

(9) Gajdoš, M.; Eichler, A.; Hafner, J.; Meyer, G.; Rieder, K.-H. *Phys. Rev. B* **2005**, *71*, 035402.

(10) Shinn, N. D.; Trenary, M.; McClellan, M. R.; McFeely, F. R. *J. Chem. Phys.* **1981**, *75*, 3142-3150.

(11) Zöphel, S.; Repp, J.; Meyer, G.; Rieder, K. H. *Chem. Phys. Lett.* **1999**, *310*, 145-149.

(12) Meyer, G.; Neu, B.; Rieder, K. H. *Chem. Phys. Lett.* **1999**, *240*, 379-384.

(13) Matsumoto, T.; Bennett, R. A.; Stone, P.; Yamada, T.; Domen, K.; Bowker, M. *Surf. Sci.* **2001**, *471*, 225-245.

(14) Spitzer, A.; Lüth, H. *Surf. Sci.* **1982**, *118*, 136-144.

(15) Vollmer, S.; Birkner, A.; Lukas, S.; Witte, G.; Woll, C. *Appl. Phys. Lett.* **2000**, *76*, 2686-2688.

(16) Wiame, F.; Maurice, V.; Marcus, P. *Surf. Sci.* **2007**, *601*, 1193-1204.

(17) Xu, Y.; Mavrikakis, M. *Surf. Sci.* **2003**, *538*, 219-232.

(18) Lawton, T. J.; Pushkarev, V.; Broitman, E.; Reinicker, A.; Sykes, E. C. H.; Gellman, A. J. *J. Phys. Chem. C* **2012**, *116*, 16054-16062.

(19) Tao, F.; Tang, D. C.; Salmeron, M.; Somorjai, G. A. *Rev. Sci. Instrum.* **2008**, *79*, 084101.

(20) Dean, J. A. *Lange's Handbook of Chemistry*; 15th ed.; McGraw-Hill Professional, 1998.

(21) Giesen-Scibert, M.; Ibach, H. *Surf. Sci.* **1994**, *316*, 205-222.

(22) Wang, J.; Huang, H.; Timothy, S. C. *Modell. Simul. Mater. Sci. Eng.* **2004**, *12*, 1209.

(23) Feibelman, P. J. *Phys. Rev. B* **1999**, *60*, 4972-4981.

(24) Jacobsen, J.; Jacobsen, K. W.; Stoltze, P.; Nørskov, J. K. *Phys. Rev. Lett.* **1995**, *74*, 2295-2298.

(25) Tao, F.; Dag, S.; Wang, L. W.; Liu, Z.; Butcher, D. R.; Bluhm, H.; Salmeron, M.; Somorjai, G. A. *Science* **2010**, *327*, 850-853.

(26) Yeo, Y. Y.; Vattuone, L.; King, D. A. *J. Chem. Phys.* **1997**, *106*, 392-401.

(27) Ertl, G.; Neumann, M.; Streit, K. M. *Surf. Sci.* **1977**, *64*, 393-410.

(28) Österlund, L.; Rasmussen, P. B.; Thostrup, P.; Lægsgaard, E.; Stensgaard, I.; Besenbacher, F. *Phys. Rev. Lett.* **2001**, *86*, 460-463.

(29) Comsa, G.; David, R. *Surf. Sci.* **1982**, *117*, 77-84.

(30) Anger, G.; Winkler, A.; Rendulic, K. D. *Surf. Sci.* **1989**, *220*, 1-17.

(31) Mudiyanselage, K.; Yang, Y.; Hoffmann, F. M.; Furlong, O. J.; Hrbek, J.; White,

M. G.; Liu, P.; Stacchiola, D. J. *J. Chem. Phys.* **2013**, *139*, 044712-044718.

(32) Fuhrmann, D.; Wacker, D.; Weiss, K.; Hermann, K.; Witko, M.; Woll, C. *J. Chem. Phys.* **1998**, *108*, 2651-2658.

(33) Michalak, A.; Witko, M.; Hermann, K. *J. Mol. Catal. A: Chem.* **1997**, *119*, 213-221.

(34) Watson, G. W.; Wells, R. P. K.; Willock, D. J.; Hutchings, G. J. *Surf. Sci.* **2000**, *459*, 93-103.

(35) Linke, R.; Becker, C.; Pelster, T.; Tanemura, M.; Wandelt, K. *Surf. Sci.* **1997**, *377-379*, 655-658.

(36) Scanlon, D. O.; Morgan, B. J.; Watson, G. W. *J. Chem. Phys.* **2009**, *131*, 124703-124708.

(37) Rakhshani, A. E. *Solid-State Electron.* **1986**, *29*, 7-17.

Chapter 8

Evolution of Surface Chemistry of Platinum-Based Bimetallic Nanoparticles Driven by Changes in Gas Conditions

(This chapter covers similar materials as Wang, H.; Krier, J. M.; Zhu, Z. *et al. ACS Catal.* **2013**, *3*, 2371-2375 – reproduced with permission, copyright 2013 American Chemical Society; and Chen, C.; Huo, Z.; Zhu, Z. *et al.* in preparation.)

Abstract

This chapter concentrates on investigating the surface chemistry of Pt-based bimetallic nanoparticle catalysts under high pressures of gases and gas mixtures using AP-XPS. In 2 nm PtFe nanoparticles, Fe atoms at ~0.7 nm IMFP can be partially reduced by the C_2H_4-H_2 mixture and oxidized by O_2 at around 100 mTorr at 298 K. In contrast, the oxidation state of surface Pt atoms does not change with gas conditions. Pt_9Co-Co core-shell nanoparticles are stable under H_2 even when heated to 673 K, without the occurrence of any significant surface segregation or surface reduction. $PtNi_3$ polyhedra and Pt_3Ni frameworks, in which Ni is more enriched at the surface than in the bulk, can undergo reversible changes in surface composition while switching the gas environment between H_2 and O_2 at 100 mTorr at 393 K. Ni migrates to the surface in the presence of O_2, whereas Pt segregates to surface in the existence of H_2.

8.1 Introduction

Bimetallic systems have attracted considerable attention thanks to their superior catalytic properties to monometallic counterparts.[1-10] Addition of a second metal opens enormous possibilities to modify surface electronic structure and adsorption sites, which leads to rational design of novel catalysts exhibiting high activity, selectivity and stability.[11-13] The bimetallic systems usually show enhanced activity and selectivity in catalytic applications comparing with the linear combination of pure metals, which is largely referred to as synergistic effect.[14] One possible root of the synergistic effect is that preferential bonding of each metal to each reactant strongly promotes the turnover rate, if the reactions undergo through Langmuir-Hinshelwood mechanism, such as Rh splitting O_2 and Pd appealing CO in CO oxidation on RhPd.[15] Another explanation involves the modification of surface electronic structure, for example the decreased d-band center on $Pt_3Ni(111)$ resulted from a pure Pt skin layer along with a Ni-rich second layer underneath.[3] This d-band downshift is also observed in alloys of Pt and other 3d transition metals,[13] which is responsible for the enhancement of activity in oxygen reduction reaction in fuel cells. In addition, some new structure ensembles may form under reaction conditions, accelerating catalytic reactions. On the PtFe and PtNi systems, Fe and Ni form oxide under the reaction mixture. The ensemble of vacancy sites on the oxide and neighboring metal atoms leads to higher activity in CO oxidation than pure Pt.[5,14]

Catalytic performances of bimetallic nanoparticles rely on a variety of factors such as size, morphology, and composition. For example, monodispersed Pt_3Ni nanoctahedra exposing {111} facets are five times more active than Pt_3Ni nanocubes terminated with {100} facets in oxygen reduction reaction.[16,17] Such results of Pt_3Ni nanocrystals accord with results of single crystal studies in which $Pt_3Ni(111)$ exhibits higher activity than $Pt_3Ni(100)$.[3] On $Rh_{1-x}Pd_x$ nanoparticles, the turnover frequency under 100 Torr of O_2 and 40 Torr of CO displays a typical volcano curve at both 453 and 463 K.[18] The activity first increases with the atomic fraction of Pd until the Pd fraction reaches 0.4, and subsequently declines with higher composition of Pd. Interactions between Rh and Pd atoms, along with the preferential bonding towards O_2 and CO, are responsible for the synergistic behaviors. Similarly, the atomic ratio in Pt−Ni and Pt−Co catalysts affects not only the activity of ethylene glycol in the aqueous phase, but also the selectivity between H_2 and alkanes.[19]

The surface chemical potential of each metal typically differs from the bulk chemical potential, because the surface free energy term should be taken into account.[1,20] As a result, most bimetallic systems exhibit a surface-to-bulk concentration gradient.[21-23] In addition, during reactions, bimetallic nanoparticle surfaces may undergo restructuring processes, leading to changes in composition and chemical states.[18,21-26] AP-XPS has long been a powerful technique to investigate surface segregation effect induced by chemical environment changes.[27,28] Our group have revealed that Rh in the Rh_xPt_{1-x} and Rh_xPd_{1-x} nanoparticles tends to diffuse to the surface above 523 K under oxidizing conditions

whereas Pd and Pt prefer to occupy the surface under reducing environments.[21,22] Similarly, while AuPd is used in CO oxidation, Pd segregation to surface is enhanced by increasing CO partial pressures. The Pd segregation is accompanied by oxidation or reduction of the metal components. Such versatility that the atomic ratio at surfaces may be subject to change during reactions poses great challenges to deeply understand reaction mechanisms and further optimize the catalysts.

In this chapter, Pt-based bimetallic nanoparticles synthesized using colloidal methods were investigated by AP-XPS under real conditions. In 2 nm PtFe nanoparticles which are active in ethylene hydrogenation at 298 K, surface Fe atoms become more reduced under the reaction mixture and oxidized under pure O_2. In contrast, the oxidation state of Pt does not vary with gas environments. Pt_9Co-Co core-shell nanoparticles with a 1~3 nm thick Co shell are stable under H_2 even at 673 K. Finally, as for the Pt−Ni system, the atomic fraction of Ni is higher at surface than in the bulk for as-synthesized $PtNi_3$ polyhedra and Pt_3Ni frameworks. At 373 K, Ni segregates to surface under O_2 in both samples because Ni is more susceptible toward oxidation by O_2, whereas H_2 drives Pt to the surface since the surface energy of Pt is lower.

8.2 Experimental Section

PtFe nanoparticles were synthesized through reduction of $Pt(acac)_2$ and $Fe(acac)_2$ by polyvinylpyrrolidone (PVP) in ethylene glycol. A total of 0.1 mmol of $Pt(acac)_2$ and 0.1 mmol of $Fe(acac)_2$ were dissolved into 5 mL of ethylene glycol together with 55 mg of PVP (M_w = 55,000). The solution was heated to 473 K in an oil bath for 5 min under Ar. After cooling the solution to 298 K, 45 mL of acetone were added into the reaction mixture to form a suspension. PtFe nanoparticles were separated by centrifugation and re-dispersed in 10 mL of ethanol. The nanoparticles were further washed by cycles of precipitation with hexane, centrifugation, and re-dispersion in ethanol. Samples for AP-XPS measurements were prepared by depositing Langmuir-Blodgett (LB) films of nanoparticles onto Si wafer substrate.

As for the preparation of Pt_9Co-Co core-shell nanoparticles, 8 mg of $Pt(acac)_2$ were dissolved into 9 mL of oleylamine in a three-necked flask, which was heated to 393 K under Ar flow. $Co(acac)_2$ solution, prepared by dissolving 30 mg of $Co(acac)_2$ into 1 mL of oleylamine in a glove box, was slowly added into the three-necked flask. The solution mixture was heated to 493 K at a rate of 5 K/min and kept at 493 K for 50 min. Pt_9Co-Co core shell nanoparticles were separated from the solution by centrifugation after cooling to 298 K and washed by cyclohexane. Samples for AP-XPS experiments were prepared via dropcasting monodispersed solution on Si wafers and washing by dimethylformamide (DMF), ethanol and cyclohexane for ten cycles to remove the oleylamine surfactant.

In the preparation of Pt−Ni bimetallic catalysts, 20 mg of $H_2PtCl_6 \cdot 6H_2O$ and 17.5 mg of $Ni(NO_3)_2 \cdot 6H_2O$ were dissolved in 0.4 mL deionized water. The solution was added into 10

mL oleylamine in a three-necked flask and heated to 433 K for 2 min to remove water, before being further heated up to 543 K under Ar. 3 min after the solution turns black, the reaction mixture was rapidly cooled down to 298 K in a water bath in order to stop the reaction. The $PtNi_3$ polyhedra were subsequently separated by centrifugation. As for the synthesis of Pt_3Ni frameworks, 3 mg of $PtNi_3$ polyhedra were re-dispersed in 5 mL of chloroform and 0.1 mL of oleylamine, which was later diluted with 10 mL of hexadecane. Pt_3Ni frameworks were acquired by heating the solution to 398 K for 12 h in air and separated by centrifugation. Both $PtNi_3$ and Pt_3Ni samples for XPS measurements were prepared via dropcasting monodisopersed solution on Si wafers. Oleylamine was washed away with cycles of DMF, ethanol and cyclohexane.

AP-XPS experiments were carried out on the Scienta 4000 HiPP workstation at Beamline 9.3.2 at ALS.[29] H_2 and O_2 gas lines are separately connected to the XPS chamber through molecular leak valves. Samples were mounted on a 1 cm sample holder with a ceramic button heater and a type-K thermocouple underneath. Because the binding energies of Pt 4f, Fe 3p, Co 3p, and Ni 3p core levels are similar, the IMFPs of photoelectrons emitted from the four core levels are nearly the same, when using the same photon energies of incident X-ray. Pt 4f, Fe 3p, Co 3p, and Ni 3p core level spectra were acquired with incident energies of 370 eV, 490 eV and 750 eV to generate photoelectrons with IMFPs of ~0.7, ~0.9, and ~1.2 nm, respectively.[30] All series of XPS spectra were quantitatively analyzed via peak deconvolution, preceded by subtracting the Shirley-type background.[31] Atomic fractions at surfaces were estimated using relative sensitive factors of Pt, Fe, Co, and Ni at different X-ray energies. The binding energy was calibrated by Si 2p peak at 99.3 eV and Fermi level at 0 eV recorded under the same conditions.

8.3 Results and Discussion

8.3.1 PtFe Nanoparticles

Figure 8-1 shows the transmission electron microscopy (TEM) and high-resolution TEM images of as-synthesized PtFe nanoparticles. The average diameter of PtFe nanoparticles is measured as 2 nm from the size of over 200 particles. The d-spacing of 0.22 nm between {111} facets in the high-resolution TEM image suggests the fcc lattice of the particles. Pt and Fe atoms are randomly arranged in the nanoparticles, which indicates the disordered phase of PtFe nanoparticles. Although ordered intermetallic PtFe alloy could be obtained, high temperature annealing was demanded.[7,32]

The composition and oxidation states at different depths on the as-synthesized 2 nm PtFe nanoparticle surface can be explored by tuning the incident energy of X-ray beams, because the IMFPs of electrons in metal vary with the kinetic energy that linearly increases with incident energy. Deconvolution of Pt 4f and Fe 3p spectra provides the oxidation state distribution of the two elements. Figure 8-2a shows that Fe atoms at the particle surface are more oxidized than in the bulk. At ~0.7 nm IMFP, ~38% of Fe is in metallic state, ~32% in

Fe^{2+}, and ~30% in Fe^{3+}. When the IMFP increases to ~0.9 and ~1.2 nm, the percentage of metallic Fe in total Fe rises to ~43% and ~50%, respectively, at the expense of Fe^{3+} that decreases to ~24% and ~15%. The percentage of Fe^{2+}, which is generally considered as reduced species, slightly increases to ~33% and ~35%. In contrast, the oxidation of Pt does not change with IMFP, with ~10% of the total Pt staying at Pt^{2+} at all IMFPs, as shown in Figure 8-2b.

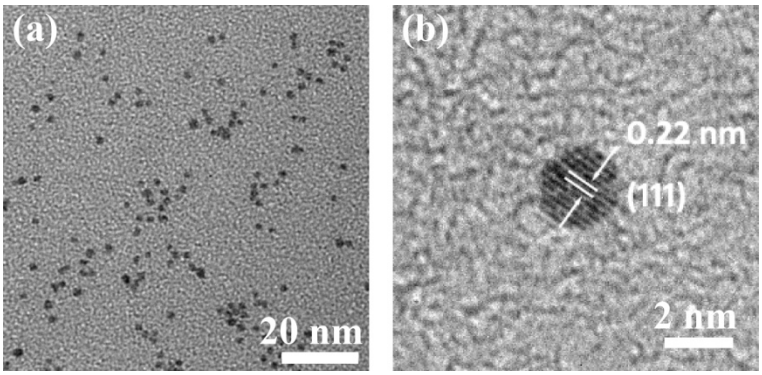

Figure 8-1. (a) TEM and (b) High-resolution TEM images of 2 nm PtFe nanoparticles. The as-synthesized particles are in the fcc crystal structure.

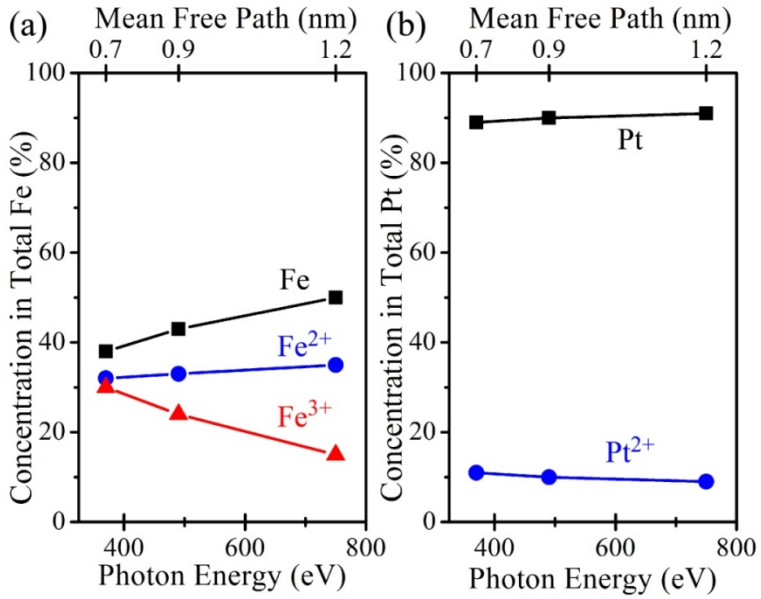

Figure 8-2. Oxidation state distributions of (a) Fe and (b) Pt in 2 nm PtFe nanoparticles as a function of photoelectron IMFPs. The percentage of Fe^{3+} in total Fe significantly decreases with IMFPs, whereas the percentage of metallic Fe increases in the meantime, indicating that surface Fe atoms are more oxidized than bulk Fe atoms. The oxidation state of Pt does not vary with IMFPs.

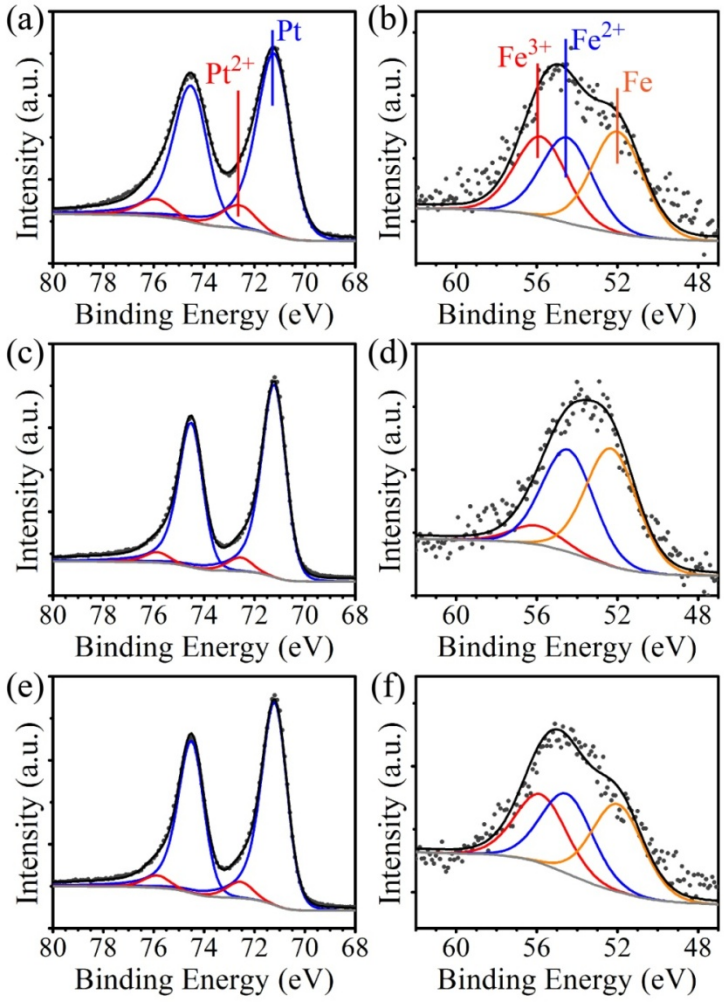

Figure 8-3. (left) Pt 4f and (right) Fe 3p spectra of 2 nm PtFe nanoparticles acquired with 370 eV incident energy at 298 K (a,b) in UHV, (c,d) under the mixture of 10 mTorr of C_2H_4 and 100 mTorr of H_2, and (e,f) under 100 mTorr of O_2. Pt remains mostly reduced under all three conditions, whereas the relative concentration of Fe, Fe^{2+} and Fe^{3+} varies with gas environments.

The surface chemistry of the 2 nm PtFe nanoparticles was monitored under the ethylene hydrogenation reaction mixture and oxygen with 370 eV incident energy at 298 K. Figure 8-3 shows the Pt 4f and Fe 3p spectra recorded in UHV, under the mixture of 100 mTorr of C_2H_4 and 10 mTorr of H_2, and under 100 mTorr of O_2 at 298 K. The Pt $4f_{7/2}$ peaks of metallic Pt and Pt^{2+} are located at 71.2 and 72.7 eV.[33-35] Fe 3p spectra are deconvoluted into three components at 52.1, 54.5, and 55.8 eV, corresponding to metallic Fe, Fe^{2+}, and Fe^{3+}, respectively.[36-38] Changes in the gas environments lead to obvious changes in the shape of Fe 3p spectra but not in Pt 4f spectra. Figure 8-4a displays that surface Fe atoms are

partially reduced under the ethylene hydrogenation mixture and oxidized under O_2. Initially in UHV, surface Fe atoms are comprised of ~38% of metallic Fe, ~32% of Fe^{2+}, and ~30% of Fe^{3+}. Upon introducing C_2H_4 and H_2, the percentage of metallic Fe and Fe^{2+} increases to ~49% and ~43%, respectively, whereas the percentage of Fe^{3+} largely drops to ~8%. The reduction of Fe could be due to the spillover of hydrogen atoms from the co-existing Pt atoms.[39-41] After evacuating the C_2H_4-H_2 mixture and introducing O_2, the percentage of metallic Fe and Fe^{2+} decreases to ~37% and ~34%, indicating the partial oxidation of surface Fe atoms back to the oxidation state distribution in UHV. The percentage of Fe^{3+} rises to ~29% in the meantime. On the other hand, Figure 8-4b illustrates that the oxidation state of Pt changes with gas conditions to a less extent as compared to Fe oxidation state. Surface Pt atoms are comprised of 90~93% of metallic Pt and 7~10% of Pt^{2+} under all three environments.

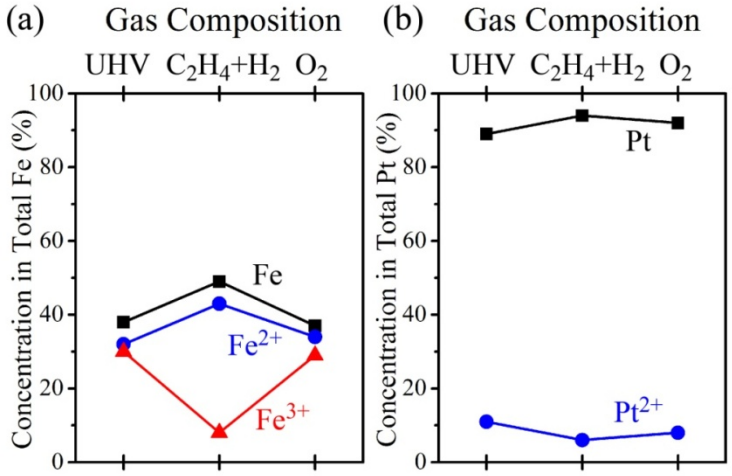

Figure 8-4. Changes in oxidation states of (a) Fe and (b) Pt in 2 nm PtFe nanoparticles with gas atmospheres at ~0.7 nm IMFP at 298 K. Fe is partially reduced under the ethylene hydrogenation reaction mixture and oxidized under O_2. In contrast, the oxidation state of Pt does not vary with gas reactants at 298 K.

Despite the significant changes in Fe oxidation states while varying gas conditions, the relative intensity ratio of Pt 4f peaks to Fe 3p peaks seems to remain the same in the spectra in Figure 8-3. The atomic fraction of Fe is estimated through the integrated area of Pt 4f and Fe 3p peaks and their respective atomic sensitivities. Figure 8-5 shows that the PtFe surface contains 34~37% of Fe regardless of gas environments at all three photoelectron IMFPs. The weak dependence of surface elemental composition on gas conditions is due to the low experimental temperature of 298 K that is not high enough for atoms to segregate between surface and bulk.[22] In addition, the similar Fe atomic fractions at all three IMFPs indicate that the 2 nm PtFe nanoparticles are homogeneously distributed.

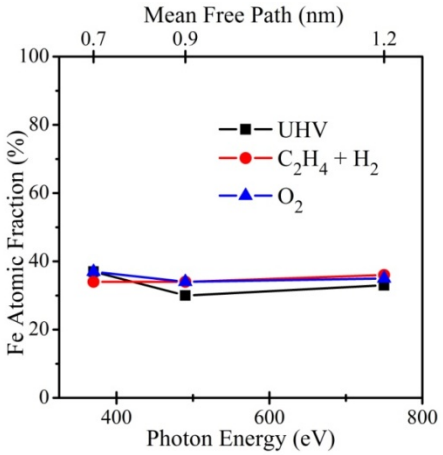

Figure 8-5. Atomic fractions of Fe in 2 nm PtFe nanoparticles with respect to probing depths under different gas environments at 298 K. The concentration of Fe is 34~37% at all IMFPs under all conditions, indicating that the 2 nm PtFe nanoparticles are uniformly distributed. Surface segregation cannot happen at 298 K because of low atomic mobility.

8.3.2 Pt_9Co-Co Core-Shell Nanoparticles

Figure 8-6 shows the model and the TEM image of as-synthesized Pt_9Co-Co core-shell nanoparticles. The particles have a ~8 nm large Pt_9Co nanocube core and a 1~3 nm thick pure Co shell. The Pt_9Co core and Co shell can be differentiated in the TEM image based on the contrast, since the particles all have dark cores and light shells. Pt_9Co-Co core-shell nanoparticles are ~10 nm large on average.

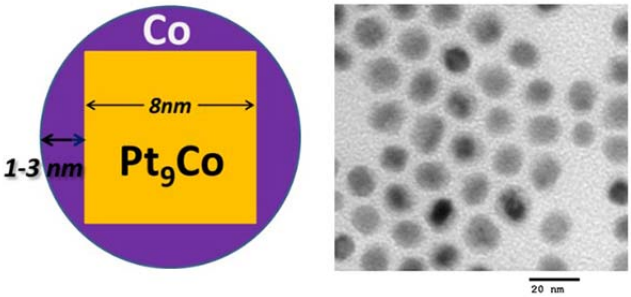

Figure 8-6. (left) Schematic and (right) TEM image of Pt_9Co-Co core-shell nanoparticles. The Pt_9Co core and Co shell can be distinguished through the difference in contrast.

The core-shell structure of Pt_9Co-Co nanoparticles can be verified by depth profiles studied using XPS at the synchrotron radiation source. As shown in Figure 8-7a, the concentration of Co is ~99% at ~0.7 and ~0.9 nm IMFPs, and slightly decreases to ~97% at ~1.2 nm IMFP. The fact that the atomic fraction of Co is close to 100% indicates that the

particle surface is nearly all occupied by Co atoms. Pt atoms, however, mostly consist of the inner core. Co is also more oxidized at surface than in the bulk, similar to Fe in PtFe nanopartciles studied in the previous section. Figure 8-7b shows that, at ~0.7 nm IMFP, Co is consisted of ~23% of metallic Co, ~32% of Co^{2+}, and ~45% of Co^{3+}. Although these values do not change much with the increase of IMFP to ~0.9 nm, the percentage of metallic Co has reached ~44% at ~1.2 nm IMFP. Meanwhile, the percentage of Co^{2+} greatly decreases to ~14% and that of Co^{3+} weakly drops to ~42%.

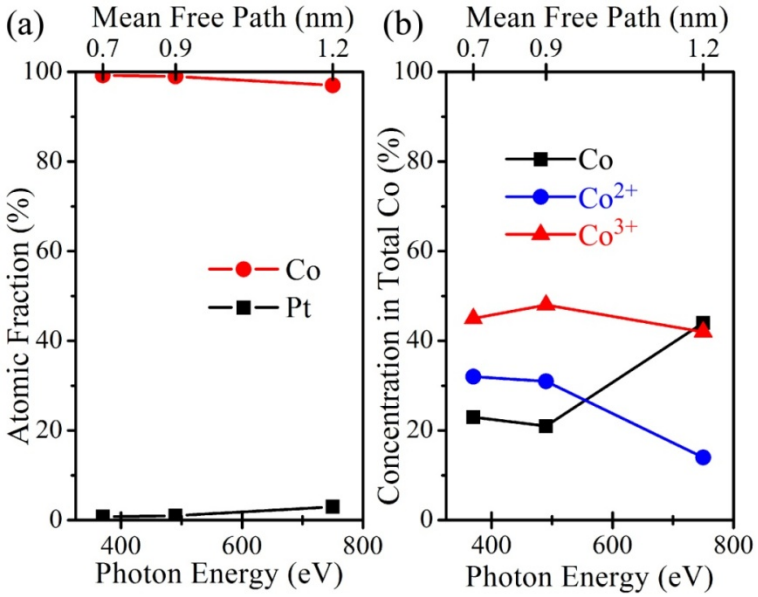

Figure 8-7. (a) Depth profiles and (b) distribution of Co oxidation states in the Co shell of Pt_9Co-Co core-shell nanoparticles. The Pt atomic fraction of only ~3% at ~1.2 nm IMFP suggests that Pt is almost undetectable at the surface. Co is more reduced in the bulk at the expense of Co^{2+}, whereas the percentage of Co^{3+} in total Co remains the same.

Previous studies in our group have revealed that Pt can facilitate H_2 to reduce Co in PtCo alloy nanoparticles at 398 K, at a much lower temperature than that required to reduce pure Co nanoparticles.[42] The performance of Pt_9Co-Co core-shell nanoparticles under H_2 was thus studied to compare with PtCo alloy nanoparticles. As displayed in Figure 8-8a, the introduction of H_2 at 298 K results in partial reduction of Co^{2+} to Co, as the percentage of metallic Co in total Co increases by ~12%, comparing to the result in Figure 8-7a. However, further heating the sample under H_2 even to 673 K does not give rise to further reduction of Co^{2+} and Co^{3+}, since the Co shell is always consisted of 32~36% of metallic Co, 18~22% of Co^{2+}, and 43~47% of Co^{3+}. The Co shell hence behaves like pure Co under H_2, leading to the stability of Pt_9Co-Co core-shell nanoparticles. Surface segregation phenomenon is not observed during the process either. Figure 8-8b illustrates that the concentration of Pt at ~0.7 nm IMFP remains at ~1% even while heating the Pt_9Co-Co core-shell nanoparticles to

673 K under 100 mTorr of H_2 for 2 h. Transport of Pt atoms into the Co lattice is inhibited probably by the mismatch between core and shell crystal structures, since Pt_9Co is in the fcc crystal lattice whereas Co is in the hexagonal close-packing (hcp) crystal lattice.

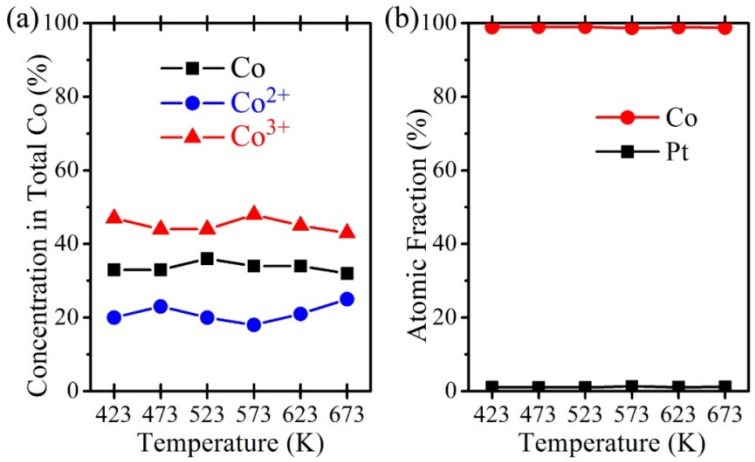

Figure 8-8. Changes in (a) Co oxidation states and (b) surface composition of Pt_9Co-Co core-shell nanoparticles at 100 mTorr of H_2 as a function of temperature at ~0.7 nm IMFP. The introduction of H_2 leads to slight reduction of Co, but heating does not result in further reduction. The concentration of Pt remains at ~1% even at 673 K, indicating that surface segregation does not occur.

8.3.3 $PtNi_3$ Polyhedra and Pt_3Ni Frameworks

Figure 8-9 shows the schematics and corresponding TEM images of solid $PtNi_3$ polyhedra and hollow Pt_3Ni frameworks. The Pt:Ni molar ratios of 1:3 in the initial polyhedra and 3:1 in the final frameworks were measured through energy dispersive X-ray (EDX) spectra. The initial $PtNi_3$ polyhedra with an average size of 15 nm exclusively expose {110} facets with a uniform morphology of rhombic dodecahedron. While heating in air at 393 K, such solid polyhedra dramatically evolve into hollow frameworks consisting of 24 edges that are 2 nm thick each. The framework products have kept the dodecahedron structure of the parent $PtNi_3$ particles.

XPS experiments were performed to explore the driving force of the morphological and compositional changes of the Pt−Ni bimetallic nanostructures. Figure 8-10 shows the Ni 2p and Pt 4f spectra of as-synthesized $PtNi_3$ polyhedra and Pt_3Ni frameworks acquired in vacuum with Al Kα source ($h\nu$ = 1486.6 eV). The Ni $2p_{3/2}$ region can be deconvoluted into four components locating at 852.5, 855.7, 860.4, and 864.2 eV. The peaks at 852.5 and 855.7 eV correspond to metallic Ni and Ni^{2+}, respectively,[43-47] and the other two peaks are the shake-up satellite features that are common for transition metals.[45-47] As shown by the fitted results, the majority of Ni is in the Ni^{2+} oxidized state at the $PtNi_3$ surface whereas in the metallic state at the Pt_3Ni surface. In contrast, the oxidation state of Pt does not vary

with the structural evolution, with most of the Pt atoms staying in the metallic state. This significant change in the relative intensity ratio of Ni^{2+} to Ni peak, along with the initial high concentration of Ni^{2+} at the $PtNi_3$ polyhedra surface, implies that Ni oxidation plays a critical role in the Pt−Ni structural changes. Ni atoms at the surface are more susceptible than Pt atoms to being oxidized by dissolved O_2 from air, yielding Ni^{2+} ions that can form soluble metal complexes with the oleylamine ligands. Since Ni dissolves faster than Pt, the particles gradually turns from Ni-rich to Pt-rich, until Pt_3Ni, the stable phase of the Pt−Ni alloy,[48] is formed.

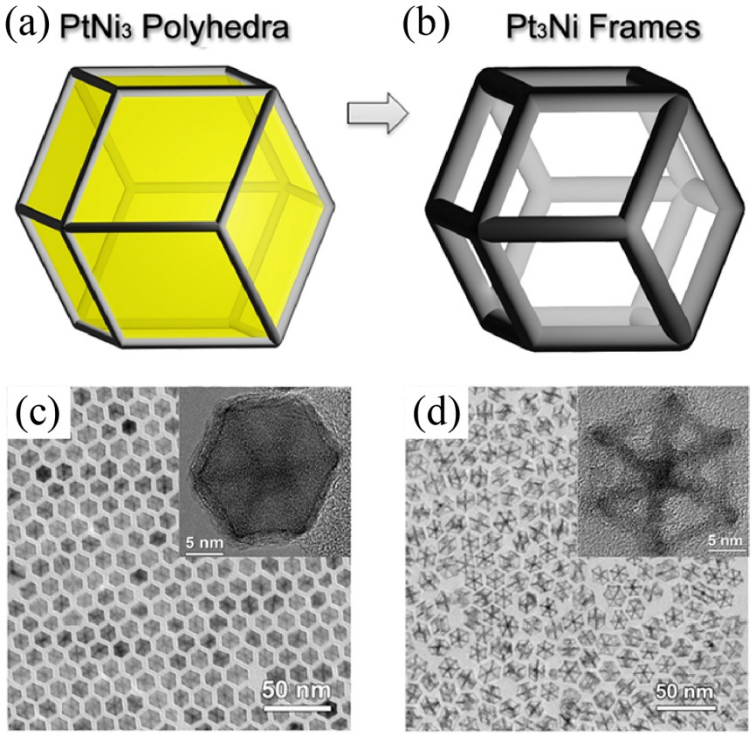

Figure 8-9. (a,b) Schematics and (c,d) TEM images of as-synthesized $PtNi_3$ polyhedra and Pt_3Ni frameworks. The insets display TEM images of single particles, showing that the particles are ~15 nm large on average and the edges are ~2 nm thick. $PtNi_3$ polyhedra show the morphology of dodecahedron that exclusively exposes {110} facets. Pt_3Ni frameworks maintain the structure of parent particles but have hollow interior.

The atomic fractions of as-synthesized $PtNi_3$ polyhedra and Pt_3Ni frameworks as a function of probing depths were studied with synchrotron-based XPS in UHV. As shown in Figure 8-11, the surface elemental composition varies with probing depths for both samples. Ni is slightly enriched at the $PtNi_3$ surface, since the Ni concentration in $PtNi_3$ polyhera is ~76%, ~73% and ~68% at IMFPs of ~0.7, ~0.9 and ~1.2 nm, respectively. Similarly, the Ni concentration is also higher at the Pt_3Ni surface than in the bulk, with Ni percentage of ~40%, ~29% and ~24% at ~0.7, ~0.9 and ~1.2 nm, respectively. The stronger

chemical bond of Ni with amine group in the oleylamine capping agent than Pt was responsible for the Ni enrichment at surface of as-synthesized nanostructures.

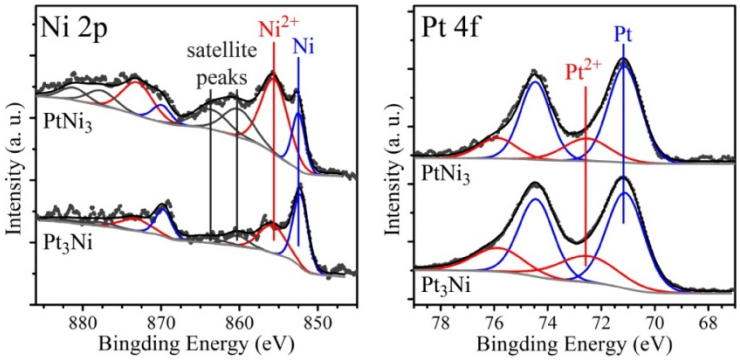

Figure 8-10. (left) Ni 2p and (right) Pt 4f spectra of as-synthesized (top) $PtNi_3$ polyhedra and (bottom) Pt_3Ni frameworks in UHV recorded by Al Kα X-ray. With the morphology variation from $PtNi_3$ polyhedra to Pt_3Ni frameworks, the intensity ratio of Ni^{2+} to Ni peaks has significantly decreased, whereas the oxidation state of Pt has bared changed. The Ni satellite peaks become less intense simultaneously with the weaker Ni^{2+} peak.

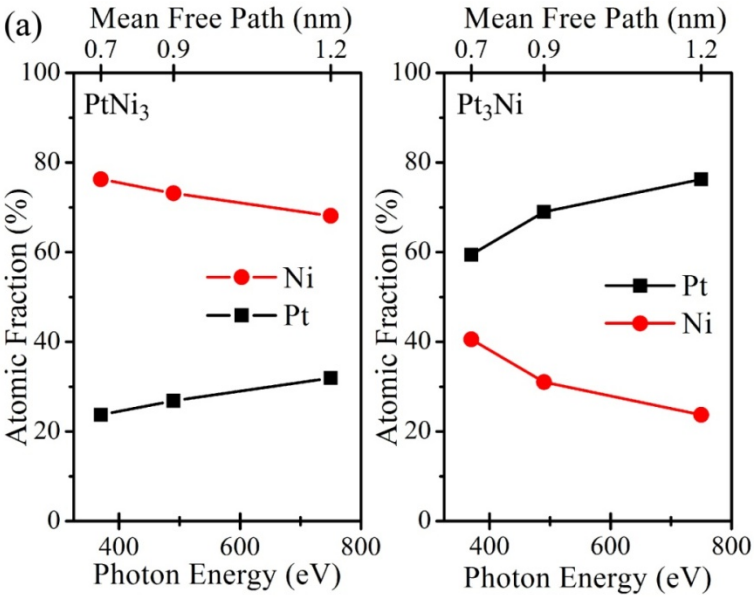

Figure 8-11. Depth profiles of the as-synthesized (a) $PtNi_3$ polyhedra and (b) Pt_3Ni frameworks in UHV at 298 K. The atomic fraction of Ni decreases with IMFPs in both samples.

Variations of Pt and Ni surface concentrations in response to changes in gas conditions were investigated by AP-XPS on both Pt−Ni nanostructures. The composition under each

condition is estimated by deconvoluting the Pt 4f and Ni 3p spectra acquired at 490 eV incident energy. An example of peak deconvolution is displayed in Figure 8-12, in which the Shirley-type background is subtracted prior to peak fitting. The main peak of Pt $4f_{7/2}$ is located at 71.1 eV, characteristic of metallic Pt.[33] Another Pt $4f_{7/2}$ component is found at 72.6 eV, corresponding to Pt^{2+} as discussed previously. The Ni $3p_{3/2}$ peak is centered at 68.5 eV, indicating that the majority of surface Ni is in oxidized states, probably as a mixture of Ni^{3+} and Ni^{2+}.[44] The metallic Ni $3p_{3/2}$ feature is found to locate at 66.2 eV through peak deconvolution, in agreement with literature.[43,49] Since the shake-up feature of Ni $3p_{3/2}$ strongly obscures with the Pt $4f_{7/2}$ component, the satellite peak of Ni 3p is not included in the peak fitting.

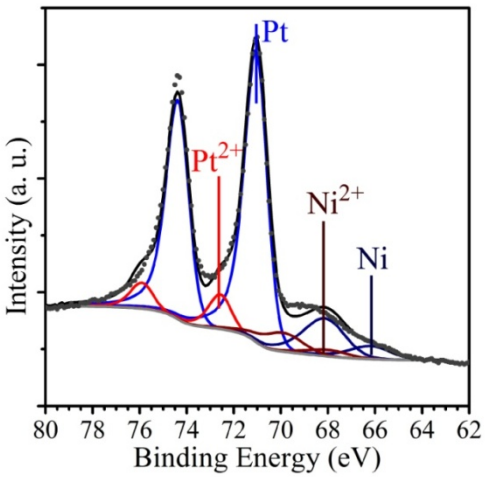

Figure 8-12. Pt 4f and Ni 3p spectra of $PtNi_3$ polyhedra recorded in UHV at 370 eV incident energy as the example of peak deconvolution. Shirley-type background was subtracted prior to peak fitting. Metallic and oxidized Pt and Ni components are both marked in the figure. Ni satellite peaks were not included in the deconvolution because Ni peaks are much less intense than Pt peaks.

Figure 8-13 illustrates the variation in surface composition with gases at 100 mTorr. As the repeated cycle of washing by DMF, ethanol and cyclohexane had sufficiently removed a large amount of oleylamine around nanoparticles, the residual surfactant was not burnt at elevated temperature and a low pressure of O_2 as in previous studies,[21-23] in order to maintain the particular shapes of samples. At 353 K, the surface composition of both $PtNi_3$ polyhedra and Pt_3Ni frameworks almost remains unchanged with respect to gas conditions, since metal atoms cannot overcome the diffusion barrier at low temperature, in accordance with previous studies.[22] When the temperature is enhanced to 393 K, the Ni concentration of $PtNi_3$ polyhedra at ~0.9 nm IMFP increases from ~73% under 100 mTorr of H_2 to ~82% under 100 mTorr of O_2, as shown in Figure 8-13a. Ni is preferentially oxidized by O_2 to

form nickel oxide that encapsulated the surface, thus tending to move to surface under oxidizing conditions.[50] The atomic fraction of Ni decreases back to ~74% when the gas environment is switched back to H_2 again. Pt tends to segregate towards surface under H_2 because of its strong tendency to segregate towards surface while coexisting with Ni.[51-53] Similar reversible trend of surface composition is also observed on Pt_3Ni frameworks at 393 K, as in Figure 8-13b. The Ni concentration at ~0.9 nm IMFP is ~32% initially under H_2, and increases to ~38% under O_2. After evacuating O_2 and re-introducing H_2, the Ni concentration declines to ~34%. Variation of surface Ni concentration is less prominent in Pt_3Ni frameworks than $PtNi_3$ polyhedra, probably as a result of the smaller amount of Ni in the hollow interior. AP-XPS results have thus supported the proposed mechanism that Ni diffuses out from $PtNi_3$ polyhedra through oxidation by O_2, which eventually leads to the Pt_3Ni hollow structure.

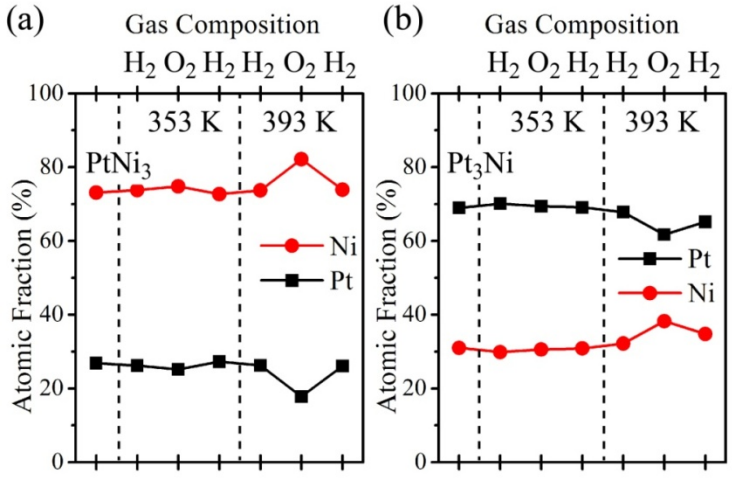

Figure 8-13. Changes of surface composition at ~0.9 nm IMFP of (a) $PtNi_3$ polyhedra and (b) Pt_3Ni frameworks in response to changes in gas environments at 353 K and 393 K. The pressure of H_2 and O_2 was kept at 100 mTorr during experiments. The starting points of both samples were measured in UHV at 298 K. At 353 K, the surface composition does not change with gas conditions. At 393 K when the atom migration mobility is higher, Ni segregates to surface under O_2 whereas Pt migrates to surface under H_2.

8.4 Conclusions

In summary, both Pt−Fe and Pt−Ni bimetallic systems undergo structural changes when varying gas conditions. The ethylene hydrogenation reaction mixture can reduce ~22% of Fe atoms at 2 nm PtFe nanoparticle surface at 298 K, and these Fe atoms are oxidized back in the presence of O_2. However, the oxidation state of Pt does not vary with gas conditions. Segregation of Pt or Fe atoms to surface is not observed either, owing to the low atomic mobility at 298 K. In the Pt−Ni system, Ni segregates to surface under O_2 because Ni is

easier to oxidize and migrates to bulk under H_2 since the surface energy of metallic Ni atoms is higher than Pt. Such surface segregation occurs at 393 K at which the structural evolution from solid $PtNi_3$ polyhedra to Pt_3Ni frameworks happens. Pt and Ni atoms do not segregate at lower temperatures such as 353 K. Lastly, Pt_9Co-Co core-shell nanoparticles do not undergo significant surface reconstruction under H_2, with only ~10% of the Co atoms being reduced after H_2 is added. However, even if heating to 673 K, surface Co atoms are not further reduced and the concentration of Pt at surface remains at ~1%.

8.5 References

(1) Somorjai, G. A.; Li, Y. *Introduction to Surface Chemistry and Catalysis*; 2nd ed.; Johns Wiley & Sons, Inc.: Hoboken, NJ, 2010.

(2) Besenbacher, F.; Chorkendorff, I.; Clausen, B. S.; Hammer, B.; Molenbroek, A. M.; Nørskov, J. K.; Stensgaard, I. *Science* **1998**, *279*, 1913-1915.

(3) Stamenkovic, V. R.; Fowler, B.; Mun, B. S.; Wang, G.; Ross, P. N.; Lucas, C. A.; Marković, N. M. *Science* **2007**, *315*, 493-497.

(4) Lim, B.; Jiang, M.; Camargo, P. H. C.; Cho, E. C.; Tao, J.; Lu, X.; Zhu, Y.; Xia, Y. *Science* **2009**, *324*, 1302-1305.

(5) Fu, Q.; Li, W.-X.; Yao, Y.; Liu, H.; Su, H.-Y.; Ma, D.; Gu, X.-K.; Chen, L.; Wang, Z.; Zhang, H.; Wang, B.; Bao, X. *Science* **2010**, *328*, 1141-1144.

(6) Zhou, S.; Varughese, B.; Eichhorn, B.; Jackson, G.; McIlwrath, K. *Angew. Chem., Int. Ed.* **2005**, *44*, 4539-4543.

(7) Sun, S. *Adv. Mater.* **2006**, *18*, 393-403.

(8) Habas, S. E.; Lee, H.; Radmilovic, V.; Somorjai, G. A.; Yang, P. *Nat. Mater.* **2007**, *6*, 692-697.

(9) Knudsen, J.; Nilekar, A. U.; Vang, R. T.; Schnadt, J.; Kunkes, E. L.; Dumesic, J. A.; Mavrikakis, M.; Besenbacher, F. *J. Am. Chem. Soc.* **2007**, *129*, 6485-6490.

(10) Yu, W.; Porosoff, M. D.; Chen, J. G. *Chem. Rev.* **2012**, *112*, 5780-5817.

(11) Nørskov, J. K.; Bligaard, T.; Rossmeisl, J.; Christensen, C. H. *Nature Chem.* **2009**, *1*, 37-46.

(12) Nørskov, J. K.; Rossmeisl, J.; Logadottir, A.; Lindqvist, L.; Kitchin, J. R.; Bligaard, T.; Jónsson, H. *J. Phys. Chem. B* **2004**, *108*, 17886-17892.

(13) Stamenkovic, V. R.; Mun, B. S.; Arenz, M.; Mayrhofer, K. J. J.; Lucas, C. A.; Wang, G.; Ross, P. N.; Marković, N. M. *Nat. Mater.* **2007**, *6*, 241-247.

(14) Mu, R.; Fu, Q.; Xu, H.; Zhang, H.; Huang, Y.; Jiang, Z.; Zhang, S.; Tan, D.; Bao, X. *J. Am. Chem. Soc.* **2011**, *133*, 1978-1986.

(15) Araya, P.; Diaz, V. *J. Chem. Soc., Faraday Trans.* **1997**, *93*, 3887-3891.

(16) Zhang, J.; Yang, H.; Fang, J.; Zou, S. *Nano Lett.* **2010**, *10*, 638-644.

(17) Wu, J.; Gross, A.; Yang, H. *Nano Lett.* **2011**, *11*, 798-802.

(18) Renzas, J. R.; Huang, W.; Zhang, Y.; Grass, M. E.; Hoang, D. T.; Alayoglu, S.;

Butcher, D. R.; Tao, F.; Liu, Z.; Somorjai, G. A. *Phys. Chem. Chem. Phys.* **2011**, *13*, 2556-2562.

(19) Huber, G. W.; Shabaker, J. W.; Evans, S. T.; Dumesic, J. A. *Appl. Catal. B* **2006**, *62*, 226-235.

(20) Rodriguez, J. A.; Goodman, D. W. *Science* **1992**, *257*, 897-903.

(21) Tao, F.; Grass, M. E.; Zhang, Y.; Butcher, D. R.; Renzas, J. R.; Liu, Z.; Chung, J. Y.; Mun, B. S.; Salmeron, M.; Somorjai, G. A. *Science* **2008**, *322*, 932-934.

(22) Tao, F.; Grass, M. E.; Zhang, Y.; Butcher, D. R.; Aksoy, F.; Aloni, S.; Altoe, V.; Alayoglu, S.; Renzas, J. R.; Tsung, C. K.; Zhu, Z.; Liu, Z.; Salmeron, M.; Somorjai, G. A. *J. Am. Chem. Soc.* **2010**, *132*, 8697-8703.

(23) Grass, M. E.; Park, M.; Aksoy, F.; Zhang, Y.; Kunz, M.; Liu, Z.; Mun, B. S. *Langmuir* **2010**, *26*, 16362-16367.

(24) Gao, F.; Wang, Y.; Goodman, D. W. *J. Phys. Chem. C* **2009**, *113*, 14993-15000.

(25) Andersson, K. J.; Calle-Vallejo, F.; Rossmeisl, J.; Chorkendorff, I. *J. Am. Chem. Soc.* **2009**, *131*, 2404-2407.

(26) Baraldi, A.; Giacomello, D.; Rumiz, L.; Moretuzzo, M.; Lizzit, S.; Buatier de Mongeot, F.; Paolucci, G.; Comelli, G.; Rosei, R.; Nieuwenhuys, B. E.; Valbusa, U.; Kiskinova, M. P. *J. Am. Chem. Soc.* **2005**, *127*, 5671-5674.

(27) Salmeron, M.; Schlögl, R. *Surf. Sci. Rep.* **2008**, *63*, 169-199.

(28) Starr, D. E.; Liu, Z.; Havecker, M.; Knop-Gericke, A.; Bluhm, H. *Chem. Soc. Rev.* **2013**, *42*, 5833-5857.

(29) Grass, M. E.; Karlsson, P. G.; Aksoy, F.; Lundqvist, M.; Wannberg, B.; Mun, B. S.; Hussain, Z.; Liu, Z. *Rev. Sci. Instrum.* **2010**, *81*, 053106.

(30) Powell, C. J.; Jablonski, A. *NIST Electron Inelastic Mean Free Path Database, version 1.2*; National Institute of Standards and Technology: Gaithersburg, MD, 2010.

(31) Shirley, D. A. *Phys. Rev. B* **1972**, *5*, 4709-4714.

(32) Yu, C. H.; Caiulo, N.; Lo, C. C. H.; Tam, K.; Tsang, S. C. *Adv. Mater.* **2006**, *18*, 2312-2314.

(33) Moulder, J. F.; Stickle, W. F.; Sobol, P. E.; Bomben, K. D. *Handbook of X-ray Photoelectron Spectronscopy*; Perkin-Elmer Corporation: Eden Prarie, MN, 1992.

(34) Hecq, M.; Hecq, A.; Delrue, J. P.; Robert, T. *J. Less Common Met.* **1979**, *64*, P25-P37.

(35) Huang, W.; Kuhn, J. N.; Tsung, C.-K.; Zhang, Y.; Habas, S. E.; Yang, P.; Somorjai, G. A. *Nano Lett.* **2008**, *8*, 2027-2034.

(36) Yamashita, T.; Hayes, P. *Appl. Surf. Sci.* **2008**, *254*, 2441-2449.

(37) Murugesan, M.; Bea, J. C.; Yin, C. K.; Nohira, H.; Ikenaga, E.; Hattori, T.; Nishijima, M.; Fukushima, T.; Tanaka, T.; Miyao, M.; Koyanagi, M. *J. Appl. Phys.* **2008**, *104*, 074316-074315.

(38) Wang, J.; Mao, B.; White, M. G.; Burda, C.; Gole, J. L. *RSC Adv.* **2012**, *2*,

10209-10216.

(39) Dutta, G.; Waghmare, U. V.; Baidya, T.; Hegde, M. S. *Chem. Mater.* **2007**, *19*, 6430-6436.

(40) Xu, H.; Fu, Q.; Yao, Y.; Bao, X. *Energy Environ. Sci.* **2012**, *5*, 6313-6320.

(41) Yu, W.; Wu, B.; Xu, J.; Tao, Z.; Xiang, H.; Li, Y. *Catal. Lett.* **2008**, *125*, 116-122.

(42) Zheng, F.; Alayoglu, S.; Guo, J.; Pushkarev, V.; Li, Y.; Glans, P. A.; Chen, J. L.; Somorjai, G. A. *Nano Lett.* **2011**, *11*, 847-853.

(43) Hüfner, S.; Wertheim, G. K. *Phys. Lett. A* **1975**, *51*, 301-303.

(44) McIntyre, N. S.; Cook, M. G. *Anal. Chem.* **1975**, *47*, 2208-2213.

(45) Biesinger, M. C.; Payne, B. P.; Lau, L. W. M.; Gerson, A.; Smart, R. S. C. *Surf. Interface Anal.* **2009**, *41*, 324-332.

(46) Marco, J. F.; Gancedo, J. R.; Ortiz, J.; Gautier, J. L. *Appl. Surf. Sci.* **2004**, *227*, 175-186.

(47) Kim, K. S.; Davis, R. E. *J. Electron Spectrosc. Relat. Phenom.* **1972**, *1*, 251-258.

(48) Dahmani, C. E.; Cadeville, M. C.; Sanchez, J. M.; Morán-López , J. L. *Phys. Rev. Lett.* **1985**, *55*, 1208-1211.

(49) Björneholm , O.; Andersen, J. N.; Wigren, C.; Nilsson, A.; Nyholm, R.; Martensson, N. *Phys. Rev. B* **1990**, *41*, 10408-10412.

(50) Samsonov, G. V. *The Oxide Handbook*; 2nd ed.; IFI/Plenum New York, 1982.

(51) Skriver, H. L.; Rosengaard, N. M. *Phys. Rev. B* **1992**, *46*, 7157-7168.

(52) Ruban, A. V.; Skriver, H. L.; Nørskov, J. K. *Phys. Rev. B* **1999**, *59*, 15990-16000.

(53) Stamenkovic, V. R.; Mun, B. S.; Mayrhofer, K. J. J.; Ross, P. N.; Marković, N. M. *J. Am. Chem. Soc.* **2006**, *128*, 8813-8819.

Chapter 9

Summary and Outlook

This thesis has concentrated on *in situ* structural changes on Pt and Cu crystal surfaces and Pt-based bimetallic nanoparticle catalysts, in order to seek the influence of catalyst surface structure on heterogeneous catalysis. HP-STM studies has demonstrated the high activity of low-coordinated step sites on both Pt and Cu surfaces compared with terrace sites, which also results in dramatic surface reconstruction. The type of low-coordinated sites, i.e. the orientation of steps, plays a critical role in inducing surface reconstruction. Distinguished structure observed at high gas pressures from structure seen in vacuum illustrates the necessity of *in situ* studies. Changes in surface composition monitored with AP-XPS have provided valuable chemical and dynamical information for understanding the structural changes and reaction mechanisms.

The *in situ* structural investigation started with the O_2/Pt(557) system along with its reference O_2/Pt(111) system. Chemisorbing on Pt steps as well as terraces at 10^{-7} Torr, O_2 induces the growth of Pt oxide from 1D chains to 2D clusters at pressures of 1 Torr at 298 K. Most clusters are populated within 2 nm from steps that present on Pt(111) because of miscut. Thereby clusters cover the entire Pt(557) surface since the terrace width is 1.4 nm. Oxygen chemisorption pattern is observed on Pt(111) terraces even at 1 Torr. Results on these two systems perfectly demonstrate the importance of *in situ* structural studies on low-coordinated surface sites. Depth profiles of the oxidized Pt(557) surface, studied using AP-XPS at synchrotron with tunable X-ray sources, have revealed that Pt oxide formed on Pt(557) is less than 0.6 nm thick, indicating that the growth of bulk oxide is kinetically inhibited at 298 K.

More interestingly, Pt oxide clusters formed under 1 Torr of O_2 disappear on Pt(557) and Pt(111) when O_2 is evacuated to 10^{-8} Torr. Since neither oxide decomposition nor oxygen desorption happens at 298 K, reactions of Pt oxide with H_2 and CO in the background are responsible for the removal of Pt oxide. In continuation, the Pt(557) surface structure was explored under H_2-O_2 and CO-O_2 mixtures to verify that the high reactivity of Pt oxide towards reducing gases. At a partial pressure of only 43 mTorr while keeping the O_2 partial pressure at 950 mTorr, H_2 completely removes the Pt oxide clusters which were initially formed under 950 mTorr of O_2. AP-XPS has demonstrated that the coverage of Pt oxide decreases with the increase of H_2 partial pressures, whereas the total coverage of H_2O and OH retains at a constant value. In addition, the fact that the consumption of Pt oxide is exclusively responsible for the decrease in Pt oxide coverage indicates that Pt oxide is an important reaction intermediate during hydrogen oxidation reaction. Under 1:1 CO-O_2

mixture, CO-induced step doubling and triangular cluster formation are observed.

Not only does the existence of low-coordinated sites affect adsorbate-induced surface reconstruction, but the sort of low-coordinated sites also influence on structural evolution. Two stepped Pt crystals, Pt(557) and Pt(332), which have the same terraces but differ only in the step orientation, were investigated under the CO-C_2H_4 mixture. After CO creates Pt clusters at step edges, subsequent addition of C_2H_4 with the same partial pressure restores the stepped structure on Pt(332). In contrast, Pt clusters on Pt(557) are preserved after adding C_2H_4. When the gas introduction sequence is reversed, C_2H_4 causes periodic adsorption patters to appear on Pt(332) but not on Pt(557), which further confirms the critical role of step orientation in the restructuring process. The three-fold sites at (111) steps allow Pt(332) to accommodate more ethylidyne converted from C_2H_4 adsorption than Pt(557), because ethylidyne occupies three-fold hollow sites. Adding CO after C_2H_4 does not create Pt clusters on either surface.

Studies on structure and mobility then moved on to the Pt(100) surface that initially undergoes a hexagonal reconstruction, under C_2H_4 and its mixture with H_2 and CO in the Torr range. The reconstruction on Pt(100) is preserved under 1 Torr of C_2H_4 by a mobile layer of ethylidyne and di-σ-bonded ethylene adsorbates. Pt atoms in the hexagonal layer are also mobile because adsorption weakens the interaction between the surface and bulk layers. However, at 5×10^{-6} Torr of C_2H_4, the reconstruction is lifted by co-adsorbed CO from background gases, creating 2~3 nm large Pt islands across the Pt(100) surface. Under 1 Torr of 1:1 C_2H_4-H_2 mixture, the active Pt(100) surface exhibits high mobility under STM, along with roughly preserved hexagonal reconstruction. The surface mobility is quenched and the Pt(100) catalyst is deactivated as soon as 3 mTorr of CO is added into the reaction mixture. AP-XPS results implicate CO adsorption on Pt(100) in stopping the surface mobility and catalytic reaction, which also lifts the reconstruction in the meantime. A highly mobile catalyst surface is crucial for catalytic turnovers.

Structural changes on the stepped Cu(557) surface were explored under similar gases or gas mixtures to studies on Pt(557), for a broader perspective on adsorbate-induced restructuring processes. Although the Cu(557) surface also undergoes structural evolution at high gas pressures, reconstruction on Cu(557) are distinguished from the observation on Pt(557) under the same gas environment owing to their different affinities to gas molecules. The higher mobility of Cu atoms than Pt atoms contributes to the distinct reconstruction as well. 12 Torr of CO is required to create Cu clusters on Cu(557), whereas 1 Torr of CO causes only wide terraces. H_2 is also able to induce formation of large Cu terraces, which grow wider with the subsequent addition of CO. C_2H_4 results in Cu clusters and a highly mobile surface under STM owing to the weak adsorption of C_2H_4 on Cu. Adding CO into C_2H_4 does not alter the structure. 1 Torr of O_2 significantly oxidizes Cu(557), forming thick Cu oxide hardly resolvable with STM, especially in the presence of O_2.

Lastly, since nanoparticles are mostly used in industrial heterogeneous catalysis, and

because bimetallic systems usually exhibit high activity and selectivity, three kinds of Pt-based bimetallic nanoparticle catalysts were monitored with AP-XPS under relevant reaction conditions. Fe atoms are partially reduced at the 2 nm PtFe nanoparticle surface under the ethylene hydrogenation mixture and partially oxidized by O_2. The Pt_9Co-Co core-shell nanoparticles do not undergo any changes in surface composition or chemical states under H_2 even at 673 K. The surface composition of $PtNi_3$ polyhedra and Pt_3Ni frameworks varies reversibly between O_2 and H_2 at 393 K. O_2 oxidizes Ni and drives Ni to segregate to the surface, whereas the oxidation state of Pt does not change. In contrast, H_2 reduces Ni and drives Pt towards the surface, because the surface energy of metallic Pt is lower than Ni. At lower temperatures, for example 353 K, such surface segregation does not occur owing to the low atomic mobility.

Experiments following this thesis can be conducted in several directions. Bimetallic catalysts deserve extraordinary attention in HP-STM studies, owing to their outstanding catalytic performances and because of the existence of few examples in literature. The preferred bonding of each metal to one reactant in the reaction mixture, if resolved, can shed light on the synergistic effect. Bimetallic catalysts also open the possibilities for enormous intriguing dynamic phenomena under reaction conditions, since atomic mobility of two metals are facilitated differently by gas adsorption. Model catalysts can be prepared by either depositing one metal on the other metal substrate or by alloying two metals.

In addition, it is noteworthy that all the gas reactants used in this thesis are small molecules. Larger molecules, which can even be in the liquid phase at 298 K but have high vapor pressure, for instance benzene, cyclohexene, and so forth, are promising reactant adsorbates in future studies. HP-STM studies using liquid with high vapor pressure is able to bridge the gap between heterogeneous reactions at the solid−liquid interface and at the solid−gas interface.

Halogen lamp heater in the current instrument cannot precisely control the sample temperature. Once one of the glass beads used to separate the STM body and the sample stage drops as a result of shaking during sample transfer, thermal isolation is severely damaged and thermal drift is enhanced accordingly during high-temperature experiments. The sample stage can be modified by using a ceramic heater for better temperature control and by replacing the glass beads with a ceramic thermal isolation layer between the sample and the STM body. Such improvement allows for high-temperature HP-STM studies that provide molecular information under conditions closer to real catalysis.

DISCLAIMER